UNIVERSITÀ
DEGLI STUDI
DI PADOVA

UNIVERSITÀ DEGLI STUDI DI PADOVA

DIPARTIMENTO DI INGEGNERIA INDUSTRIALE

SCUOLA DI DOTTORATO DI RICERCA IN INGEGNERIA INDUSTRIALE
INDIRIZZO IN INGEGNERIA DELL'ENERGIA
CICLO XXIX

Analysis, Design and Test of High Efficiency Electrical Machines with a Rotor Winding

Direttore della Scuola:
CH.MO PROF. PAOLO COLOMBO

Coordinatore d'Indirizzo:
CH.MO PROF. LUISA ROSSETTO

Supervisore:
CH.MO PROF. NICOLA BIANCHI

Dottorando: ING. DAMIANO MINGARDI

24 January 2017

Contents

Preface

This thesis is submitted to the University of Padova, Department of Industrial Engineering, Italy, as partial fulfillment of the requirements for the degree of Doctor of Philosophy (Ph.D.) in Energy engineering. The research carried out during the 3-year period of this Ph.D school is summarized in this thesis.

Abstract

This thesis deals with the analysis, design and test of three-phase high efficiency electrical motors, with particular reference to motors with a rotor winding. At first, the background and the motivations of this work are described. The bibliography on the subjects is deeply examined and a selection of the most relevant papers can be found in the reference. In this scenario, the main objective of this thesis are illustrated.

The Line-Start (LS) Synchronous Machine (SyM) design is a subject under investigation since the beginning of the last century, when solid state power converters was not available to drive SyMs. The LS SyM diffusion was limited by the intrinsic difficulties in its design and by the availability of the cheaper and more robust Induction Machine (IM). The working principle of IM and LS SyM are briefly described, as well as the state of the art of the techniques of analysis. Recently, there is a renewed interest on LS SyMs due to the new efficiency requirements and fast analysis techniques are required for the LS SyM design.

A Finite-Element (FE) aided analytical model is developed to simulate the LS SyM dynamic. The aim is to develop a model that gives reliable solutions with limited computational efforts compared with other analysis techniques. With this procedure, the LS SyM rotor parameters can be quickly calibrated to fulfill the dynamic load requirements.

An innovative analysis technique of LS SyM steady state condition is described. Such an analysis is carried out in the same reference frame used for classical SyMs. It is shown that the analysis can be used to optimize some machine parameters.

The issues in LS SyM manufacturing are introduced, with particular reference to the die casting process. The possibility to apply the recent improvements in the SRM design to LS SyM is discussed from the manufacturing point of view. Stochastic optimization has been adopted for the design of electrical motors to reduce the torque

ripple, increase the average torque and reduce the losses. The LS SyM torque ripple reduction, achieving at the same time a high average torque, is an important issue even though this topic is not treated extensively in the literature for LS SyM. For this reason, a stochastic optimization is considered in this thesis for the design of a new LS SyM lamination. The analysis is applied on a small size, 2-pole, three-phase LS SyM as this category is still not found in the motor market. The optimization is carried out considering the necessity to achieve a robust design, suitable for the industrial production, as such a LS SyM must be competitive with the workhorse of electrical motors, the IM. One of the most promising design is prototyped. Its performance are compared with the corresponding IM.

To demonstrate the feasibility in adopting LS SyM in the large-scale production, an innovative LS SyM design is proposed. The main aim is to use the same lamination for motors of different number of poles so as to reduce the manufacturing cost. A tradeoff between contrasting aspects is necessary in the design step. The performance achievable by these rotor structures are quantified.

An analytical model that describes the mutual interaction between coupled electrical circuits in machines with complex rotor structure is developed. Such a model is useful to analyze the parasitic torques in the torque characteristic of motors with rotor cage such as IM and LS SyM. The literature reveals that this topic has been discussed extensively for IM. As regards LS SyM, there is a lack of theoretical studies regarding harmonic phenomena due to the complex machine structure. This part of the thesis aims to fill this gap.

The high and unstable cost of rare-earth PMs, together with the advances in solid-state control technology, leads designers to reconsider IM for variable speed drive (VSD) applications. To the aim of making the IM suitable for the full-speed sensorless control, a particular cage design is considered. An intentionally created saliency is introduced in the rotor so as to allow the rotor position to be estimated by means of a high frequency (HF) injected signal in the stator winding also at zero-speed. Different experimental tests are carried out on IMs with asymmetrical rotor cage to validate the analysis techniques and quantify the achievable performance.

As far as the HF signal injection sensorless technique is concerned, the cross-saturation differential inductance of SyMs represents an issue. It causes a rotor position estimation error, reducing the region in which such technique is effective. The properties of the cross-saturation inductance are deeply discussed. It is originally shown that the cross-saturation inductance depends from certain machine parameters. With such an analysis, a designer can consider the effect of the cross-saturation inductance in any model-based control algorithm.

A rotor winding is added in Surface-mounted permanent-magnet machine (SPM) to create a HF anisotropy that is useful to detect the rotor position by means of a HF signal injection. Such a configuration is called "ringed-pole". In literature, this technique has been used on small-size machines. In certain configuration, the presence of the additional rotor winding causes significant rotor losses. This part of the thesis studies the rotor losses in ringed pole machines by means of FE analysis and analytical models. The aim is to investigate if the ringed-pole technique can be adopted also for large machines from the point of view of additional losses.

With few exceptions, the work described in this thesis is always supported by means of experimental measurements. Dedicated experiments has been designed. Their results are compared with those achieved with analytical models or FE analysis.

Keywords

Line start, Efficiency, Power factor, Induction motor, Synchronous motor, Machine parameters, Inductance, Differential inductance, Cross saturation, Optimization, Reluctance motor, Reluctance assisted motor, Permanent Magnet, Starting performance, Steady state, Torque characteristic, Torque dip, Synchronous torque, Asynchronous torque, Losses, Rotor losses, Analytical model, Ringed pole, Sensorless, High frequency injection

Sommario

Questo lavoro di tesi è incentrato sull'analisi, la progettazione e la prototipazione di macchine elettriche trifase ad alto rendimento, con particolare riferimento a motori dotati di avvolgimenti rotorici. Inizialmente si descrivono le motivazioni di questo lavori di tesi e il contesto in cui essa si inserisce, illustrandone i principali obiettivi. Una dettagliata analisi bibliografica è alla base del lavoro svolto. Una selezione di questi lavori si trova nelle referenze.

I motori sincroni autoavvianti (LS SyM) sono stati introdotti nella prima metà del novecento e la loro progettazione è soggetto di ricerca sin da allora. Essi non si sono mai affermati a causa della loro difficile progettazione e per la disponibilità del più robusto ed economico motore ad induzione (IM). Dopo aver descritto il principio di funzionamento di IM e LS SyM, se ne illustrano le tecniche di analisi sviluppate fino al giorno d'oggi. Negli ultimi anni vi è un rinnovato interesse verso i LS SyM grazie agli stringenti requisiti di rendimento. Vi è quindi la necessità di tecniche di progettazione veloci ed affidabili per LS SyM.

I risultati di simulazioni agli elementi finiti sono stati combinati a modelli analitici per descrivere la complessa dinamica di LS SyM. L'obiettivo è quello di ottenere una risposta sufficientemente precisa in tempi molto più brevi rispetto ad altre tecniche di analisi. In questo modo si rende possibile una rapida e precisa calibrazione dei parametri rotorici necessari per soddisfare determinati requisiti di carico dinamico.

Parte di questa tesi è dedicata allo sviluppo di una tecnica di analisi per LS SyM in condizioni di regime. Tale analisi è condotta nello stesso sistema di riferimento usato nei classici modelli per macchine sincrone non autoavvianti. Si mostra che l'analisi proposta permette anche di ottimizzare alcuni parametri di macchina.

Negli ultimi anni vi sono stati numerosi sviluppi nella progettazione di macchine sincrone a riluttanza, con o senza l'assistenza di magneti permanenti. In questa tesi si è voluto investigare sulla possibilità di applicare tali sviluppi ai LS SyM, tenendo in considerazione i vincoli costruttivi legati alla presenza della gabbia rotorica. Lo scopo è quello di ridurre il volume di magneti permanenti utilizzati per contenere i costi di produzione. Si è affrontato il problema dell'industrializzazione dei LS SyM, con particolare riferimento al processo di pressofusione del rotore. Nell'intento di ridurre il ripple di coppia, incrementare la coppia media e ridurre le perdite dei motori elettrici, recenti lavori propongono l'utilizzo di algoritmi di ottimizzazione stocastica nella fase di progettazione. I suddetti obiettivi sono basilari anche per LS SyM, anche se per questo tipo di motori la letteratura è meno fornita. Per questo motivo si è voluto utilizzare un algoritmo di ottimizzazione nella fase di progettazione della lamiera di un LS SyM. L'analisi è applicata ad un LS SyM trifase a 2 poli di piccola taglia, dato che ancora non si trovano nei cataloghi dei principali costruttori. L'ottimizzazione è sviluppata considerando la necessità di ottenere un progetto robusto e comunque adatto alla produzione industriale, dato che tale LS SyM deve essere competitivo con l'ormai consolidato IM. Una promettente struttura rotorica è stata prototipata. Le prestazioni ottenute sono confrontate con quelle del corrispondente IM.

Si è proposta un innovativa configurazione di LS SyM per dimostrare la fattibilità del loro utilizzo su scala industriale. Lo scopo è quello di utilizzare la stessa lamiera per motori con un diverso numero di poli, riducendo di conseguenza il costo di produzione.

Per fare ciò è necessario un compromesso tra aspetti contrastanti nel progetto. In questa parte di tesi, si è voluto quantificare le prestazioni ottenibili da tali geometrie nelle diverse configurazioni.

In questa tesi si è sviluppato un modello analitico per caratterizzare l'interazione di circuiti elettrici accoppiati in strutture complesse quali quelle dei LS SyM. Questa analisi mira ad essere uno strumento per la determinazione analitica delle coppie parassite in motori dotati di gabbia rotorica come LS SyM e IM. La letteratura riporta un gran numero di lavori riguardanti la descrizione di coppie parassite nella caratteristica di coppia di motori IM. In LS SyM, l'analisi delle coppie parassite è molto più complessa a causa della struttura di macchina. In letteratura, gli studi analitici riguardanti gli effetti di armoniche di MMF in motori LS SyM sono pochi ed incompleti.

L'elevato ed instabile prezzo dei magneti permanenti, assieme allo straordinario sviluppo dell'elettronica allo stato solido, ha spinto a riconsiderare il motore ad induzione per applicazioni a velocità variabile. In questo scenario, si è considerato un avvolgimento rotorico a gabbia di scoiattolo in cui i conduttori sono asimmetrici. Tale asimmetria permette il riconoscimento sensorless della posizione rotorica tramite iniezione di segnali ad alta frequenza negli avvolgimenti di statore anche a velocità molto basse. Sono stati condotti test sperimentali su prototipi di IM con gabbia asimmetrica allo scopo di verificare le tecniche di analisi e di quantificare le prestazioni ottenibili da tali geometrie.

Proseguendo l'analisi delle problematiche riscontrate in controlli di tipo sensorless con iniezione di segnale, si sono approfondite le proprietà della mutua induttanza differenziale causata dal fenomeno della saturazione incrociata tra asse d e q in macchine sincrone. Essa causa un errore nella stima della posizione rotorica, riducendo di fatto l'applicabilità del controllo sensorless con iniezione di segnale. Dopo aver discusso in dettaglio le proprietà di tale induttanza, si è dimostrato che essa dipende da alcuni parametri di macchina. Con i risultati ottenuti, può essere intrapresa una serie di accorgimenti nel controllo della macchina volta a mitigare l'effetto negativo dell'induttanza mutua dovuta alla saturazione incrociata.

Uno o più avvolgimenti rotorici possono essere introdotti anche in motori sincroni a magneti permanenti superficiali, allo scopo di estendere l'applicabilità del controllo sensorless con iniezione di segnale anche a questo tipo di motori. In questo tipo di macchine, denominate "ringed-pole", tali avvolgimenti rotorici possono essere sede di perdite importanti nel funzionamento a regime. In letteratura, questa tecnologia è stata applicata a motori di piccola taglia. In questo contesto, si sono studiate le perdite rotoriche di macchine "ringed-pole" tramite analisi agli elementi finiti e modelli analitici. Lo scopo è quello di verificare se l'uso di tale tecnologia può essere esteso a macchine di taglia superiore dal punto di vista delle perdite rotoriche.

Con poche eccezioni, gli argomenti di questa tesi sono validati tramite misure sperimentali. I risultati delle prove sperimentali sono confrontati con quelli provenienti da modelli analitici o da analisi agli elementi finiti.

Outline of the thesis

The first Chapter of this thesis is dedicated to illustrate the thesis background and the main goals of the thesis. The other Chapters of the thesis can be divided into 2 groups. Each Chapter contains an introduction to describe the literature review and the content of the Chapter itself. The first part of the thesis includes chapters from 2 to 7. It is dedicated to the analysis of self-starting machines, IM and LS SyM.

Chapter 2 provides an overview on electrical machines that can be fed directly-on-line, the IM and the LS SyM. As regards the IM, its main features and techniques of analysis such as equivalent circuit and different FE approaches are illustrated. As far as the LS SyM is concerned, the pull-in and pull-out torque concept, its equivalent circuits, the main design issues and its characteristic with respect the IM one are discussed;

Chapter 3 describes an analytical model of LS SyM combined with magnetostatic and time-harmonic FE analysis. The non-linear relationship between the main flux and the magnetizing current is computed with and without considering the cross saturation effect. The parameters of the machines are estimated as a function of magnetizing currents and rotor frequency and they are used to simulate the dynamic of the machine. To validate the model, different experimental tests on a LS SyM prototype have been carried out.

Chapter 4 presents an innovative technique of analysis of the steady state condition of LS SyM. The analysis is carried out in the $d-q$ reference frame. The main losses components are computed to estimate the efficiency. The simulated working point of LS SyM is represented in the i_d–i_q plane, as well al the limit of synchronization. The working points measured on a LS SyM prototype are compared with the predictions. It is shown how parameters such as the number of conductors per slot and the machine stack length affect the LS SyM working point.

Chapter 5 deals with the LS SyM design optimization, manufacturing and testing. From the manufacturing point of view, some constrains must be respected in LS SyM design, limiting the effectiveness of certain rotor geometries. A stochastic optimization has been used to design the rotor lamination of a LS SyM to replace a low efficiency IM. An automatic design procedure is developed. FE analysis is used to evaluate the optimization objectives considering the machine nonlinearities. Both steady state and dynamic performance are considered. Experimental measurements are carried out on a LS SyM resulting from the optimization and the results are compared with the predictions. From the experimental tests, an overview comparison between the IM and LS SyM performance is given.

Chapter 6 analyzes three possible LS SyM configurations suitable to be used for motors of different number of poles. The first machine configuration is suitable for 2-, 4- and 6-pole motors, respectively. The second and the third are suitable for 2- and 4-pole motors, respectively. The performance achievable with such rotor structures are quantified. Part of this Chapter is dedicated to illustrate the experimental tests carried out to validate the predictions.

Chapter 7: An analytical model that describes the mutual interaction between coupled electrical circuits in machines with complex rotor structure is developed. After defining the main assumptions of the analytical model, the procedure to compute the self- and mutual-inductances of each circuit present in the machine is derived. Such an analysis consider not only the fundamental component of the inductances, but all their harmonic spectra. The aim is to provide an analytical technique to determine the torque dips in the LS SyM and IM torque characteristic, being the IM a particular subset of LS SyM. FE analysis is used to validate the results. The proposed model is useful in general whether it is of interest to determine the inductances of a machine with saliency considering the harmonic content.

The second part of the thesis includes chapters from 8 to 10. It deals with design aspects of SyMs in which the HF signal injection sensorless technique is implemented in the VSD.

Chapter 8: FE analysis is carried out on IM in which an intentionally created saliency is introduced in the rotor to achieve an estimation of their HF response as a function of rotor position. Based on the results of the FE analysis, two IM prototypes with rotor saliency are manufactured. Practical aspects on their realization are discussed. A third standard IM prototype is used for comparison. The dynamic and steady state performance of the prototypes are experimentally quantified. The measured HF parameters are compared with the simulated ones.

Chapter 9 aims to describe the properties of the cross-saturation inductance l_{dq} for SyMs such as SRM, interior and surface-mounted PM machines. The analysis is supported by means of FE simulations and experimental measurements on prototypes. A simplified magnetic model is introduced to predict the position of the locus $l_{dq} = 0$, determining consequently the sign of l_{dq} in the i_d–i_q plane.

Chapter 10 investigates the ringed-pole machine from the point of view of the ring losses. Machines of different sizes and winding types are investigated. The FE analysis and the analytical model adopted to compute the ring losses is described, illustrating their peculiarities. The influence of the ring configuration and cross-sectional area on the ring losses is investigated.

List of publications

Several parts of this Ph.D. thesis have been published in international conferences and journals. Hereafter the publications are listed in a chronological order:

- **Mingardi D.**, Bianchi N., Fornasiero E., Alberti L., "Induction Motor with an Intentionally Created Saliency for Sensorless Application", 39-th IEEE annual conference of Industrial Electronics Society (IECON), 10-13 November 2013, Wien, Austria, DOI: 10.1109/IECON.2013.6699596;
- **Mingardi D.**, Fornasiero E., Bianchi N., Bolognani S., Faggion A., "Ringed Losses Evaluation in Ringed Pole PM Motors", IEEE international symposium

on Sensorless Control for Electrical Drives and Predictive Control of Electrical Drives and Power Electronics (SLED/PRECEDE), 17-19 October 2013, Munich, Germany, DOI: 10.1109/SLED-PRECEDE.2013.6684514;

- **Mingardi D.**, Bianchi N., Alberti L., Zeni R., "Analysis and Test of the Sensorless Capability of Induction Motor with Created Saliency", International Conference on Electrical Machines (ICEM), 2-5 September 2014, Berlin, Germany, DOI: 10.1109/ICELMACH.2014.6960207;
- **Mingardi D.**, Bianchi N., "FE-Aided Analytical Method to Predict the Capabilities of Line-Start Synchronous Motors", IEEE Energy Conversion Congress and Exposition (ECCE), 14-18 September 2014, Pittsburgh, PA, USA DOI: 10.1109/ECCE.2014.6954104;
- Scandola F., **Mingardi D.**, Bianchi N., "Design and Test of an Electric Minidumper", IEEE Workshop on Electrical Machines Design, Control and Diagnosis (WEMDCD), 26-27 March 2015, Torino, Italia, DOI: 10.1109/WEMDCD.2015.7194486;
- **Mingardi D.**, Fornasiero E., Bianchi N., Bolognani S., Faggion A., "Ringed Losses Evaluation in Ringed Pole PM Motors", IEEE Transaction on Industry Applications, vol. 51, no. 5, pp. 3686-3695, Sept 2015, DOI: 10.1109/TIA.2015.2424198;
- **Mingardi D.**, Bianchi N., Alberti L., Zeni R., "Analysis and Test of the Sensorless Capability of Induction Motors with Created Saliency", IEEE Transaction on Industry Applications, vol. 52, no. 3, pp. 2186-2193, may 2016, DOI: 10.1109/TIA.2016.2519414;
- **Mingardi D.**, Morandin M., Bolognani S., Bianchi N., "On the Proprieties of the Differential Cross-Saturation Inductance in Synchronous Machines", IEEE Energy Conversion Congress and Exposition (ECCE), 20-24 September 2015, Montreal, Canada, DOI: 10.1109/ECCE.2015.7310075;
- **Mingardi D.**, Bianchi N., Alberti L., "Optimal Choice of Stack Length and Conductors of Line Start Synchronous Motors", The 8th IET International Conference on Power Electronics, Machines and Drives (PEMD), 19-21 April 2016, Glasgow, Scotland, UK, DOI: 10.1049/cp.2016.0220;
- **Mingardi D.**, Bianchi N., Dai Pre' M., "Geometry of Line Start Synchronous Motors Suitable for Various pole Combinations", International Conference on Electrical Machines (ICEM), 4-7 September 2016, Lausanne, Switzerland;

Chapter 1

Introduction

This thesis is dedicated to the analysis, design and test of high efficiency electrical machines, with particular reference to machines with a rotor winding. Different aspects are discussed in the thesis. The bibliography on the covered subjects is deeply analyzed and it can be found in the citations. In this Chapter, the motivations of the work and its background are illustrated.

1.1. Background of the thesis

"HUMAN beings are able to modify intentionally the environment for their purposes such as agriculture or livestock farming. In the past such capability was somehow limited to their or the animal muscular power. The advent of fossil fuels started a new geological era. The availability of an inexhaustible source of energy from fossil fuel oxidation, raised exponentially the human capability to modify the environment, without considering the global effects. Climate change is due to anthropogenic greenhouse gases emissions, especially CO_2 [1]. 15 of the 16 warmest years on record have all fallen in the first 16 years of this century. No challenge poses a greater threat to future generations than climate change [2]. Exceptionally, the leaders of two of the most important religions release documents regarding the climate change and its effects on the population [3, 4]. This is a moment of opportunity, but also of great risk. The cost and difficulty of mitigating greenhouse-gas emissions increases every year, time is of the essence. Climate change will reduce the efficiency of the earth system to absorb the anthropogenic carbon perturbation, forming positive feedback loops in the climate system (i.e., amplifying externally induced perturbation) such as the carbon cycle [5] and the Earth albedo [6]. The land biosphere itself represents an increasingly positive feedback to anthropogenic climate change [7]. The risk is losing the possibility to mitigate the rise of temperature because of such positive-feedback in the climate system. It is clear that the energy sector play a critical role as the economic growth moves in the same direction of energy-related emissions. On one hand progresses must be made in developing cleaner and more efficient energy technologies. On the other hand, there is evidence that the "business as usual" scenario is not compatible with the possibility of limiting the rise in global mean temperature to $2°C$.

Machines driven by electrical motors consume around 2/3 of all the electrical energy. This thesis contributes to the development of more efficient electric motor systems.

1.2. Electrical motor system

All rotating electric machines are dynamic power converters. Either they convert mechanical power into electrical power (generators), or they convert electrical power into mechanical power (motors). A brief overview of the most common electrical motor topologies is carried out hereafter. Other motor topologies exist, but their description is out of the scope of this thesis.

The Induction Motor (IM) has been the workhorse of industry due to its ruggedness and low cost since its invention by N. Tesla [8]. Its working principle is that a multiphase AC stator winding produces a traveling field which induces voltages that produce currents in the short-circuited windings of the rotor. The interaction between the stator produced field and the rotor induced currents produces torque. As the torque at zero rotor speed is different from zero, the IM is self-starting. It can provide any torque up to the nominal one by varying its speed. The drawbacks of IM are the relative low Power Factor (PF) and efficiency. It is estimated that about 90% of all electrical machines are IM and the majority of them are fed from the standard AC power grid.

Direct-Current (DC) motors were used extensively in areas where variable-speed operation was required, as their flux and torque could be controlled easily by the field and armature current [9]. The developments in power electronics and digital control have triggered the widespread usage of Alternating-Current (AC) motors in Variable Speed Drive (VSD) systems. Adopting AC motors, the problems related to commutator and the brushes of DC motors, can be avoided. The availability of cheaper and effective power converters makes possible the use of VSD also for general purpose applications such as pumps, compressors, fans, machine tools and so on. As a matter of fact, several advantages derives from the adoption of VSD systems. In particular, they permit to save a large amount of energy at partial load condition, as only the power required for the process is provided to the motor. Another important advantage of VSD systems is the flexibility in the choice of the electrical motor type. The choice of an efficient motor reduces its environmental impact as well as its operational cost. This is particularly true in applications where a motor works for a large number of hours.

IMs is frequently adopted for VSD due to its ruggedness and low cost. It is forecasted that an increasing percentage of all electric motor systems will be fed through power electronics with IM [8].

Permanent Magnet (PM) synchronous machine (SyM) is considered the ideal machine. In this type of machines, torque is produced by the interaction between the PM flux and the stator rotating field. PM SyM exhibits high torque density, almost unity power factor (PF) and high efficiency due to the absence of excitation currents [10]. The use of fractional-slot winding in PM SyM allows a low torque ripple, an easy manufacturing and a good fault tolerance capability to be achieved [11]. In particular, interior PM motors with rare-earth magnets are used in electric and hybrid vehicles for their constant power operation and wide speed range [12].

The increase and the instability of rare earth PMs price, especially between 2010 and 2013, have directed the research towards rare earth free solutions. The current trend in the industrial and academic research highlights the Synchronous Reluctance Machine (SRM) as a good candidates for VSD applications [13, 14]. The principle of the reluctance torque production dates back to 19^{th} century [15]. Being its rotor made of iron only, the efficiency of SRM is high compared with the IM one as there are no rotor joule losses [16]. The SRM intrinsic disadvantages, such as high torque ripple, and low PF, can be mitigated by a proper design. Several recent studies contribute to the understanding of the SRM characteristics and its design peculiarities. PM assisted SRMs are very attractive because they combine the advantages of the pure SRM geometry and internal PM motors, leading to high saliency machines with a minimum, rare-earth free PM volume. This last feature is very desirable in a view of reducing the machine cost.

For fixed-load applications, supplying the motor by means of an inverter can only be justified if more efficient technologies than IM are adopted, such as SRM or PM machines. It should be mentioned that the presence of a power converter in a motor system represents an increase of its cost and a possible source of fault. Not to mention the current harmonics pollution in the power grid and the electromagnetic interference with the environment. For these reasons, direct-on-line fed motors will remain largely used for fixed-load applications. The line-start (LS) SRM was used in the second half of the last century when a fixed speed was desirable or necessary. When a SRM is fed directly on line, the rotor must be equipped with a short circuited winding that provide the torque necessary to accelerate it towards the synchronous speed. At steady state operation, currents don't flow in the rotor winding of LS SyM, being the rotor synchronous with the stator field. This, again, permits theoretically to increase the efficiency with respect the IM. LS PM SyM was later on considered due to the availability of rare-earth PMs. If the PM flux is high enough to provide an improved power factor, the stator joule losses can also be reduced. LS SyM have limitations on their line-start capabilities with respect to torque and external inertia and they are not suitable for all types of application. However, commercial LS SyMs have a maximum allowable load inertia up to 30 times the motor inertia, that is sufficient for the majority of the applications. It is worth noticing that, although LS SyMs are designed to be fed directly-on-line, they can be supplied also by a VSD. In particular, they can replace IMs fed by low-cost VSD. This is not always possible for conventional SyM, as they require rotor position sensing or estimation in VSD [17]. A lot of academic research was carried out to describe the complex phenomena involved in LS SyM operation [18, 19]. However, LS SyM represents nowadays only a small fraction of the motor market due to the complex design.

1.3. Legislations on efficiency

As part of a concerted effort worldwide to reduce energy consumption, CO2 emissions and the impact of industrial operations on the environment, various regulatory authorities in many countries have introduced or are planning legislation to encourage the manufacture and use of higher efficiency motors.

The International Electrotechnical Commission (IEC) has recently promulgated standards to unify motor testing standards, efficiency classes, and product labeling requirements. IEC does not regulate efficiency because this is a duty of the regional legislations. In particular, it is worth to introduce the following standards:

- IEC/EN 60034-2-1:2014 [20] specifies standard methods for determining losses and efficiency from tests (excluding machines for traction vehicles);
- IEC/TS 60034-2-3:2013 [21]. The objective of this specification is to define test methods for determining the additional harmonic motor losses of converter-fed IM. These losses appear in addition to the losses on nominally sinusoidal power supply as determined by the methods of IEC 60034-2-1;
- IEC/EN 60034-30-1-2014 [22] defines energy efficiency classes of line operated AC motors. It defines the following IE classes: the standard efficiency (IE1), the high efficiency (IE2), the premium efficiency (IE3) and the super-premium efficiency (IE4). As an example, Fig. 1.1 illustrates the standard efficiency classes for 4-pole motors at $50Hz$. A new class (IE5) is envisaged in a future edition of the stan-

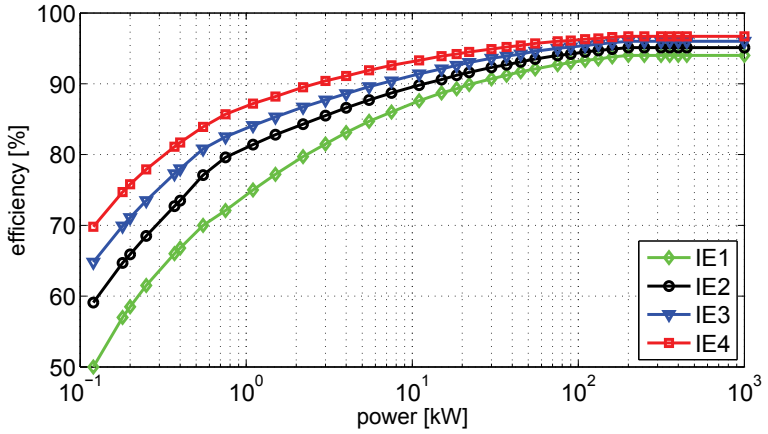

Figure 1.1: standard efficiency classes for 4-pole motors at $50Hz$ according to IEC/EN 60034-30-1-2014

dard even though technologies for IE5 are currently not well developed and not commercially available. The IEC/EN 60034-30-1-2014 widens the product range covered in the previous edition. The power range has been expanded to cover motors from 120 W to 1000 kW. All technical constructions of electric motors are covered as long as they are rated for direct-on-line operation. This includes all single- and three-phase low voltage IM, regardless of their rated voltage and frequency, as well as line-start permanent-magnet motors. A second part of this

standard series (IEC 60034-30-2) will be prepared for motors rated for variable voltage and frequency supply, such as SyM. The second part will also provide for harmonic voltage losses in motors capable of line operation when fed by frequency converters.

Governments introduce Minimum Energy Performance Standards (MEPS) setting mandatory minimum efficiency levels for electric motors. European Union MEPS stipulates that motors for direct-on-line operation between $7.5 - 375kW$ need to meet IE3 efficiency levels. Additionally IE2 motors can be placed on the market if they are driven by VSD. Motors smaller than $7.5kW$ can be IE2 until 1.1.2017. The rules that specify how efficiency should be determined and what efficiency classes should be used are based on the aforementioned standards.

From the manufacturers' point of view, it is not trivial to respect the requirements described above. On one hand, the possibility to further improve the design of IM is limited and mainly related to the use of new materials (copper cage, lamination with lower losses and improved B-H curve). On the other hand, a completely new redesign of the machine requires high investments. However, alternative technologies associated with IE4/5 efficiency-class motors have a high potential in energy-saving. This is particularly true for low rated power, because the lower the size, the higher the IM rotor loss component [16]. This supports the fact that a higher initial purchase cost of a more efficient motor will, in fact, bring higher savings within short payback periods.

As far as the direct-on-line fed motors are concerned, IE4-Class IM are already available. In applications that were exclusively limited to IMs, new developments in LS SyMs make them a cost-effective solution on a life-cycle basis. The LS SyMs available in the market exceed the IE4 Super-Premium limits, respecting the standard frame sizes [17, 23]. A significant increase of the number of LS SyM sold in the market is expected in the next decade, particularly in the power range under $7.5kW$.

1.4. Main goals of the thesis

The main goal of this thesis is to contribute to the development of high efficiency electrical motor systems from the machine design point of view. In particular, electrical machines characterized by rotor windings are treated in the thesis.

An important part of the thesis is dedicated to the LS SyM, as its difficult design remains a barrier to the diffusion of this type of motor. The challenge is to provide design techniques that take into consideration the main aspects of the machine reducing simultaneously the computation time. The importance of a careful design to achieve good performance from the electromagnetic and mechanical point of view is discussed. The aim is to demonstrate that the LS SyM technology is a good solution to meet the new efficiency classes. Since LS SyM must be competitive with the workhorse of electrical motors, the IM, techniques to achieve a robust design, suitable for the industrial production, are discussed. In particular, attention has been given to i) LS SyM types that are not available in the market at the date of writing this thesis, such as 2-pole, three-phase LS SyM and ii) small-size LS SyM ($< 7.5kW$), as they have the highest potential in efficiency improvements. However, the proposed analysis methods

are valid also for LS SyM with any size and number of poles. Measurements are used for the validation of the design techniques. The measurements are carried out on LS SyM prototypes as well as on its counterpart, the IM with the same stator. Another important goal of this work is to develop an analytical model to describe the effect of MMF harmonics in LS SyM. In literature, such a theoretical approach is still not found for LS SyM.

Design aspects related to electrical motors suitable for VSDs are also discussed, with particular reference to issues related to the high-frequency (HF) signal injection sensorless technique. The aim is to design the machine so as to extend the applicability of the HF signal injection sensorless technique. An asymmetric IM rotor cage allows information on rotor position to be achieved also at zero-speed. In the thesis, the performance achievable with such a rotor structure is experimentally quantified.
As far as the HF signal injection sensorless technique is concerned, the cross-saturation differential inductance of SyMs represents an issue, as it reduces the region in which such technique is effective. The knowledge of the properties of cross-saturation inductance is therefore essential to minimize any distortion effect on the position estimation. The properties of the cross-saturation inductance are deeply analyzed in the Thesis.
A rotor winding is added in Surface-mounted PM SyM to create a high frequency anisotropy that is useful to detect the rotor position by means of a HF signal injection. The losses due to such an additional rotor winding are studied: the aim is to investigate if the ringed-pole solution can be adopted also in large size-machines from the rotor losses point of view. FE analysis and analytical models are used to predict the losses.

Chapter 2

An overview of self-starting machines: Induction Motor and Line-Start Synchronous Motor

This Chapter provides an overview of electrical machines that can be fed directly-on-line, the IM and the LS SyM. As regards the IM, its main features and techniques of analysis such as equivalent circuit and different FE approaches are illustrated. As far as the LS SyM is concerned, the pull-in and pull-out torque concept, its equivalent circuits, the main design issues and its characteristic with respect the IM one are discussed.

2.1. Induction Motor

The principle of the IM was introduced by N. Tesla in 1886 [24]. The contemporary IM exhibits more elaborated topologies and better performance but the working principle has remained basically the same. A multiphase AC stator winding produces a traveling field which induces voltages that produce currents in the short-circuited windings of the rotor. In its electro-magnetic features, the IM is essentially a transformer [25]. The interaction between the stator produced field and the rotor induced currents produces torque.

The rotor winding can be either of the squirrel-cage type or wound type connected to slip rings. Especially in the low-power range, squirrel-cage winding is preferred as it is suitable for the industrial production. The rotor cage is in general made of aluminum: die-casted aluminum in low power IMs or of aluminum bars attached through brazing or welding processes to end rings. The casting process of aluminum uses the rotor lamination stack as a partial mold because the melting point of silicon steel is much higher [8]. With an uninsulated cage rotor, interbar currents can flow through the iron lamination.

The majority of IMs have skewed slots to reduce the cogging tendency and synchronous and asynchronous harmonic torques [26]. Skewing affects the stray-load and no-load losses. It creates additional flux components, which are loss-producing and lead

to an increase in leakage reactance. Interbar currents increase with skew, but harmonic currents flowing in the cage are reduced [27].

The drawbacks of IM are the relative low Power Factor (PF) and efficiency. Due to recent legislations on efficiency, several attempts have been done in order to increase the IM efficiency [28,29]. In order to increase the efficiency, rotor losses in squirrel cage IMs can be reduced by modifying the shape and size of the rotor bars [30]. Alternatively, copper can be used instead of aluminum for the rotor conductors [31, 32] Core losses can be reduced by decreasing the magnetic flux density in the iron of the machine. This can be done by increasing the volume or quality of iron used in the machine. This results in a trade-off between cost and efficiency.

It is estimated that about 90% of all electrical machines are IM and the majority of them are fed from the standard AC power grid.

2.2. Line-Start Motor

LS SyMs have a rotor cage for induction starting and PM or flux-barriers providing synchronous torque. Since the motor operates at a synchronous speed, the induced rotor currents at steady state are much smaller than in an IM and rotor joule losses are significantly reduced.

The pull-in torque represents the synchronization capability intended as the maximum load that can be synchronized at a given inertia. The asynchronous cage torque acts as pull-up torque, meaning that it is the one accelerating the motor from standstill towards synchronism. The final transition from asynchronous to synchronous speed is achieved in a dynamic way. During that half of the slip cycle when the synchronous torque is positive, rotor and load accelerate up to synchronous speed if the synchronous torque is enough. The pull-out torque represents the maximum load applicable at synchronous speed. If a load torque greater than the pull-out torque is applied, the motor lose the synchronism. The description of the pull-in process highlights the intrinsic LS SyM limit on their line-start capabilities with respect to torque and external inertia that can be applied. However, commercial LS SyMs have a maximum allowable load inertia up to 30 times the motor inertia, that is sufficient for the majority of the applications.

The LS SRM was used in the second half of the last century when a fixed speed was desirable or necessary. LS PM SyM was later on considered due to the availability of rare-earth PMs. Compared with the LS SRM, LS PM SyM exhibits higher efficiency and unity PF [33]. If the PM flux is high enough to provide an improved power factor, the stator joule losses can also be reduced. While in IM and LS SRM the pull-out torque is proportional to the terminal voltage squared, in LS PM SyM the PM component of pull-out torque is linearly dependent on the voltage. Consequently, LS PM SyM is less sensitive to voltage changes [34].

During starting LS SyM exhibits pulsating torques and currents whose amplitude is generally similar to those experienced in IM. However, while these pulsating torques and currents usually disappear for the IM after the initial electrical transient, they will persist in LS SyM until rated speed is achieved. This does not represents a problem in the vast majority of the applications. Associated with the pulsating torque are current

pulsations that are liable to demagnetize unprotected portions of PM. It is true that the rotor cage protects PMs from demagnetization during the transient thanks to its shielding effect, but a careful design is necessary to prevent PM demagnetization.

2.3. IM analysis

Let consider a standard IM in which a sinusoidally-distributed three-phase winding is in the stator. Assume a three-phase, sinusoidally distributed, short-circuited phase-wound rotor, although it can be demonstrated that the following equations are valid also for a squirrel cage rotor. In the hypothesis of:

- linear magnetic circuit;
- uniform airgap;
- negligible interbar current.

the fundamental equations of the IM are, in a generic reference frame fixed with the stator

$$\begin{cases} \mathbf{v}_s = R_s \mathbf{i}_s + \dfrac{d\boldsymbol{\lambda}_s}{dt} \\ \mathbf{0} = R_r \mathbf{i}_r + \dfrac{d\boldsymbol{\lambda}_r}{dt} - j\omega_m^e \boldsymbol{\lambda}_r \end{cases} \tag{2.1}$$

where $\mathbf{v}_s$ and $\mathbf{0}$ are the stator and rotor voltages, $\mathbf{i}_s$ and $\mathbf{i}_r$ are the stator and rotor currents, R_s and R_r are the stator and rotor resistances, $\boldsymbol{\lambda}_s$ and $\boldsymbol{\lambda}_r$ are the stator and rotor flux linkages, and ω_m^e is the electrical speed of the rotor (i.e., $\omega_m^e = p \cdot \omega_m$, having indicated with p the pole-pairs of the motor). Bold symbols refer to the space-vector notation. The stator and rotor flux linkages can be expressed as a function of the currents as

$$\begin{cases} \boldsymbol{\lambda}_s = \boldsymbol{\lambda}_{ss} + \boldsymbol{\lambda}_{sr} = L_s \mathbf{i}_s + M \mathbf{i}_r \\ \boldsymbol{\lambda}_r = \boldsymbol{\lambda}_{rs} + \boldsymbol{\lambda}_{rr} + = M \mathbf{i}_s + L_r \mathbf{i}_r \end{cases} \tag{2.2}$$

where the stator flux linkage is separated into a part ($\boldsymbol{\lambda}_{ss}$) due to the stator currents and one ($\boldsymbol{\lambda}_{sr}$) due to the mutual coupling with the rotor circuit. The same is for rotor flux linkage $\boldsymbol{\lambda}_r$, with obvious notation. A detailed analytical derivation of the inductances, represented in this work as L_s, L_r and M, can be found for example in [35] for a squirrel cage rotor.

The analysis of the IM, excited from balanced three-phase AC sources, was normally accomplished by means of the phase-equivalent circuit (EC), which was introduced by Steinmetz [36]. A brief description of its derivation is reported hereafter. Equations (2.1) and (2.2) can be represented by means of the dynamic EC of Fig. 2.1(a). In general, two mutually coupled circuits can be schematized with the EC of Fig. 2.1(b), where n is the transformation ratio, $L_s = L_1 + L_0$, $M = L_0/n$ and $L_r = L_2 + L_0/n^2$. Referring secondary quantities to the primary side, that is $v_s^{\backprime} = n v_r^{\backprime}$ and $i_s^{\backprime} = -\frac{i_r}{n}$, the circuit of Fig. 2.2 is achieved.

Depending on the choice of n, different forms of the EC can be derived. In particular, if $n = N_s/N_r$,that is, the actual ratio between the number of stator and rotor phase

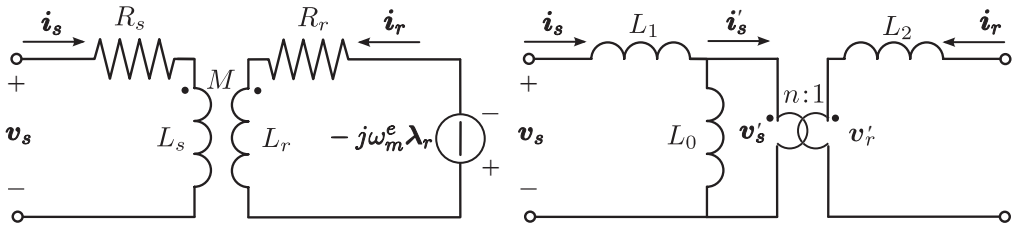

(a) equivalent circuit from equations (2.1) and (2.2)

(b) Equivalent scheme of a mutual inductor

Figure 2.1: Derivation of the IM EC

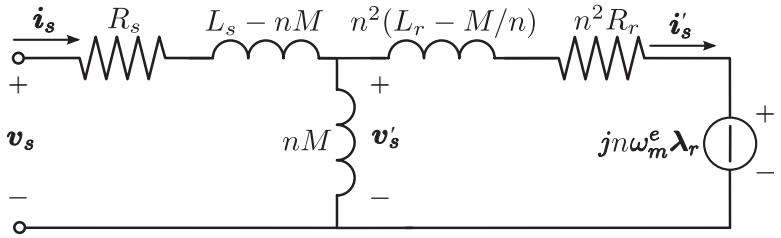

Figure 2.2: IM equivalent circuit: secondary quantities referred to the primary side

turns, the inductances L_1 and L_2 assume the physical meaning of stator and rotor leakage inductance. This EC is usually referred as "T-type". At steady state operation and after some manipulations of the second of equation (2.1), the EC of Fig. 2.2 can be drawn as in Fig. 2.3, having indicated with $L_{\sigma_s} = L_s - M\frac{N_s}{N_r}$ and $L'_{\sigma_r} = L_s - M\frac{N_r}{N_s}$ the stator and rotor leakage inductance and s is the slip. Upper case overline symbols denote steady state phasors.

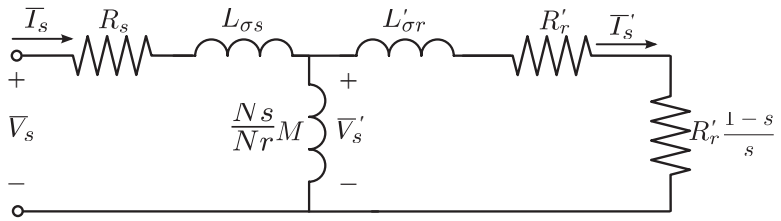

Figure 2.3: IM equivalent circuit at steady state

It is not always convenient to separate the stator and rotor contribution to the leakage inductance. As an example, when the IM parameters are determined from the no-load and the locked rotor tests, it is convenient to adopt an EC in which all the leakage inductances are on the stator or rotor side. Adopting for example $n = L_s/M$ the leakage inductance on the primary side of the EC of Fig. 2.2 is equal to zero. This EC is usually referred as "Γ-type".

It should be noted that the EC of the polyphase IM is, in general, the same as that of the transformer. The main difference lies in the expression for the resistance of the secondary side, as for the IM is associated with the slip s, while it is a constant in the transformer. The EC is very helpful in making calculations with fixed or varying parameters. The EC, written in this form, is valid for the fundamental magneto-motive

force (MMF) harmonic. However, it can be extended for the higher MMF harmonics. As indicated in [37], additional parameters are added in series to the fundamental parameters to consider effect such as skewing of the rotor bars, iron losses etc. Several papers have studied how to incorporate inter-bar current into the standard EC [38].

The computation of the EC parameters can be carried out analytically [39, 40], by means of FE analysis and experimentally with no-load and locked-rotor tests [25, 37]. The analytical approach gives a good understanding of the phenomena and it is appreciated for its speed, but it often lack in accuracy due to the inevitable approximations. FE analysis can consider effects such as iron saturation at various magnetizing currents and the current density distribution within the rotor slot at different rotor frequencies. Time-harmonic FE analysis is used to compute the EC parameters at the different slip frequencies [41]. However, this technique cannot reproduce those field harmonics due to the motional eddy currents [42]. For this reason, time-harmonic FE analysis cannot reproduce the effects of geometrical IM rotor details, such as open or closed rotor and cannot give any information about the current spectrum. On the contrary, the time-stepping FE analysis includes motional effects and provides the entire harmonic content of the stator current. However, the time-stepping FE analysis is more time consuming. Magnetostatic FE analysis is used under certain hypothesis to compute the steady state performance of IM [43]. A huge number of works in literature treats the analysis of the IM from several point of view. However, their detailed description is beyond the scope of this Section.

2.4. LS SyM analysis

Studies regarding the issue of three phase LS SyM synchronization was published many years ago. The analysis of the steady state and dynamic performance of LS SyM has been continued extensively, both on three-phase, [44–47] and single-phase machines [48–55].

Analytical calculations of LS SyM transient performance are usually carried out using a d– and q–axis model of the machine in which the rotor squirrel cage is represented by two equivalent coils with different parameters. The main LS SyM equations are reported hereafter. A sketch of the considered d– and q–axis reference frame is shown in Fig. 2.4. The flux barriers is aligned along the q–axis and the PMs flux is along the negative direction of the q–axis.

The d– and q– axis voltage equations of a LS SyM, expressed in the rotor reference frame, are

$$\begin{cases} v_{sd} = R_s i_{sd} + \dfrac{d\lambda_{sd}}{dt} - \omega_m^e \lambda_{sq} \\ v_{sq} = R_s i_{sq} + \dfrac{d\lambda_{sq}}{dt} + \omega_m^e \lambda_{sd} \\ v_{rd} = R_d i_{rd} + \dfrac{d\lambda_{rd}}{dt} = 0 \\ v_{rq} = R_q i_{rq} + \dfrac{d\lambda_{rq}}{dt} = 0 \end{cases} \tag{2.3}$$

where p is the number of pole pairs, R_q and R_q are the rotor resistances, λ_{sd}, λ_{sq}, λ_{rd}, λ_{rq} are the stator and rotor d– and q–axis flux linkages, i_{sd}, i_{sq}, i_{rd} and i_{rq} are the

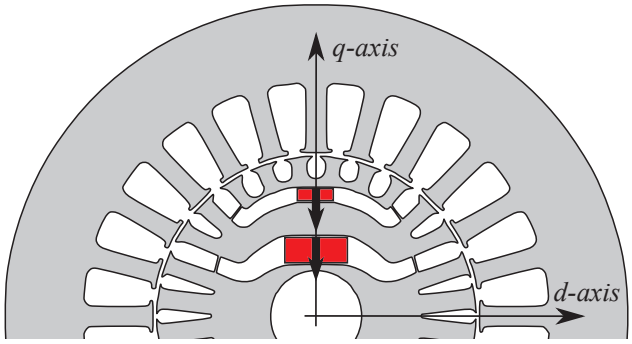

Figure 2.4: d– and q–axis reference frame

stator and rotor d– and q–axis current, respectively.

The stator and rotor flux linkages are expressed as a function of the currents as

$$\begin{cases} \lambda_{sd} = M_d(i_{sd} + i_{rd}) + L_{\sigma sd} i_{sd} \\ \lambda_{sq} = M_q(i_{sq} + i_{rq}) + L_{\sigma sq} i_{sq} - \Lambda_m \\ \lambda_{rd} = M_d(i_{sd} + i_{rd}) + L_{\sigma rd} i_{rd} \\ \lambda_{rq} = M_q(i_{sq} + i_{rq}) + L_{\sigma rq} i_{rq} - \Lambda_m \end{cases} \tag{2.4}$$

where M_d and M_q are the d– and q–axis mutual inductances and $L_{\sigma sd}$, $L_{\sigma rd}$, $L_{\sigma sq}$ and $L_{\sigma rq}$ are the stator and rotor d– and q–axis leakage inductances, respectively. The flux linkage Λ_m due to the PM is assumed to be constant.

The corresponding dynamic equivalent circuits of the LS SyM are shown in Fig. 2.5.

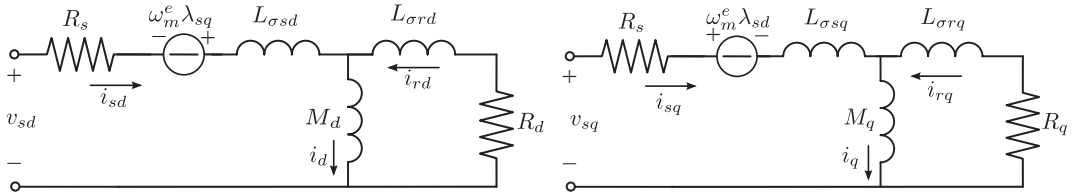

(a) d–axis (b) q–axis

Figure 2.5: Dynamic, T-type, $d-q$ equivalent circuits of LS SyM

The integration of (2.3), together with the mechanical equation

$$\frac{d\omega_m^e}{dt}\frac{1}{p} = \frac{T_{em} - T_{load}}{J} \tag{2.5}$$

allows the dynamic condition of LS SyM to be simulated. T_{em} is the electromagnetic torque developed by the motor, defined as

$$T_{em} = \frac{3}{2} p(\lambda_{sd} i_{sq} - \lambda_{sq} i_{sd}) \tag{2.6}$$

and T_{load} is the load torque. It is worth noticing that this model can be used also to simulate the dynamic of IM as it is a particular case of LS SyM in which the d– and q–axis rotor parameters are the same, as well as the d– and q–axis mutual inductances. For

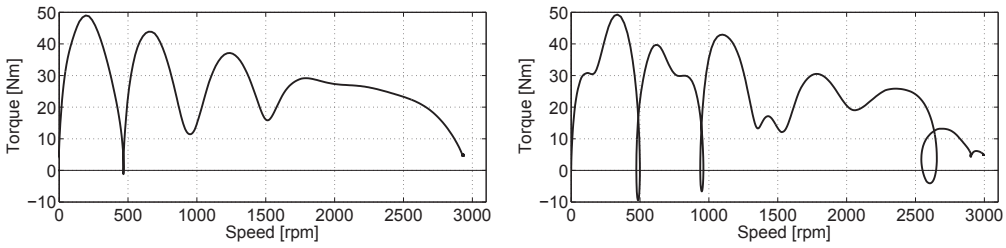

(a) Induction motor (b) Line start synchronous motor

Figure 2.6: Direct-on-line start-up

example, Fig. 2.6 shows the direct-on-line starting of an IM and a LS SyM, respectively, achieved by means of the model described above. It can be noted that, at the end of the start-up, the IM works with a certain slip, while LS SyM works at synchronous speed. Both of the motors exhibit high torque pulsation when directly started from the grid. However, the LS SyM exhibits additional torque pulsations due to the presence of the PM and the rotor saliency.

One drawback of this model is that it uses fixed value parameters. LS SyM is subjected to strong saturation level, especially during the start-up when high currents flow. Different sections of LS SyM magnetic circuit saturate independently, causing large and sometimes time-varying changes in EC parameters. Further, only the fundamental MMF harmonic is considered. Several papers in literature deal with more complicated EC in the attempt to describe the LS SyM performance. For example, in [56], an equivalent iron loss resistance is added to the EC. Other authors included the MMF harmonic effect into the equivalent circuit, see for example [51, 57] for a single-phase LS SyM. Different approaches have been developed by various authors to compute the LS SyM rotor parameters (rotor resistances and leakage inductances) [58–60]. Some of them are based on magnetostatic and time-harmonic FE analysis to take into account the machine nonlinearities. However, as mentioned above for the IM analysis, only time-stepping FE analysis can provide detailed simulations of the LS SyM behavior, including motional effects. As an example, time-stepping FE analysis is used in literature to evaluate PM behavior from the demagnetization point of view [61–65]. It is true that time-stepping simulations are very time-consuming and they are not suitable to be used in a design optimization procedure. For this reason, the analytical approach, with or without the support of simple FE simulations, is still appreciated in the first design step.

Without solving the LS SyM dynamic circuit, algebraic criterions for determining the pull-in capability was developed by different authors [33, 54, 66]. They are based on the separation of the torque components, which are described in the next Subsection.

2.4.1. LS SyM torque components

An analysis of the torque components in a three-phase LSSM is described in [19]. The influence of the magnetic saturation on the torque components is studied in [67].

The LS SyM torque during run-up is separated into components. They can be grouped into average and pulsating torque components, which are described hereafter. At asynchronous speed, current of different frequencies flows in the stator. The analysis of the torque components is carried out with a quasi steady-state analysis assuming sinusoidal variables. The stator currents due to the applied voltage and the stator currents induced by the PM rotation can be studied separately.

Average torque due to applied voltage

At first, the average torque due to the applied voltage is computed hereafter. The time derivatives in equations (2.3) are replaced with the operator $j(s\omega)$, $\omega_m^e = \omega(1-s)$ and $\Lambda_m = 0$, where ω is the electrical frequency in rad/s.

$$\begin{cases} \overline{V}_{sd} = R_s\overline{I}_{sd} + js\omega\overline{\Lambda}_{sd} - (1-s)\omega_m^e\overline{\Lambda}_{sq} \\ \overline{V}_{sq} = R_s\overline{I}_{sq} + js\omega\overline{\Lambda}_{sq} + (1-s)\omega_m^e\overline{\Lambda}_{sd} \\ \overline{V}_{rd} = R_d\overline{I}_{rd} + \overline{\Lambda}_{rd} = 0 \\ \overline{V}_{rq} = R_q\overline{I}_{rq} + \overline{\Lambda}_{rq} = 0 \end{cases} \tag{2.7}$$

By manipulating (3.1) and (2.7), the rotor current are expressed as a function of stator currents.

$$\begin{cases} \overline{I}_{rd} = -\dfrac{js\omega M_d}{R_d + js\omega(L_{\sigma rd} + M_d)}\overline{I}_{sd} \\ \overline{I}_{rq} = -\dfrac{js\omega M_q}{R_q + js\omega(L_{\sigma rq} + M_q)}\overline{I}_{sq} \end{cases} \tag{2.8}$$

Substituting (2.8) in (3.1), the stator flux to current relationship is

$$\begin{cases} \overline{\Lambda}_{sd} = \big[(L_{\sigma sd} + M_d) - \dfrac{js\omega M_d^2}{R_d + js\omega(L_{\sigma rd} + M_d)}\big]\overline{I}_{sd} = \dot{L}_{dp}\overline{I}_{sd} \\ \overline{\Lambda}_{sq} = \big[(L_{\sigma sq} + M_q) - \dfrac{js\omega M_q^2}{R_q + js\omega(L_{\sigma rq} + M_q)}\big]\overline{I}_{sq} = \dot{L}_{qp}\overline{I}_{sq} \end{cases} \tag{2.9}$$

where $\dot{L}_{dp}$ and $\dot{L}_{dp}$ are called operational inductances, which are complex numbers. assuming that $\overline{V}_{sd} = jV$ and $\overline{V}_{sd} = V$, the stator currents can be expressed as

$$\begin{cases} \overline{I}_{sd} = \dfrac{V\omega\dot{L}_{qp}(1-2s) + jVR_s}{\dot{D}} \\ \overline{I}_{sq} = \dfrac{VR_s - jV\omega\dot{L}_{dp}(1-2s)}{\dot{D}} \end{cases} \tag{2.10}$$

Where $\dot{D} = [R_s^2 + (1-2s)\omega^2\dot{L}_{dp}\dot{L}_{qp}] + j[s\omega R_s(\dot{L}_{dp} + \dot{L}_{qp})]$, which is a complex quantity too. Rationalizing $\dot{D}$, the real and imaginary part of the stator currents can be determined. It should be noted that the d– and q–axis stator currents are not, in general, phasors in time quadrature due to the rotor electromagnetic asymmetry.

The unbalanced rotor field can be split into forward and backward components [48]. The forward field rotates at the same speed of the stator field and produces stator currents of frequency f. The backward field rotates at a speed equal to $(1-2s)\omega$ and produces stator currents of frequency $(1-2s)f$.

The average torque component is

$$T_{em-avg} = \frac{3}{4} p \; Real(\overline{\Lambda}^*_{sd} \overline{I}_{sq} - \overline{\Lambda}^*_{sq} \overline{I}_{sd}) \tag{2.11}$$

where $\overline{\Lambda}^*_{sd}$ and $\overline{\Lambda}^*_{sd}$ are the complex conjugate of $\overline{\Lambda}_{sd}$ and $\overline{\Lambda}_{sd}$. Such an average torque component can be further split into two components adopting the double revolving theory:

- The forward average torque, which is always positive and it is the torque produced by a symmetric three-phase IM;
- The backward average torque, which is associated to the losses on the stator resistance caused by the backward field. It is positive below the half synchronous speed. This effect ceases, and changes sign at exact half-speed, i.e. this torque will brake the rotor [68, 69]. This phenomenon is also observed in IMs with asymmetrical rotor windings (one phase break) [70].

The average torque component is usually referred to as "cage" torque [19, 48, 68]. However, this should not create confusion. In fact, the backward average torque is due to the difference between the d– and q–axis ECs impedances. The cause of such an unbalance is due to the difference between rotor parameters (resistance and leakage inductance) or to the difference between the magnetizing inductances $L_{md} = L_{\sigma sd} + M_d$ and $L_{mq} = L_{\sigma sq} + M_q$, that is different from zero when the machine exhibits magnetic saliency. Considering a pure SRM without starting cage, $\dot{L}_{dp} = L_{md}$ and $\dot{L}_{qp} = L_{mq}$. Developing (2.11), it results

$$T_{em-avg-SRM} = -\frac{3}{4} p (L_{md} - L_{mq})^2 \frac{V^2 R_s \omega (1-2s)}{abs(D)^2} \tag{2.12}$$

It is worth noticing that the average torque of the SRM at $s = 0$ is always negative [71]. It corresponds to the backward average torque of a LS SyM at $s = 0$ because the rotor side of the ECs are open. The asymmetry of the rotor cage contributes to the backward average torque at $s \neq 0$.

Average torque due to PM rotation

The PM rotation causes currents of frequency $(1-s)f$ to flow in the stator winding. Such currents cause resistive losses in the stator winding acting as a braking torque. The analytical computation of the quasi-static PM breaking torque is derived by the short-circuited EC of a SyM, that is, with equation (2.7) considering $V = 0$ and $j\omega s = 0$. It yields, as a function of the slip s,

$$\begin{cases} I_{dm} = -\dfrac{(1-s)\omega R_s \Lambda_m}{R_s^2 + \omega^2 (1-s)^2 L_{md} L_{mq}} \\ I_{qm} = \dfrac{\omega^2 L_d \Lambda_m}{R_s^2 + \omega^2 (1-s)^2 L_{md} L_{mq}} \end{cases} \tag{2.13}$$

The flux linkages are $\Lambda_{sd-PM} = L_{md} I_{dm}$ and $\Lambda_{sq-PM} = L_{mq} I_{qm}$. Note that currents and flux linkages due to the PM are real numbers. The PM breaking torque is

$$T_m = \frac{3}{2} p (\Lambda_{sd-PM} I_{qm} - \Lambda_{sq-PM} I_{dm}) = -\frac{3}{2} p \frac{\omega_m^e \Lambda_m^2 R_s (R_s^2 + \omega_m^{e2} L_{M_d}^2)}{(R_s^2 + \omega_m^{e2} L_{M_d} L_{M_q})^2} \tag{2.14}$$

The PM breaking torque is always negative, it peaks at a low speed and it is small near synchronous speed. It reduces the positive average torque provided by the cage and reduces the LS SyM synchronization capability [33].

Pulsating torque

As far as the torque pulsations are concerned, components of double-slip-frequency and single-slip-frequency are present due to the reluctance and the PM, respectively. Their amplitude vary as a function of the slip. They are computed as

$$T_{puls-rel} = \frac{3}{4} p \; Abs(\overline{\Lambda}_{sd} \overline{I}_{sq} - \overline{\Lambda}_{sq} \overline{I}_{sd}) \tag{2.15}$$

and

$$T_{puls-PM} = \frac{3}{2} p \; Abs([\overline{\Lambda}_{sd} I_{qm} + \Lambda_{sd-PM} \overline{I}_{sq}] - [\overline{\Lambda}_{sq} I_{dm} + \Lambda_{sq-PM} \overline{I}_{sd}]) \tag{2.16}$$

Chapter 3

An improved FE-aided analytical method to predict the capabilities of Line-Start Synchronous Motor

This Chapter describes an analytical model of LS SyM combined with magnetostatic and time-harmonic FE analysis. The non-linear relationship between the main flux and the magnetizing current is computed with and without considering the cross saturation effect. The parameters of the machines are estimated as a function of magnetizing currents and rotor frequency and they are used to simulate the dynamic of the machine. To validate the model, experimental tests on a LS SyM prototype have been carried out.

3.1. Introduction

As pointed out in the previous Section, time-consuming time-stepping FE analysis has been used in literature to analyze the dynamic of LS SyM. On the other hand, the solution of analytical models are faster compared with those of time-stepping FE analysis. Analytical models give a good understanding of the complex phenomena involved in the dynamics of LS SyM, but they do not take into account phenomena such as local magnetic saturation, cross saturation or skin effect in rotor bars [72]. In addition, using fixed inductances in analytical models may lead to imprecisions [56], especially during the start-up.

To avoid the heavy approximations of linear magnetic circuit and rotor parameters constant with frequency, an analytical analysis combined with magnetostatic and time-harmonic FE analysis is described in this Chapter. The analysis is applied to three-phase LS SyMs. At first, the parameters of the machines are estimated by means of a FE analysis as a function of magnetizing currents and rotor frequency. The non-linear relationship between the main flux and the magnetizing current is computed using two approaches of different complexity so as to highlight their characteristics in term of computation time and precision of prediction. The parameters achieved from FE analysis are used to simulate the dynamic of the machine. The aim is to evaluate with reasonable precision the capability to reach synchronization, for given load torque and

inertia. The model does not require (time consuming) time-stepping FE simulations and any two-dimensional FE software can be used for the motor analysis. To validate the model, experimental measurements are carried out on a LS SRM prototype. The results of these tests are presented and compared with the predictions.

3.2. LS SyM dynamic considering saturation and rotor parameters as a function of the frequency

The proposed analysis is again based on equations (2.3). It is again assumed that the stator windings produce a sinusoidal field distribution along the airgap. However, the results obtained considering only the fundamental harmonic of airgap flux density can be considered a good approximation when the number of slots per pole per phase is quite high. This is a common choice in IM and LS SyM.

The considered Γ-type ECs are shown in Fig. 3.1. having indicated with R_{rd} and

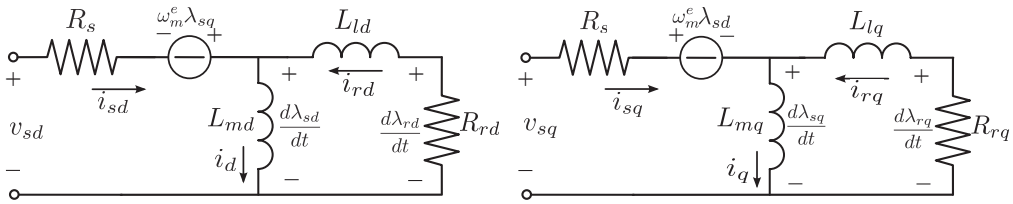

(a) d–axis (b) q–axis

Figure 3.1: Dynamic, Γ-type, $d-q$ equivalent circuits of LS SyM

R_{rq} the rotor resistances of the Γ-type ECs. The stator and rotor flux linkages are

$$\begin{cases} \lambda_{sd} = L_{md}(i_{sd} + i_{rd}) \\ \lambda_{sq} = L_{mq}(i_{sq} + i_{rq}) - \Lambda_m \\ \lambda_{rd} = L_{md}(i_{sd} + i_{rd}) + L_{ld} i_{rd} \\ \lambda_{rq} = L_{mq}(i_{sq} + i_{rq}) + L_{lq} i_{rq} - \Lambda_m \end{cases} \tag{3.1}$$

The parameters of the circuits of Fig. 3.1 are determined from FE analysis. The magnetizing inductances L_{md} and L_{mq} are computed by means of magnetostatic FE analysis, taking into account the non-linearity in the magnetic circuits. The computation is carried out with and without considering cross saturation effect. Rotor resistances and rotor leakage inductances are obtained from the $d-q$ model of the machine as a function of rotor frequency, as shown in detail [60].

Fig. 3.2 shows the flow-chart of the integration of equations (2.3). After setting the initial value of state variables, (1), for each integration step the rotor parameters are chosen as a function of rotor frequency, (2), and the rotor currents are computed from the flux linkages rearranging (3.1), (3). The magnetizing currents are computed with or without considering cross saturation effect as will be described later, (4). After that, the stator currents are achieved according to the equivalent circuits of Fig. 3.1, (5). Torques T_{em} is computed from (2.6) and the load torque T_{load} is, in the case of a fun or pump, $T_{load} = k\omega_m^2$, (6). At last, the state variables variations are computed

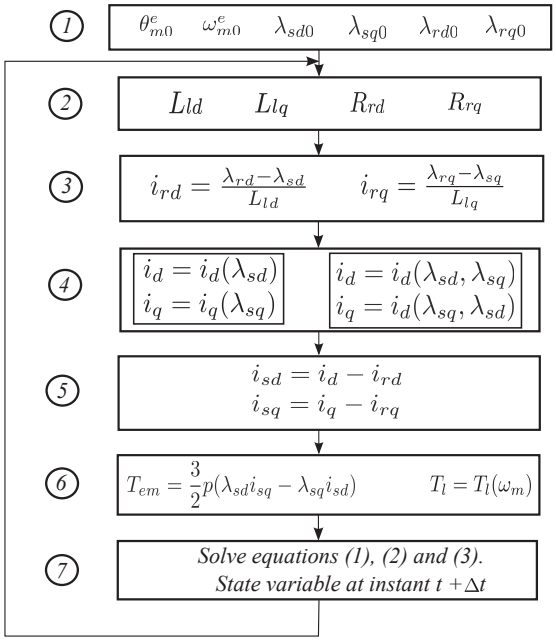

Figure 3.2: Flow chart of the dynamic analysis

from equations (2.3) and (2.5) and then integrated, (7). In the following Subsections, details on the parameters computation will be given.

3.2.1. Magnetizing current vs flux linkages

Generally speaking, both the magnetizing inductances L_{md} and L_{mq} are functions of both the magnetizing currents because of the cross saturation phenomenon. Two approaches are described: the first neglects the cross saturation, while the second includes the actual relationship between flux linkages λ_{sd}, λ_{sq} and currents i_d, i_q.

Solution without considering the cross saturation

To compute the relationship between currents i_d and i_q and stator flux linkages λ_{sd} and λ_{sq} without considering cross saturation, only two series of magnetostatic FE simulations are carried out. The first is performed by varying i_d, with $i_q = 0$, and computing λ_{sd} from the field solution. The second is performed by varying i_q, with $i_d = 0$ and computing λ_{sq} from the field solution. Since flux linkages are symmetrical with respect to the d– axis (the PM flux is along the q– axis), only positive d– axis currents are considered to reduce the computation time.

The obtained non-linear relationship between flux linkages and currents is used to compute the currents i_d and i_q flowing in the circuits of Fig. 3.1 for each integration step, as sketched in Fig. 3.3. The time to achieve the solution without considering cross saturations results to be very short. In details, a simulation of the dynamic start-up of a grid-connected LS SyM takes few seconds to be solved.

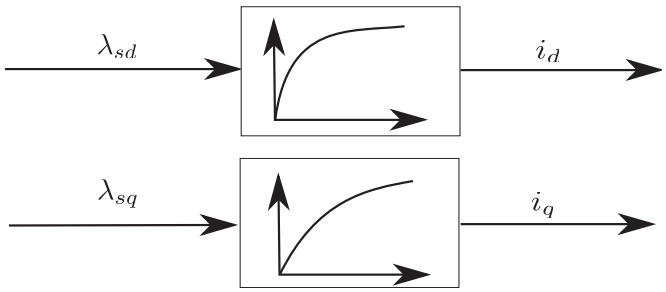

Figure 3.3: Sketch of the interpolation of magnetizing currents from the flux linkages without considering cross saturation

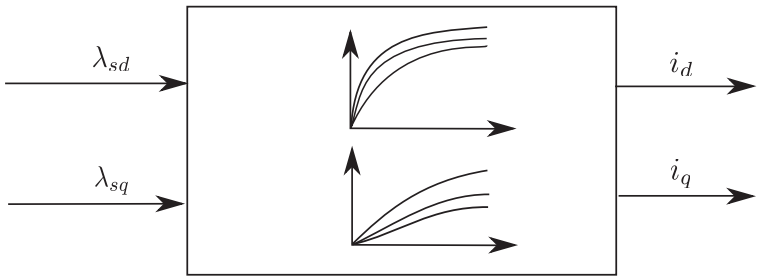

Figure 3.4: Interpolation of magnetizing currents from flux linkages with considering cross saturation

Solution considering the cross saturation

when the cross saturation effect is considered, the stator flux linkages λ_{sd} and λ_{sq} are functions of both the magnetizing currents i_d and i_q. A two-quadrant mapping in the $i_d - i_q$ plane is necessary. As above, due to the symmetry of the machine, only positive d– axis currents are considered. During the dynamic analysis, the currents will be computed by means of relationships $i_d = i_d(\lambda_{sd}, \lambda_{sq})$ and $i_q = i_q(\lambda_{sd}, \lambda_{sq})$ in each step of the integration, as sketched in Fig. 3.4.

3.2.2. Rotor parameters

Different approaches have been developed by various authors to compute LS SyM rotor parameters (rotor resistances and leakage inductances) [58,59]. The approach proposed in [60] has been chosen hereafter, since it considers rotor saliency between $d-$ and $q-$axis and the variation of parameters with rotor frequency as well.

To compute the rotor parameters, FE analysis is carried out by removing the PM magnetization and using a linear iron. If there are closed rotor slots or, in general, deeply saturated parts of the magnetic circuit, an equivalent permeability is used in those parts in order to keep the circuit linear, as shown in Fig 3.5. Fig. 3.6 shows the d– and q– axis flux lines when PMs are demagnetized. Time harmonic FE simulations at different rotor frequencies are carried out. From the field solutions, the equivalent parameters of the circuit shown in Fig. 3.1 are obtained. Fig. 3.7 shows the flux lines and the current density distribution at locked rotor, i.e. at rotor frequency $f_r = 50Hz$,

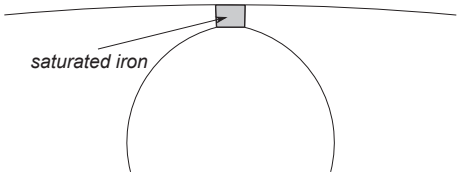

Figure 3.5: Saturated iron bridges

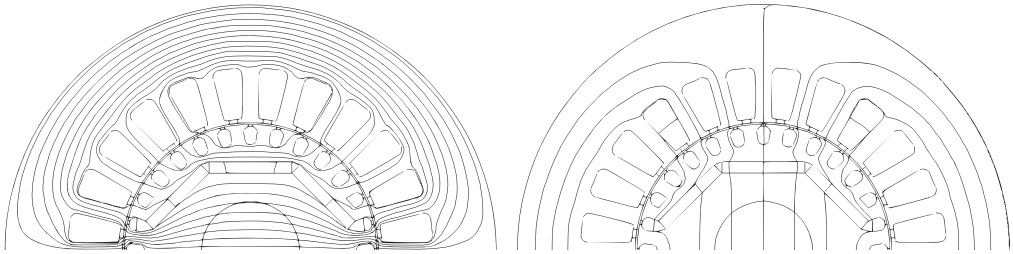

(a) d–axis current only (b) q–axis current only

Figure 3.6: Flux lines at no load, LS SRM (demagnetized PM)

of a $2-$pole, $1.5kW$ PM LS SyM. Fig 3.8 shows its rotor parameters as a function of the rotor frequency.

Other parameters not included in the 2-D FE analysis are analytically computed: at first the stator resistance R_s, then, the three-dimensional parameters, such as the skewing leakage inductance, end winding resistance and leakage inductance [73].

3.3. Dynamic analysis

The dynamic analysis gives the torque developed by the motor, including all the pulsating torque components. After synchronization, steady state performance can also be evaluated from torque, currents and flux linkages.

Fig. 3.9(a) shows the speed versus torque during the start-up and synchronization of the considered PM LS Sy. The simulation is carried out without cross saturation. The motor is loaded by an impeller whose inertia is about 3 times the inertia of the motor itself.

The number of conductors per slot n_{cs} affects significantly the dynamic behavior

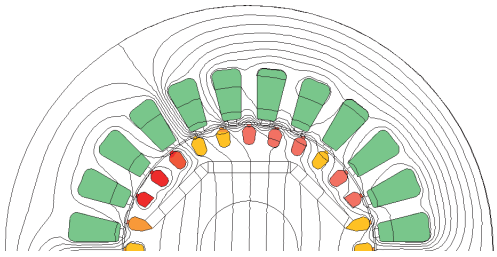

Figure 3.7: Flux lines and current density distribution at locked rotor

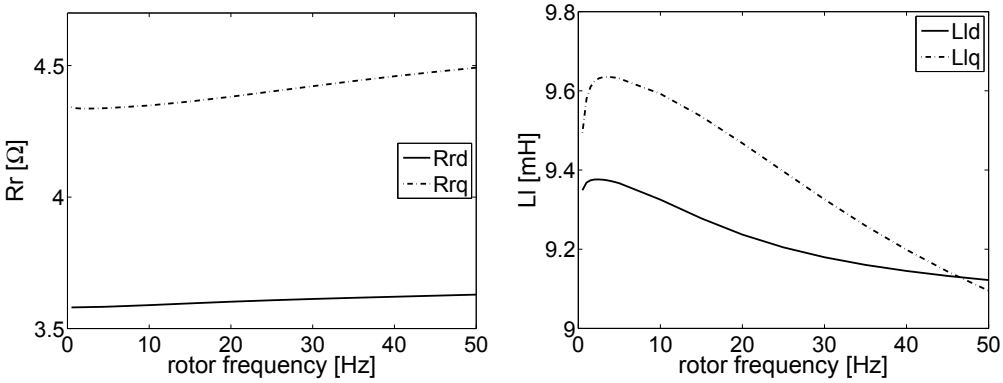

(a) Resistances (b) Leakage inductances

Figure 3.8: Rotor parameters as a function of rotor frequency

and steady state performance of LS SyM [74]. This is expected because the rotor parameters of the EC are proportional to the square of n_{cs} and directly proportional to L_{stk}. In [46] the relationship between the magnetizing inductance and the successful LS SyM synchronization is investigated. As an example, Fig. 3.9(b) shows that, if a reduced value of n_{cs} is considered, the start-up is improved. However, the transient current increases as well, together with the risk of PM demagnetization. Such risk must be properly evaluated. The analytical model provides the amount of the starting current, useful to understand if demagnetization occurs, but a more precise FE analysis must be carried out.

This result highlights a key feature of the proposed procedure. In fact further FE simulations are not necessary to analyze the behavior of LS SyM with different n_{cs}: various dynamic analysis can be carried out on the basis of the same field solutions. This is a great advantage with respect to the FE time-stepping approach as regards the computation time. Of course, this analysis can be used not only to search the proper n_{cs}, but also to test the impact of different stack length L_{stk}, loads, inertias and so on.

The proposed procedure can be used to estimate the detrimental effect of the temperature on the synchronization capability of LS SyMs by varying the stator resistance, PM coercivity and the conductivity of the rotor conductors.

To validate the proposed FE-aided analytical model, time-stepping FE simulations have been carried out. In particular, Fig. 3.10(a) and Fig. 3.10(b) compare torque and phase current, respectively, obtained at locked rotor condition and rated voltage. The analytical curves refer to the model including cross saturation effect. There is a satisfactory agreement between the results of the time stepping simulation and the proposed method results. The mean value of the torque computed at steady state at locked rotor are reported in Table 3.1, together with the amplitude of the pulsating torque due to the PM, T_{pm}.

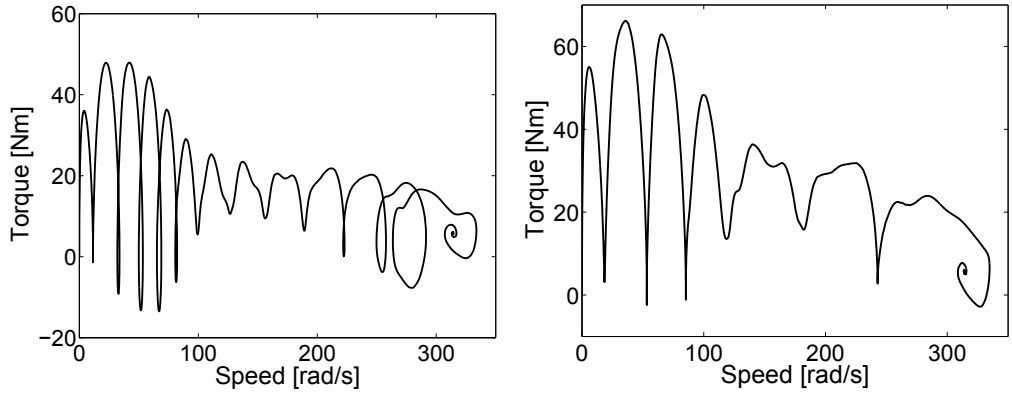

(a) $n_{cs} = 58$ (b) $n_{cs} = 46$

Figure 3.9: Torque vs speed during start-up, two different number of conductors per slot

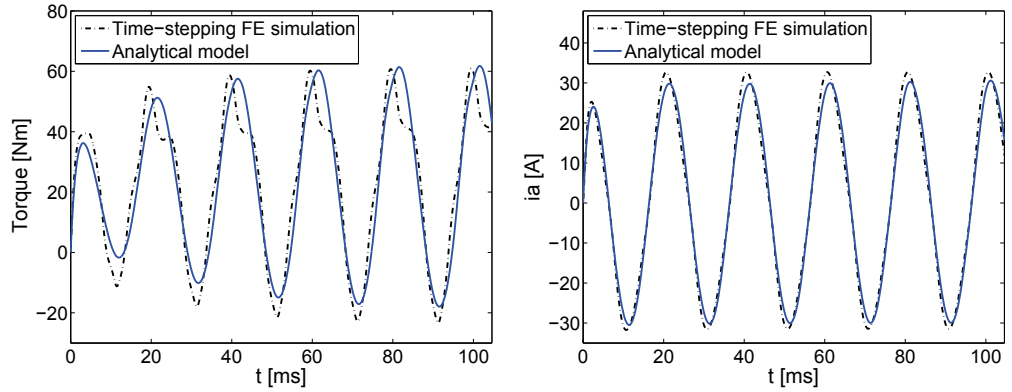

(a) torque vs time (b) current vs time

Figure 3.10: locked rotor test

3.4. Simulations vs tests

The proposed procedure has been validated by means of specific experimental tests, comparing their results with the predictions.

Table 3.1: Torque at locked rotor (*: value obtained considering cross saturation)

	Mean value $[Nm]$	Amplitude of Tpm $[Nm]$
Time-stepping FE	21.9	84.3
Analytical model	22.1 (+1%)	79.8 (−5%)
Analytical model *	21.6 (−1%)	79.4 (−5%)

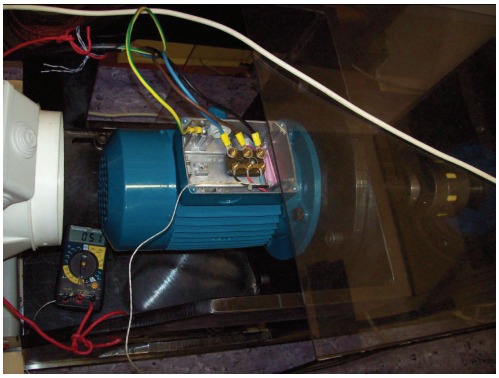

Figure 3.11: LS SRM prototype under test

Table 3.2: Main data of the LS SRM prototype

symbol	description	value	unit
p	number of pole pairs	1	-
Q_s	number of stator slots	24	-
Q_r	number of rotor slots	20	-
α_{sk}	skewing angle	15	deg
D_s	airgap diameter	65	mm
g	airgap	0.4	mm
D_e	external diameter	125	mm
L_{stk}	stack lenght	100	mm
J_m	rotor inertia	1.3	$g \cdot m^2$
V_n	rated voltage	400	V
τ_n	rated torque	4.8	Nm

3.4.1. Main data of the prototype

The experimental tests were performed on a LS SRM prototype available in laboratory whose data are reported in Table 3.2. Fig. 3.11 shows the experimental set-up. The prototype under test has been mounted on a test bench where a vector controlled IM is adopted as a load. The experimental equipment includes a torque-meter, an oscilloscope, a watt-meter and a variable transformer. The IM is fed by an inverter and controlled so as to reproduce the load torque.

Different total inertia J has been considered, whose values are reported in Table 3.3.

Table 3.3: Tested values of inertia

Inertia	$[g \cdot m^2]$
J1	5.9
J2	9.6
J3	24.3

Table 3.4: Synchronization voltage: tests versus improved analytical models (*: value obtained considering cross saturation)

	no load - J 1	no load - J 3	J 2	J 3
Analytical model* [V]	225*	415*	520*	585*
Analytical model [V]	205	410-	>570	> 570
TESTS [V]	220	420-480	530-550	> 550

3.4.2. synchronization capability

At first, the synchronization capability of the prototype is verified. The LS SRM has been supplied at different voltages, at no load and under rated load. These tests have been carried out at different inertias. The load, applied by means of the torque-controlled IM, is applied as a function of the speed as $T_{load} = k\omega_m^2$ to simulate a pump. The voltage required for synchronization is reported in Table 3.4, for both simulations and measurements. Referring to experimental tests, the lower and upper value in Table 3.4 correspond to the synchronization voltage at cold and hot motor, respectively. In the simulations, stator winding and rotor bar temperature has been fixed equal to $70°C$.

It is worth noticing that the prototype exhibits a low synchronization capability. At the nominal load and a load inertia corresponding to J 2 (about 7 times the rotor one), it synchronizes at a voltage greater than $500V$. Table 3.4 shows that, for low supply voltage, the models considering and neglecting cross saturation effect give similar results. At higher supply voltage, only the model considering cross saturation allows the synchronization capability to be satisfactorily estimated. This is because of the high saturation reached when the motor is supplied at high voltage. However, Table 3.4 shows that the synchronization capability of the motor is slightly overestimated. It is interesting to report that the synchronization voltage is very sensitive to variation of rotor parameters. This highlight the importance to include effects such as temperature and three-dimensional parameters in the parameters of the ECs.

The increase of the stator winding and rotor bar temperature has a detrimental effect on the synchronization capability. This behavior has been both observed (see Table 3.4) and predicted by the model. A further increase of rotor bar temperature leads to a reduction of the cage torque at low slip and hence to a worse synchronization capability.

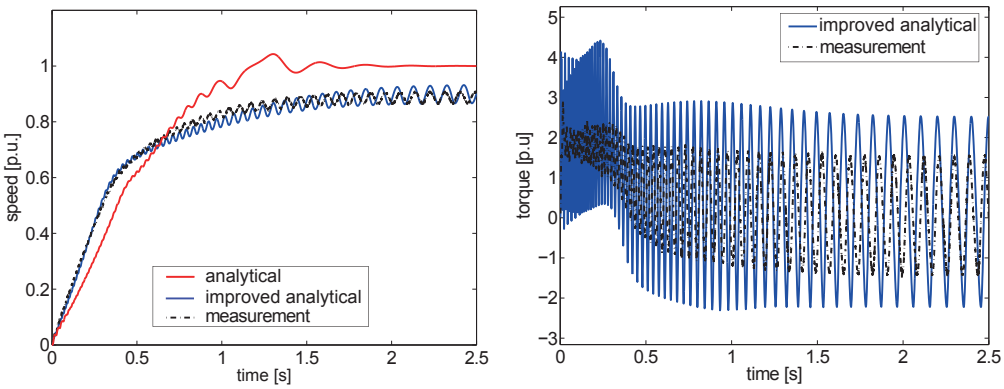

(a) Speed (b) Torque

Figure 3.12: Start-up, $V = 400\ V$

3.4.3. Start-up at nominal voltage: torque, speed and current

The prototype is started-up supplying it at rated voltage, when load is one fourth of the rated load and inertia J 3 is selected, see Table 3.3. The motor does not synchronize with the stator rotating field. Fig. 3.12(a) and Fig. 3.12(b) show the speed and torque behaviors, respectively, from both measurement and simulation with the proposed method, considering cross saturation effect. Fig. 3.12(a) reports also (red curve) the start-up achieved with constant rotor parameters and magnetizing inductance (unsaturated value). It is worth noticing that only the simulation with considering saturation and the variation of rotor parameters matches satisfactorily the measured one. In fact, the model with constant parameter predict wrongly a successful synchronization. This is an interesting comparison, as it demonstrates the improvement with respect the classical constant-parameter model.

Fig. 3.12(b) shows that there is a quite good correspondence between the measured and simulated mean torque. The analysis of the torque behavior highlights that the predicted amplitude of the oscillating reluctance torque by simulation is slightly higher than the measured one. Such an overestimation is due to the saliency ratio of the prototype, which is lower than the prediction due to the deformation of the flux barriers caused by the aluminum die casting process.

It is important to highlight that the torque labeled as "measured" in Fig. 3.12(b) refers to the torque produced by the motor under test. In dynamic condition, the torque produced by the motor under test is achieved from the torque measured by the torque-meter T_{tm} by [75]

$$T_{motor} = T_{tm} + J_m \frac{d\omega_m}{dt} \tag{3.2}$$

Fig. 3.13(a) and Fig. 3.13(b) show the current of the phase a during the rated voltage start-up shown in Fig. 3.12, obtained from simulation and measurement, respectively. Good agreement between measurement and prediction is observed. In particular, the current peaks are the same in both cases. Further, it is possible to distinguish the starting process into 2 steps from the phase current point of view: the first is characterized by a higher current. The motor starts from standstill, and the acceleration is rather

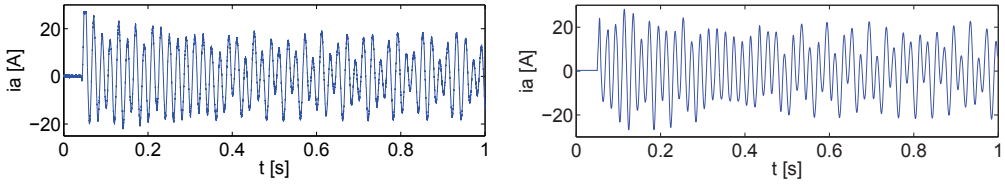

(a) Measurement (b) Improved analytical

Figure 3.13: Phase a current during start-up

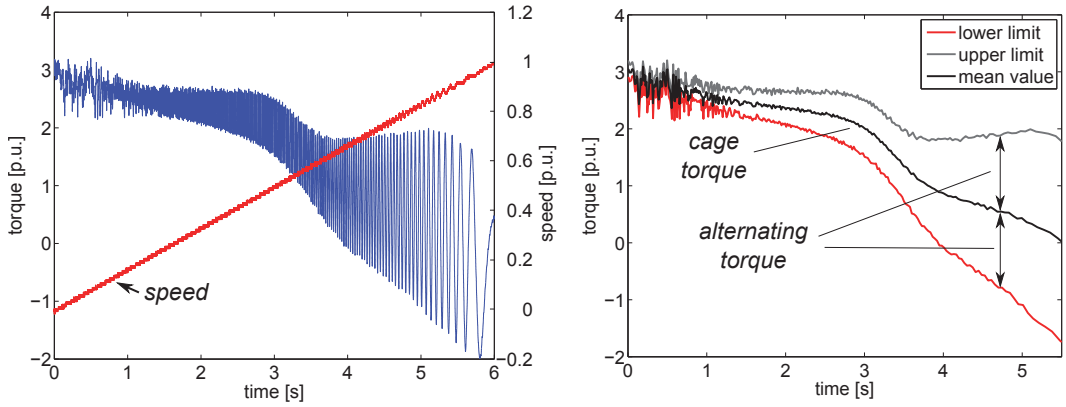

(a) Torque and speed (b) Torque components

Figure 3.14: Experimental measurements: speed and torque envelopes

high. In the second step, the motor approaches the synchronization speed. The electromagnetic torque is reduced and the motor fails to synchronize, causing the current distortion visible after $t = 0.5s$ of Fig. 3.13 both in simulation and measurement.

3.4.4. Quasi steady state characteristic

To measure the quasi steady state mechanical characteristic, the motor has been supplied by the line voltage and it is forced to increase its speed by means of the IM following a ramp. The speed variation is slower than the variation of electrical quantities. The measured torque and the speed are shown in Fig. 3.14(a).

From such a test, it is possible to segregate the "average" and the oscillating torque. As explained in Chapter 2, the first is associated to the forward and backward average torque and the second to the effect of the anisotropic rotor structure. In Fig. 3.14(b), the black line represents the average torque. The blue and red curves are the boundary of the upper and lower measured torque peaks, respectively. As expected, not only the average torque, but also the amplitude of the oscillating reluctance torque varies as a function of the speed.

The mean component of the torque decreases monotonously with the speed of the motor, see Fig. 3.14. It can be noted that a steep variation of the mean torque component occurs in the vicinity of half the synchronous speed. This corresponds to the torque characteristic of a motor which exhibits a high difference between the d– and q–

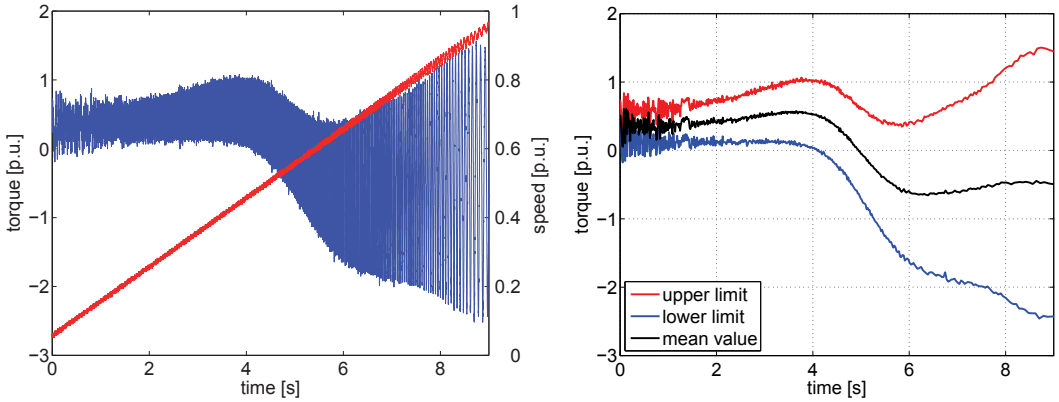

(a) Torque and speed

(b) Torque components

Figure 3.15: Experimental measurements: torque envelopes, pure SRM

axis EC impedance. To investigate this effect, another experimental test is carried out. The rotor of the prototype is replaced with a second rotor with the same lamination but without the rotor cage, that is, a pure SRM. The test to measure the mechanical characteristic is then repeated. The results achieved by this test are reported in Fig. 3.15.

As expected, the backward average torque component produces motoring torque below half speed and generating torque above, see (2.12). In the vicinity of synchronous speed, the average torque component due to the saliency is negative and its amplitude is about half the rated power. Especially when the stator resistance is relatively high, such as in small-size LS SyM, this results in a difficult synchronization.

3.5. Conclusions

An analytical method coupled to fast FE analysis has been developed and experimentally validated. It allows the start-up of LS SyM to be rapidly predicted, considering phenomena such as saturation, cross saturation and skin effect in rotor bars. As far as the complexity of the model is concerned, if the machine is not heavily saturated, the model without the cross saturation effect gives acceptable results in terms of synchronization capability and steady state performance. Such a model yields a remarkable reduction of the computation time: the FE mapping in the $i_d - i_q$ plane is not required and the dynamic analysis is very fast. Compared with the classical analytical model with constant parameters, the improved model predict satisfactorily the experimental results. The proposed tool is very useful for a designer to analyze the behavior of various geometries without the adoption of time-expensive FE models in the first design stage. From the experimental dynamic tests, the torque components have been segregated.

Chapter 4

Optimal selection of stack length and conductors of Line Start Synchronous Motors

This chapter presents an innovative technique of analysis of the steady state condition of LS SyM. The analysis is carried out in the $d-q$ reference frame. The main losses components are computed to estimate the efficiency. The simulated working point of LS SyM is represented in the I_d–I_q plane, as well al the limit of synchronization. From the analysis, parameters such as the number of conductors per slot and the machine stack length can be optimized. The working points measured on a LS SyM prototype are compared with the predictions.

4.1. Introduction

As showed in the previous Chapter, the number of conductors per slot n_{cs} affects the starting performance of LS SyM. It was showed that the normalized analysis allows to rapidly evaluate the effect of a variation of n_{cs} and also of the stack length L_{stk} from the synchronization point of view, without the need of further FE simulations.

As far as the steady state performance is concerned, similarly to IMs, L_{stk} and n_{cs} determine the LS SyM steady state performance in terms of efficiency and PF at a given load. When variable-load is applied, a compromise in the selection of n_{cs} has to be given [76]. Another solution is to arrange a multi-connection stator winding to provide different machine flux levels, as proposed in [77]. The LS SyM exhibits a higher power density than the IM. As a consequence, the LS SyM with the same size of an IM exhibits a higher efficiency for a given load torque, that can exceed the efficiency imposed by the IE4 efficiency class. It is therefore useful to select the minimum stack length L_{stk} to reach the desired efficiency. On the contrary, in [29], the core axial lengthening of an IM is considered a method to get a higher efficiency motor. In the same paper, the authors proposed a normalized analysis that allows the induction motor performance to be computed for a given lamination geometry. Then, n_{cs} is chosen so as to work at the maximum efficiency.

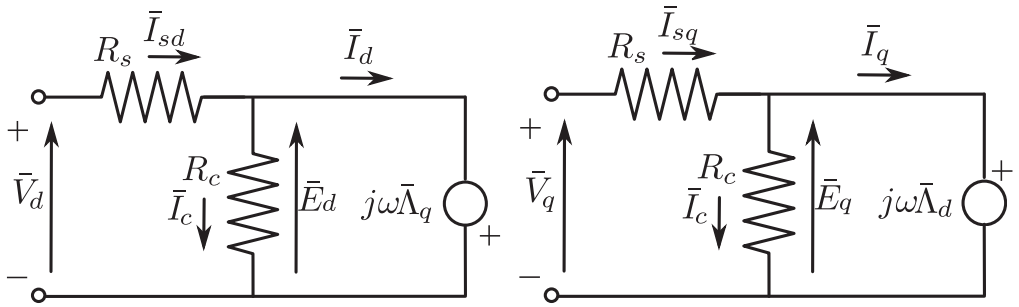

(a) d–axis (b) q–axis

Figure 4.1: LS SyM steady state equivalent circuits

Few papers in literature address a detailed analysis of LS SyM efficiency and PF variation with L_{stk} and n_{cs}, including experimental results. This part of the thesis aims to fill this gap. A normalized analysis of the LS SyM performance is presented, coupling FE analysis with analytical computations. The losses components are computed by means of FE. Then, the efficiency and the working point of LS SyM are represented in the I_d–I_q plane. Such an analysis is valid for any synchronous motor. In this thesis it is presented for LS SyM, which are grid connected and hence voltage level and frequency are fixed. This approach is suitable when a designer is interested in using the same lamination for motors of different size. In this case, a parametric analysis can be carried out to select the best combination of L_{stk} and n_{cs} to maximize the efficiency. The improved dynamic procedure described in Chapter 3 has been used to compute the feasible region the I_d–I_q plane from the synchronization point of view. The final part of this Chapter presents a series of experimental measurements on a LS SyM prototype to validate the predictions.

4.2. LSSM steady state analysis

The approach proposed hereafter is based on a per-unit FE analysis. The simulations are carried out for a motor with $L_{stk} = 1\ m$ and $n_{cs} = 1$. After that, the performance of a motor with any actual value of L_{stk} and n_{cs} can be rapidly achieved. The aim is to select the minimum axial length allowing a given efficiency to be reached, together with the optimal selection of n_{cs}, according to a given load and a given geometry. The PF variation as a function of the phase voltage or the load has been taken into account.

The analysis of the efficiency and PF of LS SyM is presented in the I_d–I_q plane. The considered d– and q–axis reference frame is that of Fig. 2.4. The LS SyM d– and q–axis equivalent circuits at steady state, which take into account the iron losses, are shown in Fig. 4.1. R_c is the resistance that represents the iron losses. The stator resistance R_s is computed as

$$R_s = \frac{\rho Q_s n_{cs}(L_{stk} + L_{ew})}{3A_{slot}k_{fill}} \tag{4.1}$$

where ρ is the copper resistivity at the considered temperature [78], Q_s is the number of stator slots, L_{ew} is the length of end windings, estimated as $L_{ew} = 2.5D_s/p$, where

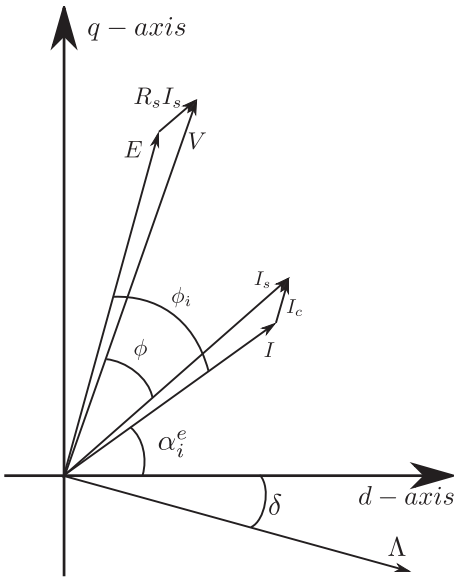

Figure 4.2: Steady state vector diagram of LS SyM

D_s is the stator inner diameter. A_{slot} is the slot cross section area and k_{fill} is the slot fill factor.

Referring to Fig. 4.1, E_d and E_q are the stator back emf and Λ_d and Λ_q are the stator flux linkages, given by d– and q–axis currents and PMs. The corresponding vector diagram at steady state is shown in Fig. 4.2.

The selected LS SyM lamination is analyzed in the I_d–I_q plane by means of FE analysis: the currents are imposed and the flux linkages are computed from the field solution. The iron losses are computed at 50 Hz by means of Steinmetz's formula, considering that the specific hysteresis losses and the specific eddy current losses are about the 70 and 30 % of the specific iron losses p_{si}, respectively. The specific losses are computed as

$$p_s = p_{si}\left(\frac{B_m}{B_{ref}}\right)^2 \tag{4.2}$$

where $B_{ref} = 1T$. The maximum value of flux density B_m is computed with FE in the tooth and in the back iron, respectively. Iron losses are computed as

$$P_{iron} = p_{st} \cdot k_{mt} \cdot G_t + p_{sbi} \cdot k_{mbi} \cdot G_{bi} \tag{4.3}$$

where p_{st} and p_{sbi} are the specific losses of the teeth and in the back iron, respectively, $k_{mt} = 2$ and $k_{mbi} = 1.5$ are the coefficients to increase the losses due to lamination cutting and punching, while G_t and G_{bi} are the weight of the teeth and the back iron, respectively. The electromagnetic torque has been computed as $T_{em} = \frac{3}{2}p(\Lambda_d I_q - \Lambda_q I_d)$, where p is the number of pole pairs. The Joule losses in stator conductors are $P_j = 3R_s I_s^2$, where I_s is the stator current. Losses in rotor bars are neglected. Mechanical losses P_{mech} depend on the bearing friction, air friction etc. In absence of a measured value they can be estimated by empirical formulas. In this work, the measured value is used.

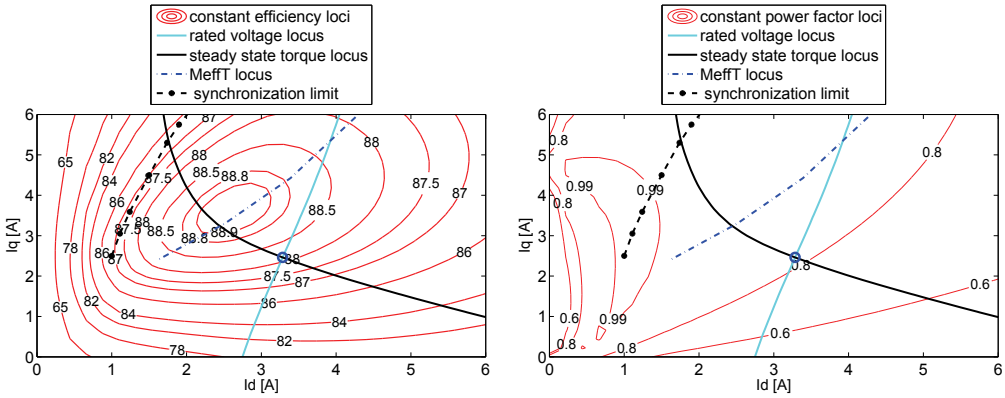

(a) Constant Efficiency loci (b) Constant PF loci

Figure 4.3: LS SyM: simulations in the I_d–I_q plane, $L_{stk} = 0.1\ m$ and $n_{cs} = 50$

The motor efficiency has been computed for each combination of I_d– and I_q–current as

$$\eta = \frac{T_{em} \cdot \omega/p - P_{mech}}{T_{em} \cdot \omega/p + P_{iron} + P_j} \tag{4.4}$$

The analysis is applied again to a $1.5kW$, three phase, LS SyM for pumping application, whose size is the same of that in Table 3.2. The stator of the corresponding IM ($n_{cs} = 50$) is used initially for the analysis. The normalized simulations are used to compute currents, flux linkages and iron losses for such a combination of L_{stk} and n_{cs}.

The constant efficiency loci is plotted in the I_d–I_q plane in Fig. 4.3(a) and the constant PF loci is shown in Fig. 4.3(b). The figures reports also the rated load torque curve (black solid line) together with the line-to-line voltage curve (light solid line). After synchronization, the motor operating point is given by the intersection between the load torque curve and the line voltage curve, as shown in Fig. 4.3 by the circle. Similarly to what is done in inverter-fed synchronous motor, where the current vector lies on the maximum torque per ampere (MTPA) locus, the idea is to design the LS SyM in order to achieve the maximum efficiency for a given load. In Fig. 4.3, the dot-dashed line represents the Maximum Efficiency per Torque (MEffT) locus. Fig. 4.3 also reports the limit of synchronization for a given inertia by the star curve. Such a limit forms an integral part of the analysis of a LS SyM and therefore must be considered. Section 4.4 illustrates how the synchronization limit is achieved. The area to the left of the synchronization limit constitutes a non-feasible zone, in which the motor is not able to synchronize with the stator field. It is convenient that such a synchronization limit is as far as possible from the MEffT locus, allowing a robust synchronization to be achieved. From Fig. 4.3(b), it is confirmed that the maximum efficiency loci does not correspond to the maximum PF loci.

It is worth noticing that Fig. 4.3 refers to the LS SyM with the same $L_{stk} = 0.1\ m$ and $n_{cs} = 50$ of the corresponding IM. With such values, the maximum efficiency achievable by the motor can not be reached. Varying L_{stk}, it is expected that the maximum efficiency loci will vary too. As an example, the lower L_{stk}, the lower the maximum efficiency due to the lower ratio between L_{stk} and L_{ew}. As far as n_{cs} is concerned, a higher n_{cs} is expected to move the line voltage curve to the left side of

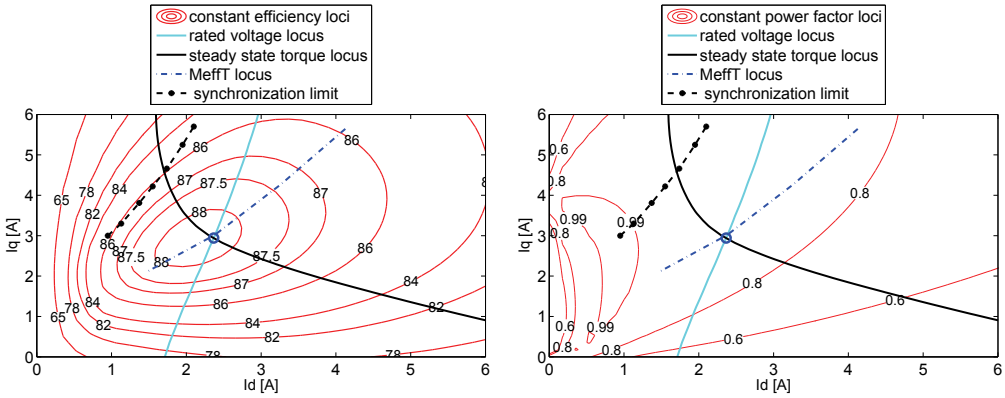

(a) Constant Efficiency loci (b) Constant PF loci

Figure 4.4: LSSM: simulations in the I_d–I_q plane, $L_{stk} = 0.085\ m$ and $n_{cs} = 62$

Fig. 4.3(a) due to the lower current necessary to excite the magnetic circuit. It is important to remember that with a higher n_{cs} the working point will be closer to the synchronization limit.

4.3. On the choice of L_{stk} and n_{cs}

As shown in the previous Section, the analyzed machine is not optimized for the given load. Depending on the design objective, the two considered variables (L_{stk} and n_{cs}) can be varied accordingly. Being fixed the motor load, one could be interested to find the minimum L_{stk} that allows the desired efficiency to be reached. Alternatively, a compromise in the choice of L_{stk} and n_{cs} can be reached if the motor is designed to work at variable load.

In the following, L_{stk} and n_{cs} are chosen so as the motor works at its maximum efficiency for the given load. L_{stk} has been reduced up to the load torque locus cross the center of the maximum efficiency zone. It results $L_{stk} = 0.085\ m$ and then n_{cs} has been properly chosen. Fig. 4.4(a) and Fig. 4.4(b) show how efficiency and PF have been modified. The efficiency in the new working point (about 88.2%) is lower than the maximum efficiency of the original motor (about 88.9%), but it is higher than the original working point (about 88%).

4.4. Synchronization limit

To represent the synchronization limit on the I_d–I_q plane, the following procedure has been used: being fixed n_{cs}, the minimum synchronization voltage has been computed for different values of load torque by means of the dynamic analysis of Chapter 3. At such a minimum synchronization voltage, the steady state I_d and I_q currents are reported in the I_d–I_q plane, as in Fig. 4.3. As an example, Fig. 4.5 illustrates the synchronization of the LS SyM at a voltage over and below the synchronization limit, respectively, at the rated torque and with inertia J 2 of Table 3.3.

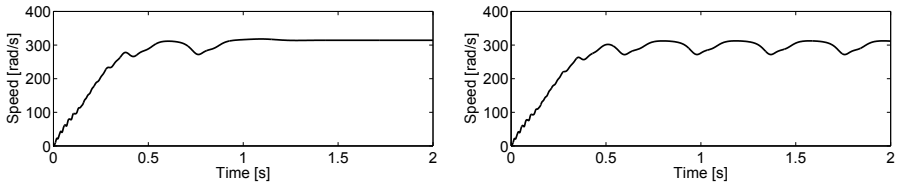

(a) $V = 300V$ (b) $V = 296V$

Figure 4.5: LSSM starting over and below the synchronization limit at rated torque: $n_{cs} = 50$, $L_{stk} = 0.1m$

4.5. Experimental measurements

The results from the proposed procedure has been validated by means of experimental measurements. The used prototype is the LS SRM prototype whose data are reported in Table 3.2.

The motor under test has been connected to the load through a torque transducer and supplied by a three-phase variable transformer. The torque-controlled master IM of the test bench is used to reproduce the effect of the load. To represent the working point of LSSM in the I_d–I_q plane, the rotor position has been detected by means of the encoder of the master motor. The three phase currents has been measured by external probes and conventional three-to-two-phase Park coordinate transformation is applied for both measured voltages and currents.

Fig. 4.6 shows the working points of the machine achieved with a voltage from $320V$ to $480V$ and with a load torque up to 8 Nm. Measurements are reported with circle marks. The simulations results are reported with cross marks and interpolated with lines. The actual winding temperature is measured so as to use the proper resistance in the analytical computations. The working points corresponding to voltage and load torque below the rated ones (see Table 3.2) are achieved at thermal steady state. For the other working points of Fig. 4.6, the temperature exceeded the temperature limit at thermal steady state. They are achieved with a fast test at the temperature corresponding to the nominal voltage and load torque.

It can be noted that there is a satisfactory agreement between simulated and measured results. In fact, the error of the predicted working point current remains below 3% in the whole I_d–I_q range. The error is relative to the actual measured current and it is higher for the working points corresponding to high voltage and load torque. The working points at the bottom of Fig. 4.6 are achieved at no load. Total mechanical losses due to the test bench, whose corresponding torque is measured as $T_{mech} = 0.3$ Nm, are the cause of the I_q current in such working points.

Fig. 4.7 shows the comparison between the efficiency measured by means of the direct method and the estimated efficiency for different load torque at the rated voltage. Good agreement is observed between the two curves of Fig. 4.7, confirming the validity of the proposed method. Consideration about the efficiency measurements uncertainty will be given in Appendix 5.6.1.

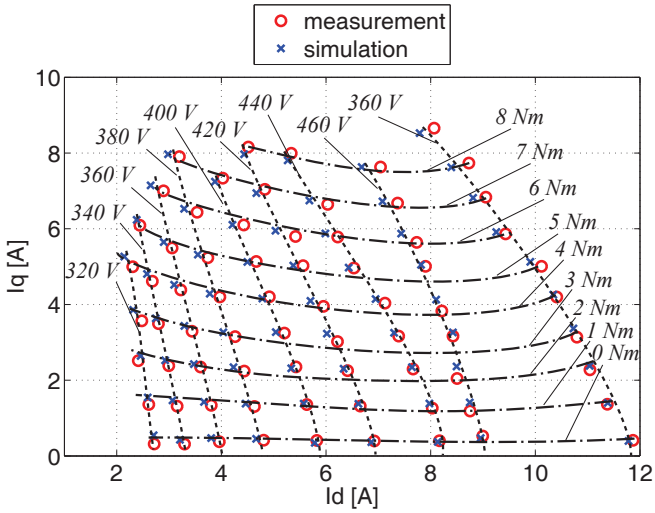

Figure 4.6: Working points of the machine: voltage from $320V$ to $480V$ and load torque up to $8Nm$. FE vs measurements

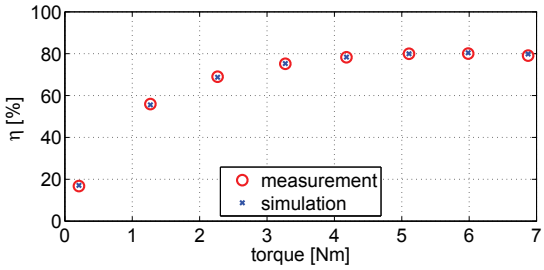

Figure 4.7: Efficiency as a function of load torque at nominal voltage ($V = 400\ V$). FE results vs measurements

4.6. Conclusions

A detailed analysis of the steady state performance of LS SyM has been carried out on the I_d-I_q plane. The procedure is carried out adopting per unit quantities so that the same FE field solutions are used to estimate the LSSM performance for both different stack length and different number of conductors per slot. This work shows that the proposed approach is an useful tool to select the minimum core axial length of an LSSM to get a given efficiency and minimizing the machine cost. It also highlights the importance to tune the stator winding to maximize the efficiency. Experimental measurements result in good agreement with the predictions, confirming the validity of the proposed approach.

Chapter 5

LS SyM design optimization and manufacturing

In this Chapter, the issues in LS SyM manufacturing are introduced, with particular reference to the die casting process. The possibility to apply the recent improvements in the SRM design to LS SyM is discussed from the manufacturing point of view. Together with the design techniques described in the previous chapters, a stochastic optimization is used to design the rotor lamination of a LS SyM to replace a low efficiency IM. After the automatic drawing of the rotor is developed, FE analysis is used to evaluate the optimization objectives considering the machine nonlinearities. Both steady state and dynamic performance are considered. Experimental measurements are carried out on a LS SyM resulting from the optimization and the results are compared with the predictions. From the experimental tests, an overview comparison between the IM and LS SyM performance is given, including thermal aspects. The tests will give a clear picture of the achievable performance of LS SyM in comparison to the IM.

5.1. Introduction

The recent research on SRM for VSD application has produced multi-barrier rotors exhibiting a high saliency ratio. In PM assisted SRM, the PMs are adopted to improve the power factor and the torque quality. PM-assisted SRM machines have a torque density that is comparable with that of other PM machines [79]. Rare earth free magnetic material can be inserted in the flux barriers, making possible the development of a low cost solution. These aspects pointed out new prospectives for the LS SyM design. However, from the manufacturing point of view, some constrains have to be satisfied in LS SyM design, limiting the effectiveness of certain rotor geometries. The LS SyM manufacturing issues will be discussed in the first part of this Chapter.

The viability of high efficiency LS SyM has already been demonstrated for fractional [53, 54, 80] and integral horsepower motors [44, 47, 81]. The majority of the papers in literature deals with 4-pole LS SyM. They are easier to be manufactured with respect 2-poles motors, since it is not necessary to surround the shaft with the PMs and/or the flux barriers. However, 2-poles motors are more suitable for centrifugal loads because

of their higher speed. Some authors proposed 2-pole solutions [47, 48, 50, 54, 55, 80, 82]. In [47], the authors demonstrate the utility of the reluctance-torque component on a $5kW$ 2-pole PM LS SyM. However, the convenience in adopting the LSSM technology in small-size ($1.5-2.2kW$), 2-pole motors on the large scale is still to be demonstrated. from the knowledge of the authors there are not small-size, 2-poles LS SyM in the marketplace.

Optimization algorithms coupled with FE analysis are nowadays used to design electrical machines, especially when the number of design variables are high such as in SRMs [83–86]. The process can be very time consuming depending on the number of candidate solutions and the non-negligible time for FE evaluation for each candidate. A proper choice of the algorithm and the problem conditioning is necessary to speed-up the simulations. The set of parameters used to describe the rotor geometry has a critical role in the design optimization: each parameter should have a reasonable impact at least on one objective. Useless parameters should be removed to keep the optimization process as simple as possible and to reduce the number of iterations needed for the convergence.

In this Chapter, the design of a new 2-pole, $1.5kW$, high efficiency (IE4 efficiency class) LS SyM is described. As pointed out in the Thesis introduction, this category of motor exhibits the highest potential in energy savings.

Several aspects are considered in the LS SyM design. A preliminary analysis of the asynchronous performance is carried out by means of the model described in Chapter 3 to guarantee the LS SyM synchronization in certain condition. As far as the synchronous performance are concerned, the choice of the number of flux barriers, the PM material and shape are discussed considering the design constrains. Then, an optimization algorithm is coupled with FE analysis to improve the synchronous performance. The stator winding is optimized by means of the procedure explained in Chapter 4. One of the most promising rotor geometry has been manufactured. Its performance has been measured on a test bench and compared with the predictions. Different PM volumes are tested in the same rotor structure, evaluating their impact on the dynamic and steady state motor performance. The performance of the LS SyM counterpart, the IM, is also measured providing an overview comparison between the IM and LS SyM performance.

5.2. Issues in the LS SyM manufacturing

The difficulty of designing a LS SyM is that flux barriers and starting cage have to share a limited space. Some constrains are:

- In a SRM, the magnetic bridges are quite thin and are designed to withstand only the centrifugal forces. Conversely, in a LS SyM, they are thicker so as to withstand the mechanical stress due to the die casting process. Additional magnetic fluxes are lost to saturate them, reducing the torque developed by the motor; for this reason LS SRM usually exhibits low performance. Alternatively, the SRM lamination can be used, filling the flux barriers with aluminium [72, 87].
- The high and uncontrolled starting current can demagnetize portions of PMs. In particular, the demagnetization of rare-earth-free magnetic material such as

Ferrite must be carefully evaluated. A higher PM width is required to avoid demagnetization. For small-size LS SyM, this is in contrast with the low rotor volume available due to the presence of the cage;

- A steep asynchronous torque versus slip characteristic, and therefore a low cage resistance, is essential to achieve a high synchronizing capability. However, the rotor resistance is usually higher than the equivalent IM cage due to the lower volume. This reduces the synchronizing capability.

In LS SyM, open rotor slots are preferred so as (i) to increase the cage maximum torque thanks to their lower leakage inductance, improving the synchronization capability; (ii) to reduce the q–axis inductance, increasing the reluctance torque component (iii) to reduce the leakage PM fluxes necessary to saturates the bridges.

The synchronizing capability of LS SRM is lower than that of the LS PM SyM [33]. The PM torque component is usually higher than the reluctance torque component. In addition, in LS SRM the pole slips occupy only 180 electrical degrees, instead of 360 degrees as in the LS PM SyM, leading to a smaller energy available for the synchronization. However, an increase of the PM flux is associated to two opposing effects:

1. an increase of the available synchronizing energy due to the higher PM torque;
2. an increase of the PM breaking torque.

These effects yield different behaviors depending on the machine size. In large size machines, the stator resistance is relatively low and the increase of the synchronizing energy dominates on the breaking torque. On the contrary, in small size machines, the magnet braking torque has a significant impact at almost-synchronous speed. In these cases, a reduction of the magnet "strength" can results in an overall increase in the synchronization capability [34].

5.3. Constraints of the project

5.4. LS SyM optimization

Some design constrains are listed in Table 5.1.

The stator lamination of the corresponding IM is used and the design is focused on the unconventional rotor geometry. The improvement of the stator geometry represents a further step in a motor optimization and it will be subject of future works. The same stator winding of the corresponding IM (that is, with the same n_{cs}) is considered and it can be changed in a second time.

The analysis is split in three main steps. They are the preliminary analysis, the synchronous performance optimization and the final validation.

Table 5.1: Main constrains for the LS SyM design

symbol	description	value	unit
p	number of pole pairs	1	-
Q_s	number of stator slots	24	-
α_{sk}	skewing angle	0	deg
D_s	airgap diameter	65	mm
g	airgap	0.4	mm
D_e	stator external diameter	125	mm
$D_{i,ring}$	end ring internal diameter	38	mm
D_{shaft}	Shaft diameter	25	mm
L_{stk}	stack lenght	100	mm
V_n	rated voltage	400	V

5.4.1. Preliminary analysis

Choice of the PM type

Sintered NdFeB PMs are used. Different approaches are found in literature to reduce the PM demagnetization. In [82], the rotor bar cross section was reduced to increase the rotor resistance and reduce the starting current, limiting the risk of PM demagnetization. However, this reduces the slope of the asynchronous torque characteristic and the synchronization results more challenging. Hereafter, a proper selection of the PM type, thickness and shape is used to avoid PM demagnetization and do not deteriorate the starting performance.

Considerations on the rotor cage

In the preliminary analysis, the maximum cage resistance (or minimum cage cross section) which guarantees the synchronization is determined by means of the FE-aided analytical method proposed in Chapter 3.

The cage cross section is increased up to satisfy the requirement that the LS SyM is able to synchronize a load inertia $J_{load} = 10J_m$ at a voltage corresponding to the 80% of the rated one.

5.4.2. Synchronous performance optimization

A multi-objective optimization algorithm coupled with magnetostatic FE is used to optimize the LS SyM synchronous steady state performance. Candidate solutions (which form the LS SyM population) are iteratively modified according to probabilistic rules. Multi-objective optimization algorithms search for a set of possible solutions according to the Pareto dominance criterion. This approach results in the family of the best compromise designs that provide the designer with a clear view of how much each objective is penalized by the improvement of the other one. Differential Evolution (DE) algorithm gives the best results in terms of convergence time and repeatability of the results in electrical machine optimization [85]. For this reason, a multi-objective DE algorithm is used in this work.

The two optimization objectives are the maximization of the torque per Joule loss ratio and the reduction of the torque ripple.
The torque ripple is computed as

$$T_{ripple} = \frac{T_{max} - T_{min}}{T_{avg}} \tag{5.1}$$

where T_{max}, T_{min} and T_{avg} are the maximum, minimum and average torque, respectively. The torque is evaluated by means of n magnetostatic FE simulations in different equally-spaced rotor positions. The rotor position is varied within an interval of 60 electrical degrees, corresponding to the torque waveform periodicity. Other authors evaluated the motor torque in a reduced interval, that is, the stator slot pitch, to reduce the number of FE simulation per candidate [85]. This was chosen because the stator slot pitch is representative of the most significant harmonic component of the torque ripple.

The LS SyM design optimization is complex since the maximum torque is a function of the current angle, which, in turn, is a function of the design parameters. Different approaches have been proposed in literature to face this problem. Some authors carried out an additional search of the MTPA current angle for every candidate design [83] and others included the current angle in the parameters to be optimized by the algorithm [86]. Hereafter, the first approach has been used.
The current amplitude is fixed to that of the corresponding IM at rated torque.

A set of 5 parameters has been used to describe the LS SyM according to Fig. 5.1. They are:

- The angular position of the flux barrier θ_{b1} (which terminal parts are rotor bars);
- The number of "q–axis rotor slots", see Fig. 5.1;
- The angular position of the first "q–axis rotor slot" θ_{c1};
- The depth of the "q–axis rotor slots", h_c;
- The tooth width between "q–axis rotor slots", t_c.

The machine resulting from the automatic drawing exhibits central symmetry. As a result, the rotor cage is constituted by an even number of rotor slots. The upper and

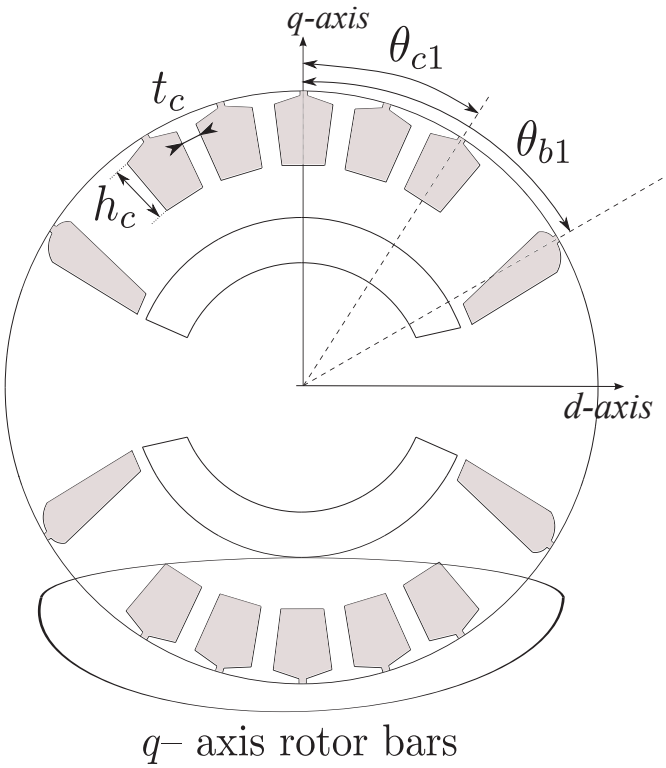

Figure 5.1: Description of the parameters used for the automatic LS SyM design

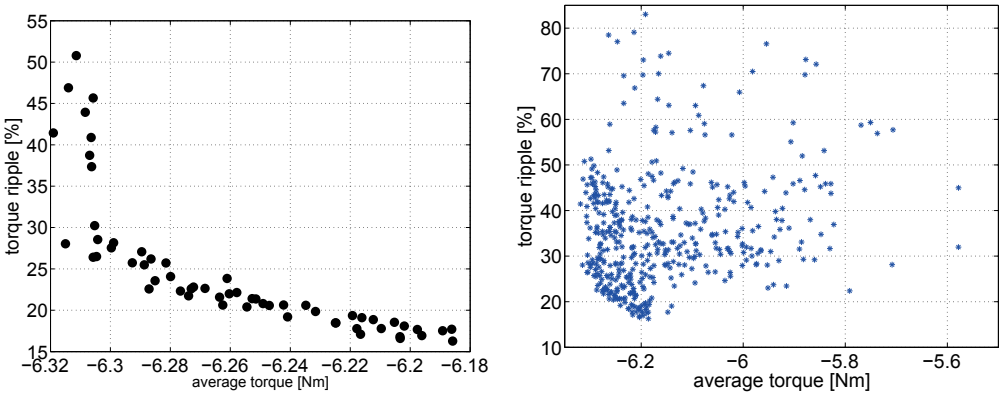

(a) Front after 18 generations

(b) Characteristics of all the simulated individuals

Figure 5.2: Optimization results

lower limits of the parameters are defined (i) on the basis of the minimum cage cross section resulting from the preliminary analysis and (ii) on the basis of the geometric feasibility.

The results reported in Fig. 5.2 refer to the DE algorithm after 18 generations. The Pareto front after 18 generations is considered to be satisfactory and the optimization has been stopped. It includes candidates which exhibit a $T_{ripple} < 20\%$. It is convenient to remember that also the pump impeller exhibits a intrinsic and unavoidable torque

ripple. Furthermore, as explained in the next Section, unpredict component of torque ripple arise due to the manufacturing process. For these reasons,

As far as the average torque is concerned, it is significantly higher than the IM at the same current level (about $4.9Nm$, corresponding to $1.5kW$). This is expected due to the higher torque density of LS SyM compared than IM.

Fig. 5.2(b) reports the characteristics of all the simulated candidates. From Fig. 5.2(b), it is confirmed that unacceptable torque ripple characterize some candidates (which are not along the Pareto front). A great improvement of both the objectives are achieved from the optimization.

A pareto optimal candidate design, which exhibits a good compromise between the two objectives, is selected for the final validation stage.

5.4.3. Final validation

A further analysis on the selected candidate has been carried out.

At first, the steady state condition is evaluated by means of the procedure explained in Chapter 4. In particular, n_{cs} is chosen so as to work at the maximum achievable efficiency for that given geometry.

Then, the dynamic performance of the optimal LS SyM are evaluated by means of the FE-aided analytical method of Chapter 3. It is expected that the synchronization capability is higher, meanly because of two reasons:

- The optimal LS SyM exhibits a greater cage cross section, which means a low rotor resistance;
- The synchronous torque of the optimal design is likely to be higher than that of the rough LS SyM.

However, it is convenient to carry out this test having tuned n_{cs} to reach the maximum efficiency and consequently the rotor parameters have changed with respect the preliminary analysis.

The last step of the confirmatory analysis deals the time-stepping FE analysis of the optimal LS SyM. The start-up of the machine is simulated up to reach the steady state synchronous condition. This test aims to:

- confirm the proper synchronization of the machine;
- verify the absence of PM demagnetization;

It is worth noticing that the time-stepping FE simulation is time-consuming and for this reason it is used only in the final analysis on the optimal LS SyM.

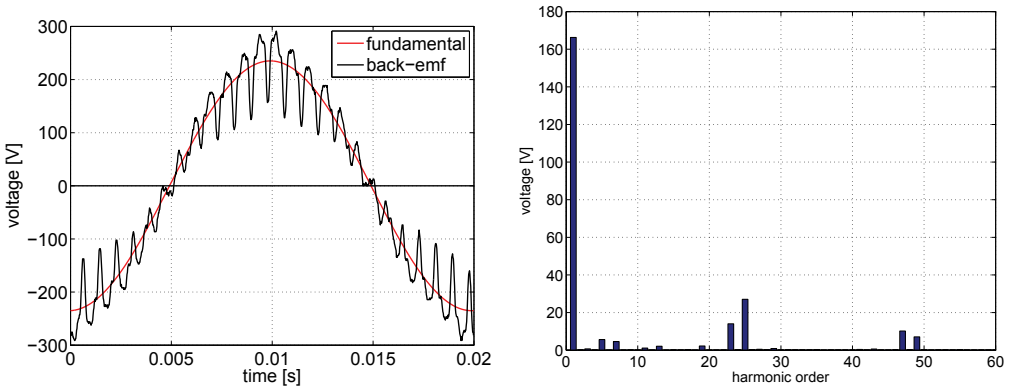

(a) Line-to-line back-emf

(b) rms value of the back-emf harmonics

Figure 5.3: Back-emf at $3000rpm$

5.5. Experimental measurements on prototype

Experimental tests on the prototype have been carried out and they are described in detail in the following Subsections. They are:

- Back-emf measurement;
- Determination of the magnetic characteristics;
- Synchronization tests;
- Synchronous torque measurements;
- Efficiency measurement.

It is worth reporting that a slight reduction of the flux barrier width occurs due to the die casting process. However, such a deformation does not prevent PMs to be inserted within the flux barriers. After the die casting process, the rotor has been turned on a lath.

5.5.1. Back-emf

The prototype has been mounted on a test bench in which a speed-controlled IM is used as master motor or brake. The LS SyM is dragged by means of the master motor up to the rated speed of $3000rpm$. The line-to-line back-emf voltage have been measured and it is shown in From Fig. 5.3. With the same test, the mechanical losses of the prototype has been measured by means of a high precision torque meter.

The fundamental back-emf harmonic exhibits an rms value lower than the nominal voltage (166 V vs 400 V). This is due to the low PM volume buried in the rotor structure. It is worth to report that the amplitude of the back-emf remains unchanged after all the tests described in this Chapter, confirming the absence of PM demagnetization.

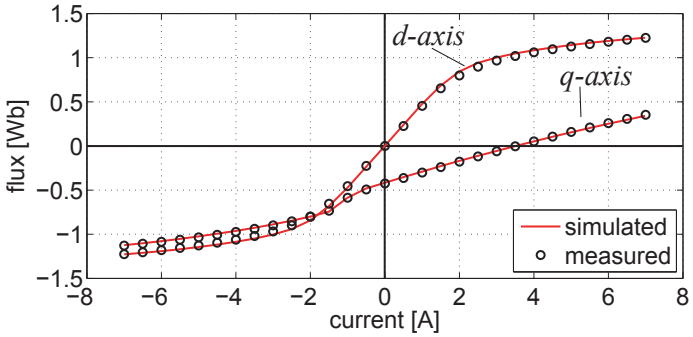

Figure 5.4: Measured magnetic characteristics

5.5.2. Determination of the magnetic characteristics

The aforementioned test bench is used also to measure the machine magnetic characteristics $\Lambda_d(I_d, I_q)$ and $\Lambda_q(I_d, I_q)$. Both master and slave motors are supplied by two inverters. The currents references are imposed through a dSPACE board DS1104. The magnetic characteristics can be obtained at steady state applying the d- and q-axis currents and measuring the q- and d-axis voltage respectively. During these measurements, the LS SyM prototype is dragged by the master motor at constant speed. At steady state condition, it results

$$\begin{aligned} \Lambda_d(I_d, I_q) &= \frac{U_q - R_s I_q}{\Omega_{me}} \\ \Lambda_q(I_d, I_q) &= \frac{U_q - R_s I_q}{\Omega_{me}} \end{aligned} \tag{5.2}$$

To avoid the influence of the stator resistance, the measurement is carried out with both a positive and a negative current for the d- and q-axis. The combination of (5.2) with the two currents yields an expression of the flux linkages which are not function of R_s. A similar result would be achieved by measuring the flux linkages at two different rotor speeds.

The measured d- and q-axis flux linkages are reported in Fig. 5.4, together with the results from FE analysis. Fig. 5.4 refers to the characteristics achieved without considering the current of the other axis, that is, $\Lambda_d(I_d, 0)$ and $\Lambda_q(0, I_q)$. The comparison confirms the accuracy of the results predicted by FE analysis. The measurements are then repeated considering the cross saturation effect, but the results are not reported here for the sake of brevity.

5.5.3. Synchronization tests

To evaluate the synchronization capability of the prototype, the same test bench of the previous experimental tests has been used. The prototype has been supplied by the grid and the master motor is torque controlled so as to reproduce the effect of the load, with $T_{load} = k\omega_m^2$.

This test has been carried out after reaching the thermal steady state (about three hour operation). The evaluation of the stator winding temperature at steady state is described in Subsection 5.5.5. Fig. 5.5 shows torque and speed measured during the start-up at nominal voltage at rated torque. As explained in Section 3.4, the torque

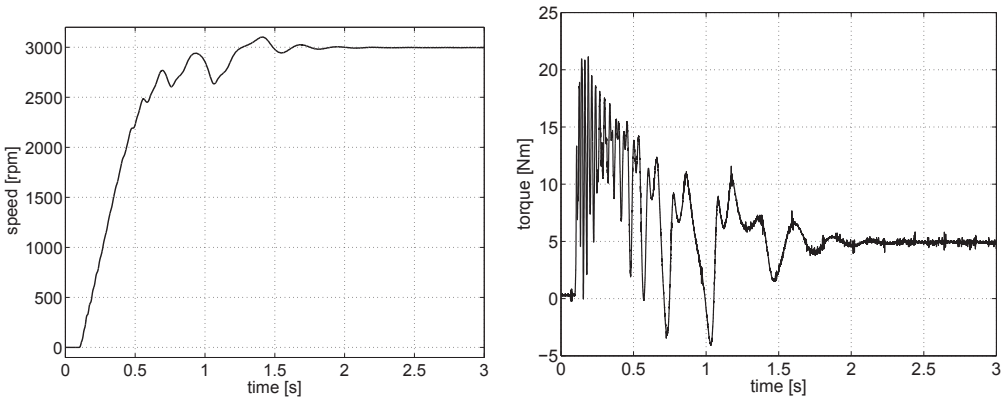

(a) speed (b) torque

Figure 5.5: start-up at nominal voltage at rated torque

labeled as "measured" in Fig. 5.5 is computed as (3.2).

It is worth noticing that this test confirms the good synchronization capability of the prototype. It is able to synchronize at rated load a load inertia which is about 18.7 times higher than the prototype inertia ($J_m = 1.3gm^2$).

5.5.4. Synchronous torque measurements

The tests illustrated in this Subsection are carried out on a test bench in which the master motor is connected to the prototype through a non reversible gear box (ratio 1:59) and a torque meter.

The torque versus current vector angle of the prototype has been measured. The current amplitude has been fixed to the rated one. For each value of the current vector angle from 0 to 2π, the torque has been sampled for the whole rotor revolution. The average value of such a torque has been reported in Fig. 5.6(a) as a function of the current vector angle. As a first approximation, the segregation of the torque components can be achieved. The first harmonic component is referred to as PM torque. The second harmonic component is referred to as reluctance torque. It is worth noticing that the reluctance and the PM torque components exhibit the same amplitude.

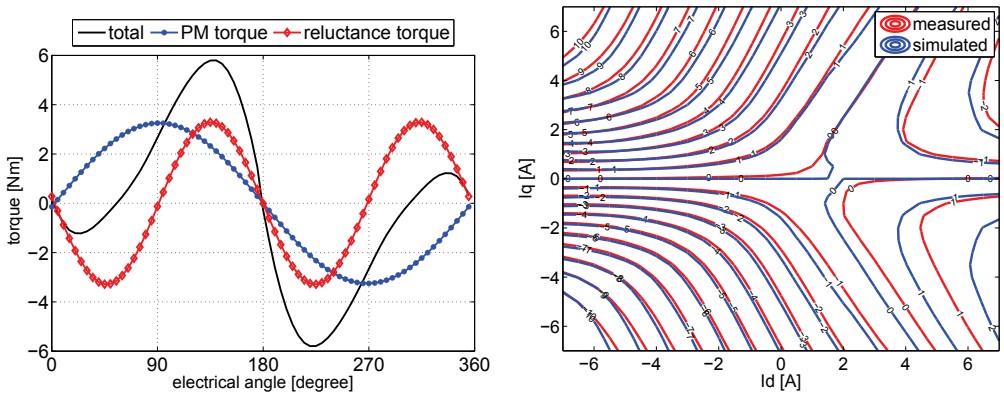

(a) measured torque vs current vector angle (b) constant torque loci

Figure 5.6: Steady state torque

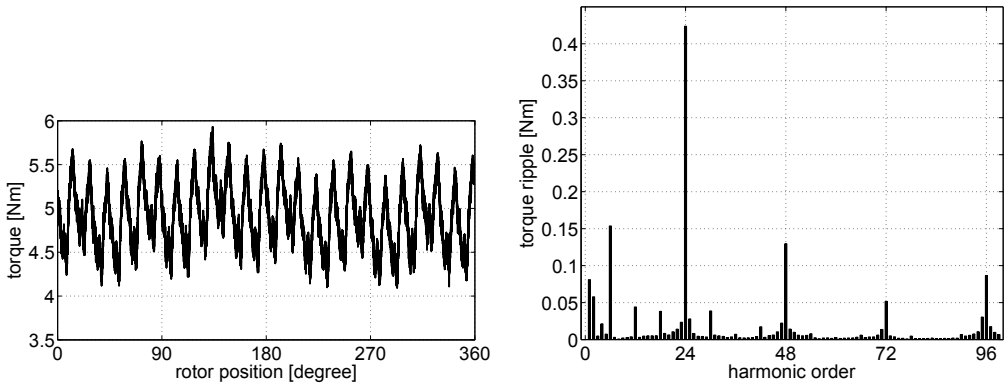

(a) Torque trend (b) Torque spectra

Figure 5.7: Torque as a function of rotor position: measurement

The whole torque mapping in the $I_d - I_q$ plane has been also measured. The torque has been sampled for each I_d and I_q current combination and averaged along a whole revolution of the rotor. Fig. 5.6(b) shows the constant torque loci achieved from both experimental tests and FE simulations. Also in this case, FE results match properly the experiments. The slight difference is due to the non-ideal magnetic properties of the lamination and to the deformation caused by die casting process.

Fig. 5.7 shows the trend of the torque as a function of the rotor position. The figure refers to the rated current corresponding to MTPA trajectory. The torque harmonic spectra is also reported in Fig. 5.7.

As a comparison, the simulated torque is reported in Fig. 5.8 as a function of the rotor position. The simulated torque harmonic spectra is reported in Fig. 5.8(b) Comparing Fig. 5.7(b) with Fig. 5.8(b) one can note that:

- The average torque from FE analysis is slightly higher than the measured one ($5.1Nm$ versus $4.9Nm$);
- The torque ripple from FE analysis is lower than the measured one (17% versus

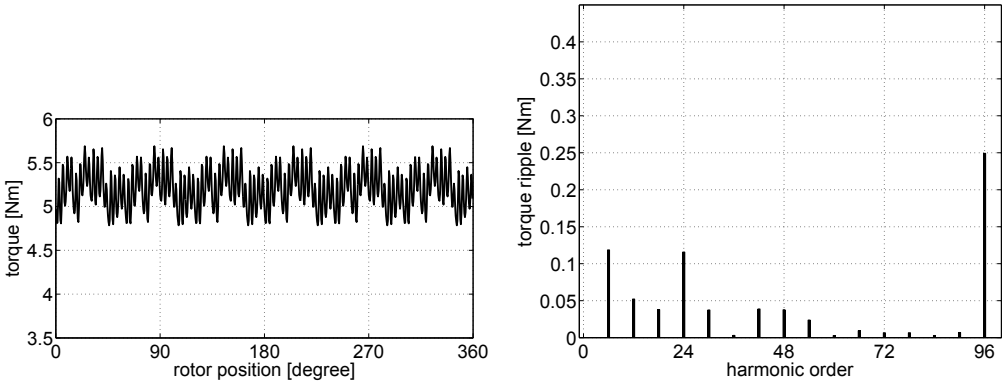

(a) Torque trend (b) Torque spectra

Figure 5.8: Torque as a function of rotor position: FE analysis

37%);

- The measured torque spectra contains harmonics whose order is lower than 6. These torque harmonics reveal that the torque periodicity is greater than 60 electrical degrees.
- The 24^{th}, 48^{th}, 72^{th} torque harmonics, are higher than the predictions. This is due to the rotor deformation caused by the die casting process. As a matter of fact, rotor assembly imperfections, rotor PM displacements and/or width and thickness variations correspond to increased harmonics whose orders are multiple of the number of teeth [88]. The discrepancy between the prediction and the measurements can be due also to manufacturing tolerances. In addition, local mechanical and and thermal stress close to the bridges during manufacturing may alter the magnetic properties. A different behavior is for the 96^{th} harmonic, whose amplitude results higher from the simulations.

Even though the rotor lamination was designed to reduce the torque ripple, the discrepancy between experimental and FE results shows that this is a critical aspect of the LS SyM manufacturing. It is true that the application for which the motor is designed does not require a particulary low torque ripple and the prototype does not exhibit any particular noise or vibration compared with the corresponding IM. However, the experimental analysis on the LS SyM prototype reveals that the rotor structure must be improved from the mechanical point of view if a low torque ripple is required.

Table 5.2: Efficiency measurement

	I [A]	V [V]	Pout [W]	Pin [W]	PF [-]	η [%]	$\Delta T\,[^{\circ}C]$
IM	3.53	399.3	1500	1838	0.75	81.6	47
LS SyM	3.04	397.8	1498	1706	0.81	87.8	37
LS SyM, FE	2.96	397.8	1498	1704	0.82	87.9	-

5.5.5. Efficiency measurements

The measurement of the prototype efficiency is carried out following the instructions of the European Standard for determining losses and efficiency [20]. The corresponding size of the confidence intervals within which the true mean value of efficiency are enclosed with a sufficiently high probability is determined. For the accurate description of the used instrumentation and the computation of the accuracy, see Appendix 5.6.1. The European standard suggests the direct measurement of input and output power for the determination of the efficiency of SyMs. This is a test method in which the mechanical power of a machine is determined by measurement of the shaft torque and speed. The electrical power of the stator is measured in the same test.

The efficiency of the IM with the same frame size of the LS SyM prototype is carried out for comparison. An IM classified within the IE2 efficiency class is used for this measurement. The European standard suggests for IM to determine the efficiency by the sum of separate loss components. However, the direct method is used also for the IM to allow a better comparison to be achieved.

The prototypes are mounted on the test bench and the torque-controlled IM is used to reproduce the load. They are supplied directly from the grid and after they reached the thermal steady state, the input and output power have been sampled. The stator winding temperature rise over the room temperature is acquired during the test. The results are reported in Table 5.2. It is worth noticing that the LS SyM exhibits an efficiency much higher than the IM (87.8% versus 81.6%). The stator currents of the prototype are lower, as well as the windings temperature. The PF results improved, from 0.75 for the IM to 0.81 for LS SyM. The LS SyM prototype performance, estimated with FE as illustrated in Section 4.2 and reported in Table 5.2, are in agreement with those from measurements.

It is worth to report that the manufacturing tolerances has not been minimized in the prototyping stage. A further increase of the LS SyM performance is expected if the manufacturing tolerances will be reduced.

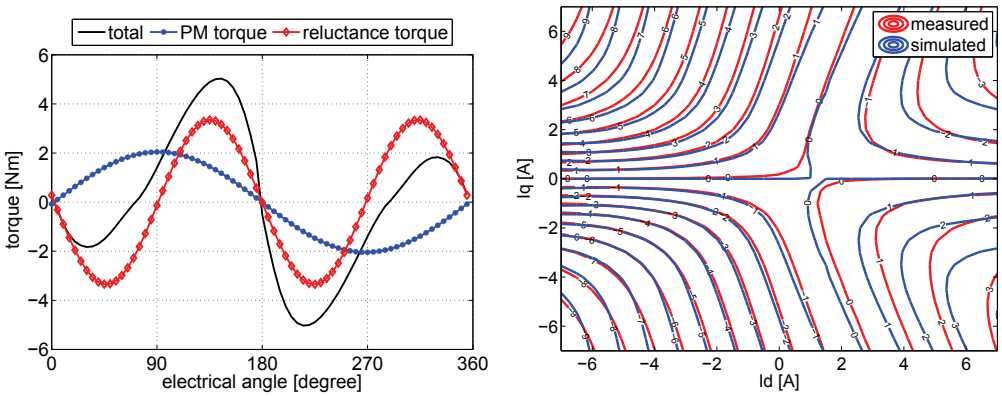

(a) measured torque vs current vector angle

(b) constant torque loci

Figure 5.9: Steady state torque: LS SyM with a reduced PM volume

Table 5.3: Efficiency measurement, low PM volume

	I [A]	V [V]	Pout [W]	Pin [W]	PF [-]	η [%]	ΔT [°C]
IM	3.53	399.3	1500	1838	0.75	81.6	47
LS SyM	3.41	400.6	1480	1733	0.73	85.4	47
LS SyM, FE	3.27	400.6	1480	1719	0.75	86.1	-

5.5.6. Measurements on a LS SyM with a reduced PM volume

The tests described previously have been repeated with a lower PM volume (about 70% of the original PM volume) introduced in the optimized rotor lamination of Section 5.4. Results are summarized in the following:

- the rms line-to-line back-emf is $104.0V$;
- the synchronization voltage, measured at: (i) full load and (ii) load inertia $J_{load} = 18.7J_m$ and (iii) thermal steady state, is $V_{syn} = 435V$;
- the torque versus current vector angle, at the same current level used in Subsection 5.5.4, is reported in Fig. 5.9(a). The measured and simulated constant torque loci is shown in Fig. 5.9(b).
- The steady state performance is reported in Table 5.3 for both measurements and FE analysis. The IM performance is also reported in Table 5.3 for comparison.

From the results of the tests on the LS SyM with a lower PM volume, it is worth noticing that:

1. The reluctance torque component is 1.6 times the PM torque component;
2. The measured efficiency and PF are lower with respect to full PM volume motor; However, the efficiency is still much higher compared with the IM one.

3. The synchronization capability is reduced with respect to full PM volume motor. This result shows that the reduction of the synchronizing energy due to a lower PM flux has a predominant effect on the synchronization capability with respect the reduction of the PM breaking torque. this is expected because the PM breaking torque is a function of the square of the PM flux (see (2.14)), which is relatively low in the considered prototype.
   The tested load inertia is very high compared with an actual $1.5kW$ impeller. Unfortunately, a lower inertia test bench was not available in the laboratory. Alternatively, if the load torque is controlled with high bandwidth, the load inertia could be actively emulated to determine the pull-in characteristic of the machine under test [87]. The simulations reveals that, with a load inertia halved with respect the tested one, the synchronization capability is about $360V$, which is enough for the considered application.

5.6. Conclusions

This Chapter describes a new approach for the design of a LS SyM. The analysis is applied on a small size, 2-pole, three-phase LS SyM as this category is still not found in the motor market and it exhibits the highest potential in efficiency improvements. The design procedure takes into account the constrains due to the manufacturing process (with particular reference to the die casting process). From the manufacturing point of view, the possibility to apply the recent improvements to the design of SRM, with or without PM assistance, on LS SyM is discussed.

A stochastic optimization has been used to design the rotor lamination. After the automatic drawing of the rotor is developed, FE analysis is used to evaluate the optimization objectives considering the machine nonlinearities. Both steady state and dynamic performance are considered. Experimental measurements are carried out on a LS SyM prototype resulting from the optimization and the results are compared with the predictions. All the results from the experiments are in agreement with those from FE simulations.

The following experiments are illustrated in the text:

- Back-emf measurement;
- Determination of the magnetic characteristics;
- Synchronization tests;
- Synchronous torque measurements;
- Efficiency measurement.

Different PM volumes are tested in the same rotor structure, evaluating their impact on the dynamic and steady state performance of the motor. The performance of the LS SyM counterpart, the IM, is also measured providing an overview comparison between the IM and LS SyM performance. The LS SyM prototypes exhibit superior steady state performance with respect that of the corresponding IM. A very good synchronization capability is achieved also when a reduced PM volume is considered. It is demonstrated

that the LS SyM technology is a good solution to meet the new efficiency classes in the large-scale production with a low PM volume buried in the rotor.

5.6.1. Appendix A

This Appendix is dedicated to the description of the instrumentations used to determine the efficiency of the prototype and to the analysis of the uncertainty of this test.

European Standard for determining losses and efficiency [20] suggests to use 0.2 class instrumentation. The following 0.2 class instrumentations have been used in this thesis:

- Watt-meter WT230: The absolute value of the uncertainty is $E_w = 0.1\%P_{meas} + 0.1\%Range$. Assuming a measured value of $1500W$, it results $E_w = 0.1\%(1500) + 0.1\%(3000) = 4.5W$
- Torque-meter, whose rated torque is $20Nm$: From the data-sheet it results an absolute value of the uncertainty $E_{t20} = 0.1\%(20) = 0.02Nm$. In addition, it exhibits an offset variable between $-0.085 \div -0.038Nm$. The offset can be written as $Of_{t20} = -0.0615 \pm (0.085 - 0.0380)/2 = -0.0615 \pm 0.0235Nm$. The instrument magtrol 3411 is used for the automatic acquisition of output torque and speed.

A sinusoidal power supply was not available to supply the LS SyM under test. The efficiency test was carried out supplying the motor directly from the grid. The harmonic voltage factor of the grid voltage resulted $HVF = 0.018$, lower than suggested from the standard.

The uncertainty is computed using the laws of the statistical error propagation. It is assumed that the effects which cause a deviation of the measurements from the actual value are of random nature. Therefore, the measured quantities will obey in good approximation the so-called normal or Gaussian distribution. It can be affirmed that there is a 95% probability that any value of the quantity x lies into the interval $x_{mean} \pm 1.96\sigma_x$, where x_{mean} and σ_x are the actual mean value and the actual standard deviation (unknown).

In the case of the efficiency measurement, the input and output power are subjected to inevitable fluctuations even at constant conditions (random uncertainty). Only N readings of the measured quantities are available (e.g. input power) and the actual mean value and the actual standard deviation can not be determined. In these cases, only a confidence interval of x can be determined to which the true (mean) value x_{mean} is confined with a certain probability. For this aim, the arithmetically averaged value $\hat{x}$ of the N x-values is taken as an estimate of the true (mean) value. To compute the confidence interval, it can be written that, for a 95% of probability,

$$\hat{x} - \frac{1.96 s_x}{\sqrt{N}} \leq x_{mean} \leq \hat{x} + \frac{1.96 s_x}{\sqrt{N}} \tag{5.3}$$

where s_x is the standard deviation of the N readings with respect to their average value $\hat{x}$, computed as

$$s_x = \sqrt{\frac{1}{N-1} \Sigma_{i=1}^{N} (x_i - \hat{x})^2} \tag{5.4}$$

As suggested by the standard, a high number of samples (> 200) of input and output power are acquired. The relative overall measurement uncertainty is calculated by the square root of the sum of the squares of the random uncertainty and the instrument uncertainty. However, the confidence interval of the input and output power is relatively small compared to the instrumentation uncertainty due to the high number of samples. For this reason, the random uncertainty will be neglected.

As far as the statistic uncertainty of the instrumentation, a uniform distribution of the samples within the uncertainty interval is usually assumed by the manufacturers. In this case, it is expected that the measurement lies within the interval

$$x_{meas} \pm \sigma_{meas} = x_{meas} \pm \frac{E_{meas}}{\sqrt{(3)}} \tag{5.5}$$

where σ_{meas} represents the standard deviation of the measurement and E_{meas} is the instrument absolute value of the uncertainty.

The relative uncertainty of the speed (measured with the magtrol 3411) is $\epsilon_{speed} = 0.01\%$ of reading), which is negligible with respect to the output torque and input power uncertainty.

Assuming a uniform distribution of the torque offset within the interval $-0.085 \div -0.038Nm$, the output torque uncertainty is computed as

$$E_{t20} = \sqrt{\frac{0.02^2}{3} + \frac{0.0235^2}{3}} = 0.0178Nm \tag{5.6}$$

Considering a mean value of the N torque readings of $4.8Nm$, the statistical percentage uncertainty is

$$\epsilon_{t20} = 0.0178/4.8 * 100 = 0.37\% \tag{5.7}$$

The watt-meter percentage uncertainty, considering an average value of $P_{meas} = 1500W$, is $\epsilon_w = \frac{4.5}{1500*\sqrt{(3)}} * 100 = 0.17\%$;

The total percentage efficiency uncertainty is therefore

$$\epsilon_\eta = \sqrt{\epsilon_{t20}^2 + \epsilon_w^2} = \sqrt{0.37^2 + 0.17^2} = 0.4\% \tag{5.8}$$

The absolute efficiency uncertainty, considering an average value of $\eta = 87.8\%$, is

$$E_\eta = \epsilon_\eta * \eta = 0.004 * 87.8 = 0.4\% \tag{5.9}$$

The efficiency can therefore be written as $\eta = (87.8 \pm 0.4)\%$.

Chapter 6

Geometry of Line Start Synchronous Motors Suitable for Various pole Combinations

The difficult design, manufacture and the high cost due to presence of PM limit the widespread of LS SyM in the market. Another key factor that limits the LS SyM diffusion is the need of having a wide variety of different laminations of different size, increasing the number of pieces to be stored, the number of mould geometries etc. This Chapter presents an innovative LS SyM design that allows the same stator and rotor laminations to be used for different number of poles. From the manufacturing point of view, the adoption of a unique rotor lamination is extremely advantageous. It is shown that satisfactory performance can be achieved only rearranging the stator winding according to the number of poles. Experimental measurements are carried out on a LS SyM prototype in which the same lamination is used for a 2-pole and 4-pole machine.

6.1. Introduction

A key factor that limits the LSSM diffusion in the market is that an industry should add to the production a wide variety of motors of different size and different lamination, increasing the number of laminations to be stored, the number of mould geometries etc. As suggested in [29], the same lamination can be used for motors of different size but for each speed (number of poles) a new lamination design is needed. In IMs the number of rotor poles is adapted to stator poles. On the contrary, in LS SyM, the rotor polarity depends on the rotor geometry and the magnetization direction of PMs. Dahlander type winding can not be used.

This Chapter describes an innovative design for three-phase LS SyMs. The aim is to use the same lamination for motors of different number of poles so as to reduce the manufacturing cost (stamps, stored parts etc), even though the motor performance may slightly decrease. When the number of poles is fixed, each motor configuration requires particular design peculiarity (flux barrier angle, back iron and tooth size etc). This Chapter shows that satisfactory performance can be achieved using the same LS

SyM lamination for motors with a different number of poles. The stator windings are adapted for each number of poles so as to work properly at the desired synchronous speed.

Three motor geometries are analyzed by means of the design techniques described in Chapters 3 and 4, highlighting their advantages and drawbacks. The first motor geometry (**mcA**) is suitable for 2-, 4- and 6-pole motors, respectively. The second (**mcB**) and the third (**mcC**) motor geometries are suitable for 2- and 4-pole motors, respectively.

The final part describes the experimental tests on a LS SyM prototype, whose lamination is similar to the **mcC** one. The measured performance is reported for both 2- and 4-pole, showing a good agreement with the simulated performance.

6.2. Multi-pole rotor structure

In order to employ the same rotor lamination in motors running at different speeds, it is necessary that it can be used with different number of poles. Therefore, a tradeoff between various aspects has to be done. As an example, the stator back iron of a 4-pole machine generally is not suitable for a 2-pole machine. On the other hand, the stator back iron of a 2-pole machine is oversized for a 4-pole machine. Thus, the 4-pole stator IM can be rearranged to achieve reasonable flux density in the stator back iron of a 2-pole LS SyM.

The location of the flux barriers with PMs affects significantly the motor performance, in terms of average torque, efficiency and torque ripple. The optimal flux barrier angle is a function of the number of poles [89]. Thus, it is necessary to find a rotor structure that can give satisfactorily performance for all the desired number of poles.

As illustrated in Chapters 3 and 4, the choice of the number of conductors per slot n_{cs} affects the steady state and the starting performance, since the rotor parameters vary with the square of n_{cs}. In this Chapter, n_{cs} is chosen to maximize the efficiency. The synchronization capability has been considered in the analysis: the analytical model combined with FE simulations described in Chapter 3 is used to compute the minimum synchronization voltage of LS SyMs. The rotor cage of all the LS SyMs shown in this Chapter is designed to synchronize a load inertia at least 5 times the motor inertia, at full load and rated voltage, for any number of poles. The slot fill factor is fixed at 0.4 for all the motors.

6.2.1. mcA: motor geometry suitable for 2, 4 and 6 poles

Fig. 6.1 illustrates the lamination of the **mcA**, whose geometrical data are reported in Table 6.1. It is a lamination suitable to be used in 2-, 4- and 6-pole LSSM, respectively, by changing i) the magnetization direction of the PMs in the rotor and ii) the stator winding. The slots occupied by a phase of the stator winding are highlighted in Fig. 6.1 according to the different number of poles. A non-chorded winding is considered in all cases. The stator lamination is a standard lamination for a 4-pole IM. The rotor exhibits symmetry over 60 mechanical degrees and there are 30 rotor slots.

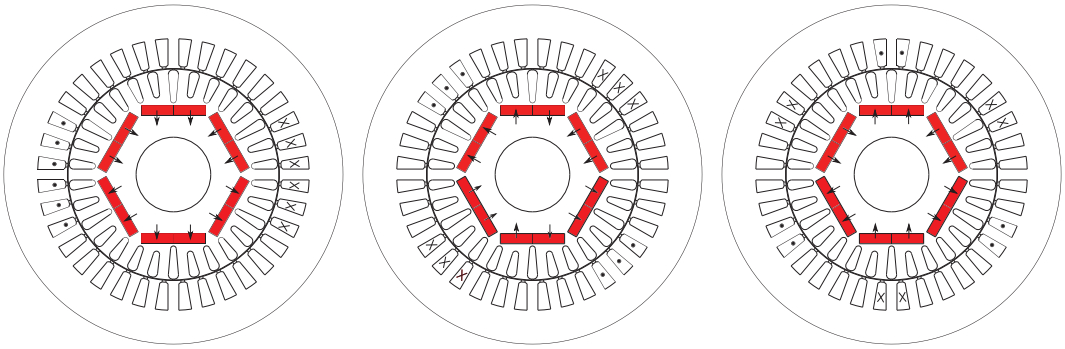

(a) 2-pole configuration (b) 4-pole configuration (c) 6-pole configuration

Figure 6.1: Lamination of **mcA** motor: for 2, 4 and 6 poles, according to the PM magnetization direction and winding type

Table 6.1: Geometrical data of **mcA** lamination

symbol	description	value	unit
D_e	external diameter	200	mm
D_s	airgap diameter	125	mm
L_{stk}	stack lenght	110	mm
g	airgap	0.4	mm
Q_r	n. of stator slot	30	-
Q_s	n. of rotor slot	36	-

The considered PMs are high energy NdFeB. They are oriented so as to form 1, 2 and 3 pole pairs, respectively. The machines with such different number of poles have been analyzed by means of FE analysis. Fig. 6.2 illustrates flux lines and the flux density at no load (only PM flux). In the 2-pole motor, three PMs are oriented with "North" direction and other three PMs with "South" direction. As illustrated in Fig. 6.2(a), the 2-pole machine exhibits a high flux density in the back iron ($1.8T$) and the associated iron losses will be relatively high. As reference, the flux density in the tooth and in the back iron at no load in the corresponding IM is $1.6T$ and $1.5T$, respectively. In the 4-pole machine, 3 barriers over 6 contain PM with different

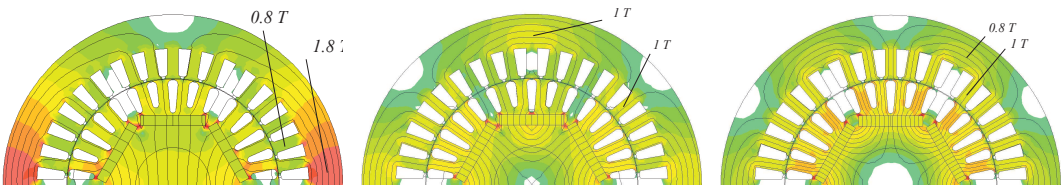

(a) 2-pole configuration (b) 4-pole configuration (c) 6-pole configuration

Figure 6.2: No load flux lines and flux density map of **mcA** lamination according to PM magnetization direction, Fig. 6.1

Table 6.2: Performance of **mcA** motor

Parameter	2-pole LSSM	4-pole LSSM	6-pole LSSM
P_j [W]	319	262	363
P_{iron} [W]	157	92	61
P_{out} [W]	5500	4000	4000
PF [-]	0.98	0.92	0.98
speed [rpm]	3000	1500	1000
η [%]	91.4	91.6	89.7
η IE4 [%]	90.9	91.1	89.5
V_{syn} [V]	330	330	360

magnetization direction. In order to avoid PM flux to be short-circuited between any other pole, the rotor bar at the center of the PM is deeper with respect the other bars, as in Fig. 6.1. In the 6-pole motor, each flux barrier addresses PMs with alternating magnetization direction.

The performance of **mcA** motor is reported in Table 6.2 as a function of the number of poles. The highest power at which the IE4 efficiency is reached is referred to as rated power. When the same lamination is used for motor with different number of poles, attention should be paid to select properly the "rated" working conditions [78]. As shown in Table 6.2, the 2-pole motor configuration (5.5 kW vs 4 kW for the 4- and 6-pole motor, respectively) exhibits higher losses. Consequently, the 2-pole motor exhibits a higher temperature. However, LS SyM motor exhibits higher power density than the corresponding IM and it could be reasonable to increase the rated power of the LS SyM. The measured temperature at steady state of the prototypes are reported for reference in Section 6.3.

The loss components (Joule losses P_j and iron losses P_{iron}) are highlighted in Table 6.2. They are estimated as in Chapter 4: the Joule losses are computed with the stator resistance computed at $100°C$ and the iron losses are estimated by means of the teeth and back iron maximum flux density (computed with FE).

It is worth noticing the losses distribution as a function of the number of poles. Regarding the Joule losses P_j, they are higher than P_{iron} in all cases. As far as the iron losses are concerned, they are higher in the 2-pole machine as expected, due to the high flux density in the back iron.

McA geometry allows the IE4 efficiency class to be reached for all the considered number of poles, a result which is difficult to be achieved using IM.
The minimum synchronization voltage is also reported in Table 6.2. All configurations are well suited to start-up the motor at the rated voltage

6.2.2. mcB: motor geometry suitable for 2 and 4 poles

Table 6.3: Geometrical data of **mcB** lamination

symbol	description	value	unit
D_e	external diameter	210	mm
D_s	airgap diameter	125	mm
L_{stk}	stack lenght	110	mm
g	airgap	0.4	mm
Q_r	n. of stator slot	28	-
Q_s	n. of rotor slot	36	-

The **mcB** geometry is suitable to be used in 2- and 4-pole machines. Its lamination is shown in Fig. 6.3 and its geometrical data are reported in Table 6.3. The size of

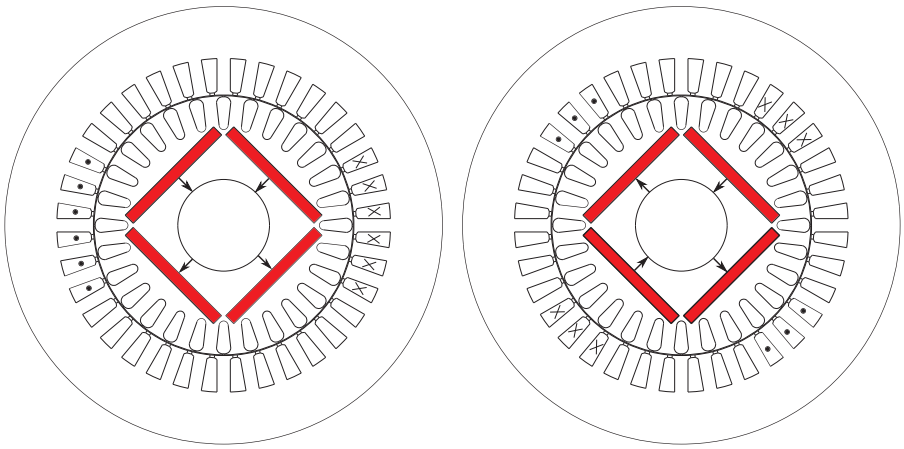

(a) 2-pole configuration (b) 4-pole configuration

Figure 6.3: Lamination of **mcB** motor: for 2 and 4 poles, according to the PM magnetization direction and winding type

mcB lamination is similar to the size of **mcA** lamination, with the exception that the external diameter has been slightly increased (from 200 mm to 210 mm). Due to the higher PM flux of this rotor structure, the stator back iron flux density in the 2-pole machine would be higher than $1.8T$. The **mcB** PM volume is the same of the **mcA** one.

Fig. 6.4 shows the distribution of flux lines and the correspondent flux density at no load for the 2- and 4-pole machines. It can be noted that the stator back iron flux density is $1.6T$ in the 2-pole machine. As expected, in the 4-pole machine the stator back iron flux density is $0.8T$ that is, halved with respect the 2-pole machine one. The performance of the **mcB** motor is shown in Table 6.4 as a function of the number of poles, together with the loss components.

The **mcB** rotor structure allows a high performance to be achieved both in 2- and 4-pole machines. When running as 2-pole machine, the **mcB** motor exhibits higher

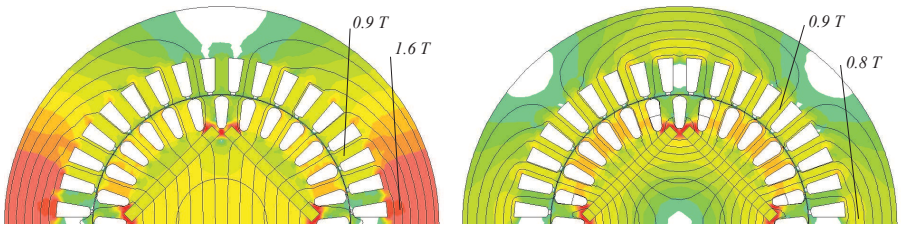

(a) 2-pole configuration (b) 4-pole configuration

Figure 6.4: No load flux lines and flux density of **mcB** lamination according to PM magnetization direction, Fig. 6.3

Table 6.4: Performance of **mcB** motor

Parameter	2-pole LSSM	4-pole LSSM
P_j $[W]$	448	297
P_{iron} $[W]$	172	103
P_{out} $[W]$	7500	5500
PF [-]	0.95	0.93
speed [rpm]	3000	1500
η [%]	92.1	92.6
η IE4 [%]	91.7	91.9
V_{syn} [V]	320	380

losses due to the higher rated power. The Joule losses increase is due to the longer end windings and a slightly higher stator current. The iron losses increase is due to the higher stator flux density. Attention should be paid to the synchronization in the case of 4-pole, since the high PM flux linkage causes a high breaking torque during start up. This is the cause of the relatively high synchronization voltage of the 4-pole motor, see Table 6.4. Anyway, it remains lower than the rated one.

6.2.3. mcC: motor geometry suitable for 2 and 4 poles with induced pole

The **mcC** geometrical data of are shown in Table 6.5. Its lamination is shown in Fig. 6.5. It is substantially different from the **mcB** one, which was shown in Subsection6.2.2: there are only two rotor flux barriers in the rotor.

In the case of 4-pole, the PMs are arranged so as to obtain an induced pole rotor structure [90]. Thus, two poles located in alternate positions require PMs and the other two do not. These induced poles are achieved by the flux re-distribution. On one hand, good performance of the 4-pole machine are achieved when the flux barrier angle is at about 45 degrees with respect the PM magnetization axis. On the other hand, to achieve good performance in the 2-pole machine, the flux barrier angle must be increased with respect the PM magnetization axis. The selected flux barrier angle is a compromise to achieve satisfactory performance both in the 2- and 4-pole machine.

Table 6.5: Geometrical data of **mcC** lamination

symbol	description	value	unit
D_s	airgap diameter	140	mm
g	airgap	0.4	mm
D_e	external diameter	220	mm
L_{stk}	stack lenght	120	mm
Q_r	n. of stator slot	28	-
Q_s	n. of rotor slot	36	-

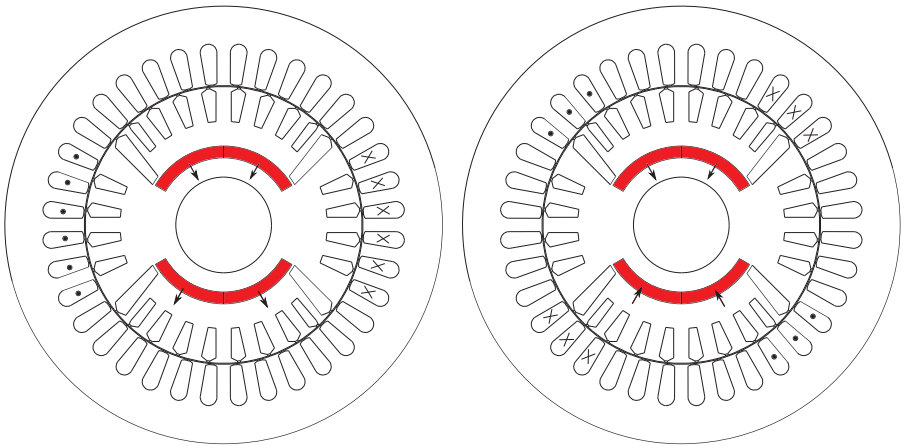

(a) 2-pole configuration (b) 4-pole configuration

Figure 6.5: Lamination of **mcC** motor: for 2 and 4 poles according to the PM magnetization direction and winding type

McC motor has the advantage that it contains a lower PM volume (about 35%) with respect **mcA** and **mcB** motors. Fig. 6.6 shows the flux lines distribution and the correspondent flux density at no load for **mcC** motor. Its performance is reported in Table 6.6.

Similarly to **mcB** motor, the estimated efficiency exceeds the IE4 efficiency class limit both in the 2- and 4-pole machine. This is an interesting result, considering the lower PM volume of the induced pole rotor structure. However, it should be mentioned that the overall volume of the **mcC** motor is 32% higher than the **mcA** one and 20% higher than the **mcB** one (higher outer diameter).

It is worth noticing that the 4-pole machine exhibits higher iron losses, even if the no-load flux density in the stator parts are rather low. This is due to the stator flux density that increases considerably when the machine is loaded.

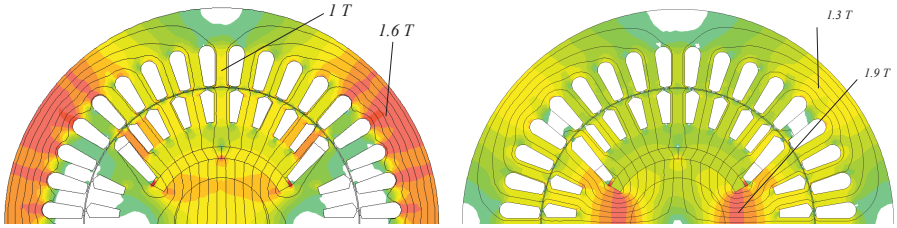

(a) 2-pole configuration (b) 4-pole configuration

Figure 6.6: No load flux lines and flux density of **mcC** lamination according to PM magnetization direction, Fig. 6.5

Table 6.6: Performance of **mcC** motor

Parameter	2-pole LSSM	4-pole LSSM
P_j $[W]$	401	252
P_{iron} $[W]$	198	170
P_{out} $[W]$	7500	5500
PF [-]	0.87	0.80
speed [rpm]	3000	1500
η [%]	92.2	92.4
η IE4 [%]	91.7	91.9
V_{syn} [V]	325	300

6.3. Experimental measurements on the prototypes

Experimental measurements are carried out on the LS SyM prototype resulting from the optimization described in Chapter 5. Its lamination is of the **mcC** type, as in Fig. 6.5. It has been optimized to run as 2-pole motor and lower performance is expected when it works as 4-pole motor with induced pole. The measurements carried out in this Section allows the analysis presented in this Chapter to be validated.

The prototype is mounted on a test bench in which a torque-controlled master IM is used to reproduce the effect of the load. The motor under test has been connected to the master motor through a torque transducer and supplied by the grid.

After the synchronization, the load has been applied by means of the master motor. The efficiency is measured with the direct-method at thermal steady state (that is, after about 3 hours of operation). The measured motor performance is reported in Table 6.7 together with the results of the simulations for the 2- and 4-pole machine, respectively. The stator winding overtemperature with respect the room temperature is also reported. As a term of comparison, the corresponding 2-pole IM stator winding overtemperature is $\Delta T = 47°C$, see Table 5.2.

The simulations predict with good accuracy the performance in both cases, validating the proposed approach. It is interesting to report that both the 2- and 4-pole motors are able to synchronize the nominal load with an inertia of 18.7 times the motor

Table 6.7: LSSM prototype: Performance

	Parameter	FE results	Measurements	unit
2-pole	P_{out}	1498	1498	W
	PF	0.82	0.81	-
	speed	3000	3000	rpm
	η	87.9	87.8	%
	ΔT	-	63	$^{\circ}C$
4-pole	P_{out}	533	533	W
	PF	0.54	0.53	-
	speed	1500	1500	rpm
	η	72.9	72.6	%
	ΔT	-	83	$^{\circ}C$

one at the rated voltage. The 2-pole motor exhibits a high efficiency, which exceeds the IE4 class one. Table 6.7 confirms that the 4-pole motor exhibits a low efficiency as well as a low power density.

6.4. Conclusions

Different design configurations of Line Start Synchronous Motor are proposed to the aim of using the same lamination for various pole combinations. The advantages of such a solution are:

i) the possibility to reduce the number of different parts that must be produced and stored and

ii) the possibility to use the same mould to produce motor of different number of poles.

The design results to be a tradeoff between contrasting aspects, because each number of poles requires particular design peculiarities such as flux barrier angle, back iron and tooth size etc. The different design configurations are analyzed by means of FE. Advantages and drawbacks of the proposed rotor structures are discussed. It is shown that, with proper design criteria, satisfactory performance can be achieved for all the considered number of poles as summarized in Fig. 6.7.

Experimental measurements are carried out on a Line Start Synchronous Motor prototype, where the same lamination is used to run 2- and 4-pole machine, respectively. The measured performance results in good agreement with the prediction, confirming the validity of the proposed analysis.

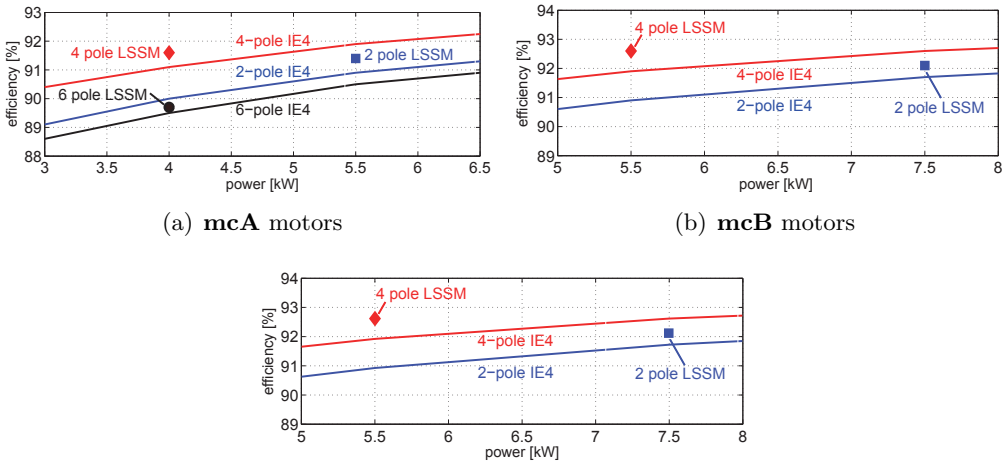

(a) **mcA** motors

(b) **mcB** motors

(c) **mcC** motors

Figure 6.7: Efficiency of the proposed machine configurations as a function of the power and the number of poles

Chapter 7

Modeling and analysis of Line Start Synchronous Machines containing space harmonics

This Chapter presents an analytical model that describes the mutual interaction between coupled electrical circuits in machines with complex rotor structure such as LS SyM. After defining the main assumptions of the analytical model, the procedure to compute the self- and mutual-inductances of each circuit in terms of winding space harmonic is derived. The literature reveals that this topic has been discussed extensively for IM. As regards LS SyM, there is a lack of theoretical studies regarding harmonic phenomena due to the complex machine structure. This part of the thesis aims to fill this gap. Such a model is useful to analyze the parasitic torques in the LS SyM and IM torque characteristic, being the IM a particular subset of LS SyM. The analytical model is also useful in general whether it is of interest to determine the winding inductances of a machine with saliency considering the harmonic content.

7.1. Introduction

The analysis carried out in Chapters 2 and 3 consider sinusoidally distributed stator and rotor windings, neglecting any MMF harmonic phenomena. However, synchronous and asynchronous torque dips in torque versus speed curve of a cage IM may be large depending on the number of stator and rotor slots [26]. These parasitic torques can prevent the successful operation of the motor. Analytical methods are used to predict the amplitude and the frequencies associated with the parasitic torques of IM. FE analysis is used by several authors to study the parasitic torques of IM considering saturation, skin effect in rotor bars, three-dimensional effects and so on [91]. Although FE analysis is preferred in the final design stage, analytical models are still appreciated for their speed and for the understanding of the involved phenomena.

Unlike the IM, the LS SyM rotor is usually unskewed because of the PM buried in the rotor core. A rich airgap MMF harmonic content can arise and parasitic torques in the torque-speed characteristic can affect the synchronization process. The MMF harmonic

effect on the LS SyM torque characteristic has been studied in [51, 57]. However, a general criteria to design LS SyM so as to avoid parasitic torques is still to be developed.

The goal of this Chapter is to develop a general approach to describe harmonic phenomena in LS SyM. The coupled-circuit approach is used to derive an analytical model of a LS SyM in which all MMF harmonics are taken into account. The key concept is to describe the inductance coefficients of any machine winding in terms of harmonic winding turn. The mathematical formulation of an electrical machine containing space harmonic using the coupled circuit approach and the derivation of the circuit parameters can be found for example in [92–94]. A study on the mutual inductance between LS SyM windings is presented in [95]. However, the mutual coupling between different rotor parts was neglected. Hereafter, a more general approach is derived. The analysis is applied on a machine which is not doubly-cylindrical (IM) or with salient pole (generator), but which contains flux barriers in the rotor, as a SRM. The model is applicable to both squirrel cage IM and LS SyM, as the IM can be considered as a particular subset of LS SyM without saliency in the rotor.

The first part of this chapter describes the model hypothesis. The machine equations are briefly described. Then, the inductance coefficients are computed considering each coil to be excited separately. The drawback of this approach is that it leads to a high number of differential equations to be solved numerically.

FE analysis is used to validate the results. In particular, the winding inductance coefficients has been computed by FE analysis as a function of the rotor position, showing a very good agreement with those from analytical computations.

7.2. Hypothesis of the model

The coupled magnetic circuit theory is used for the derivation. The following general assumptions are made:

- negligible iron saturation;
- absence of stator/rotor skewing;
- the magnetic circuit of the considered LS SyM is constituted by i) a smooth stator (without saliency), neglecting the slotting effect and by ii) a slottless squirrel cage (with negligible interbar current) on a rotor with saliency given by 1 flux barrier, whose position with respect the rotor $d-$axis is shown in Fig. 7.1. The flux barrier angle θ_{b1} of Fig. 7.1 indicates the half angle of the flux barrier, expressed in mechanical degrees;
- no PM are inside the flux barriers or elsewhere;
- in the stator there are three identical stator windings, mutually displaced by 120 electrical degree. Each stator winding is constituted by N turns each, distributed in $2q$ stator slots, where q is the number of slot per pole per phase. It is assumed that q is an integer. Fractional slot windings are not considered here because they exhibit a richer harmonic content than those having an integral number of slots per pole per phase and they are not commonly used for IM and LS SyM. It is

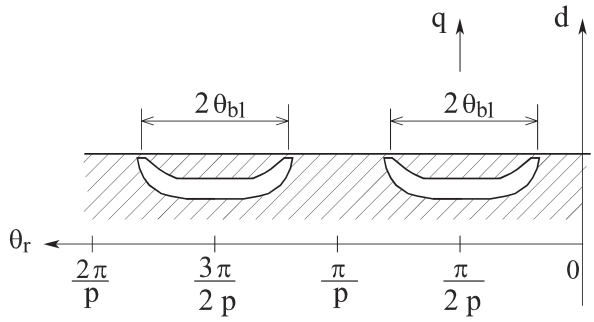

Figure 7.1: Geometrical references of the flux barriers

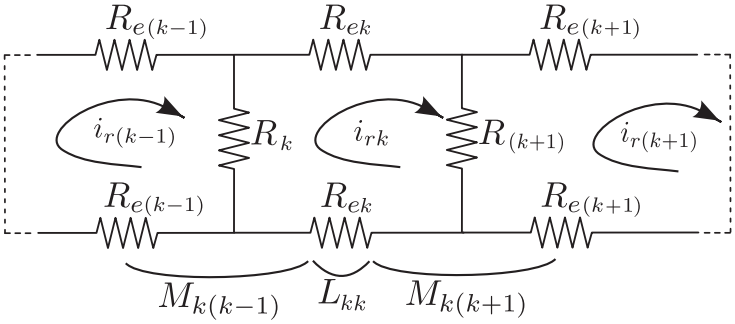

Figure 7.2: Rotor cage equivalent circuit

also assumed that the electrical angle corresponding to two conductors carrying equal currents of opposite signs is π (full pitch), that is, shortened or lengthened pitch are not considered.

- the leakage inductances of the stator windings, rotor bars and end rings are neglected.

The aforementioned assumptions may seem rather severe to the reader but they permit an easier model description. In a second time, the model presented in this Chapter can easily be generalized to include the effect of PM buried in the rotor, the effect of slotting, shortened or lengthened pitch of the stator windings and the presence of leakage inductances. Iron saturation is more severe to be treated analytically, but it is beyond the scope of this analytical model. Saturation is described with accuracy by FE analysis, that is a forced step in the final machine design.

A common assumption in the analysis of machines with squirrel cage rotor is that the cage can be replaced by a polyphase winding having the same number of poles of the stator winding. This assumption is justified by referring to steady state operation with sinusoidal rotor current. In [96], the rotor conductors are combined in pairs to form symmetrical circuits along the d– and q–axis. In this work a more general approach is necessary and the cage rotor is considered as a set of mutually coupled loops. Each loop is defined by two adjacent rotor bars and the connecting portions of the end rings between them. The equivalent circuit of the rotor cage is shown in Fig. 7.2. One can note that all the end winding (R_{ek}) and the rotor bar (R_k) segments are different between each other. The self- (L_{kk}) and the mutual-inductance ($M_{k(k+1)}$) of the first

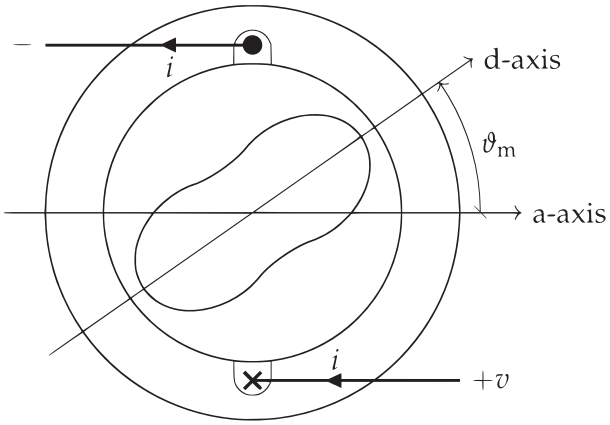

Figure 7.3: Sketch of an elementary electromechanical energy converter

rotor loop are sketched in Fig. 7.2. With the same notation and obvious meaning of the terms, the self- and mutual-inductances between the stator phases and between the stator phases and the rotor loops are defined.

One advantage of this approach is that it is also applicable to cage rotors with non-integral number of rotor bars per stator pole-pair. No assumption has been made on the cage bars distribution. Rotor bars are not assumed uniformly distributed, as in [35, 97] for the IM, nor in correspondence of the pole shoe of a salient pole machine. The position of the rotor bars along the rotor circumference is a variable of the model. The modification of the stator field due to rotor currents is taken into account adopting the coupled magnetic circuit theory. The model is valid for any type of excitation and during transient operation since no assumption has been made regarding the current waveform.

7.3. Machine equations

Consider the elementary rotary electro-mechanical converter of Fig. 7.3. For a conservative system with the user convention, the following voltage balance equation can be written:

$$v(t) = Ri(t) + \frac{d\lambda(t)}{dt} = Ri(t) + \frac{dL(\theta_m^e)}{dt} i(t) + L(\theta_m^e)\frac{di(t)}{dt} \tag{7.1}$$

where the flux linkage to the coil is $\lambda = L(\theta_m^e)i(t)$, having indicated with R and $L(\theta_m^e)$ the resistance and the inductance coefficient of the coil, respectively. If L is function of the rotor position (for example when the rotor exhibits saliency), the voltage differential equation is of the second order with non-constant coefficients and the analytical solution does not exist.

Consider now a three-phase machine with a non-salient stator and a salient rotor with cage. A common choice in electrical machine analytical analysis is to consider only the constant and the first harmonic term in the stator winding inductance coefficients. Under this hypothesis, the $d-q$ transformation changes the time-varying stator

differential equations into constant coefficient differential equations, for which the analytical solution exists. The other inductance harmonic terms remain time-varying after transformation (see Appendix 7.6) and they are difficult to handle mathematically [97]. This is the reason why they are commonly ignored. For this reason, no transformations are applied to the circuit equations of this analysis.

In general, for a machine having n rotor bars, there are $n+3$ nonlinear differential equations (plus the mechanical equation). The voltage equations of the considered LS SyM are, in matrix form:

$$[v] = [R]\,[i] + \frac{d}{dt}\,[\lambda] \quad = [R]\,[i] + [i]\,\frac{d}{dt}\,[L] + [L]\,\frac{d}{dt}\,[i] \tag{7.2}$$

Splitting the resistance and inductance matrices into stator and rotor submatrices, they become

$$[R] = \begin{bmatrix} [R_s] & [0] \\ [0]^T & [R_r] \end{bmatrix} \tag{7.3}$$

and

$$[L] = \begin{bmatrix} [L_s] & [M_{sr}] \\ [M_{rs}]^T & [L_{loops}] \end{bmatrix} \tag{7.4}$$

Developing each submatrix, one obtains

$$[R_s]_{3x3} = \begin{bmatrix} R_s & 0 & 0 \\ 0 & R_s & 0 \\ 0 & 0 & R_s \end{bmatrix} \tag{7.5}$$

$$[R_r]_{nxn} = \begin{bmatrix} R_1 + R_2 + 2R_{e1} & -R_2 & ... & 0 & 0 & -R_1 \\ ... & ... & ... & ... & ... & ... \\ ... & -R_k & R_k + R_{k+1} + 2R_{ek} & -R_{k+1} & 0 & ... \\ ... & ... & ... & ... & ... & ... \\ -R_1 & 0 & 0 & ... & -R_n & R_n + R_1 + 2R_{en} \end{bmatrix} \tag{7.6}$$

$$[L_s]_{3x3} = \begin{bmatrix} L_{aa} & M_{ab} & M_{ac} \\ M_{ba} & L_{bb} & M_{bc} \\ M_{ca} & M_{cb} & M_{cc} \end{bmatrix} \tag{7.7}$$

$$[L_{loops}]_{nxn} = \begin{bmatrix} L_{11} & M_{12} & ... & ... & M_{1n} \\ ... & ... & ... & ... & ... \\ M_{k1} & ... & L_{kk} & ... & M_{kn} \\ ... & ... & ... & ... & ... \\ M_{n1} & ... & ... & M_{n(n-1)} & L_{nn} \end{bmatrix} \tag{7.8}$$

$$[M_{sr}]_{3xn} = \begin{bmatrix} M_{a1} & M_{a2} & ... & M_{an} \\ M_{b1} & M_{b2} & ... & M_{bn} \\ M_{c1} & M_{c2} & ... & M_{cn} \end{bmatrix} \tag{7.9}$$

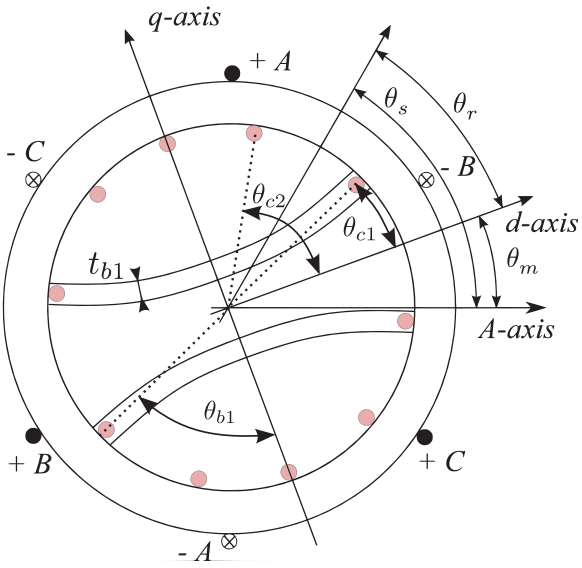

Figure 7.4: Considered LS SyM

For the reciprocity theorem, the submatrices $[R_s]$, $[R_r]$, $[L_s]$ and $[L_r]$ are symmetric, that is, for example, $M_{a1} = M_{1a}$. The submatrices $[M_{sr}]$ and $[M_{rs}]$ are transposed between each other, that is $[M_{rs}] = [M_{sr}]^T$. In [35], the machine structural symmetry of the IM and the space-vector notation was exploited to reduce the number of equations. However, such a model can not be used to describe a LS SyM because the rotor bars are not always uniformly distributed and the magnetic circuit is not doubly-cylindrical.

The torque equation is

$$[T] = [i] \frac{\partial}{\partial \theta_m^e} [L] [i] \tag{7.10}$$

7.4. Description of the analytical model

In this Chapter, the procedure to determine the inductances of a LS SyM as a function of the rotor position is illustrated. The LS SyM considered initially exhibits a non-salient stator in which there is a basic three-phase winding with $q = 1$ and $n_{cs} = 1$. The rotor exhibits one flux barrier and a rotor cage. Then, the model is generalized for a three-phase winding with $q > 1$ and $n_{cs} > 1$. The rotor conductors are represented in Fig. 7.4 with grey circles and $\theta_{c2} - \theta_{c1}$ is the angle spanned by the first rotor loop. The inductance of each winding of the machine is computed considering the MMF due to the winding itself and solving the machine magnetic circuit.

To validate the proposed model, FE analysis of a simple LS SyM has been considered. It is of the type sketched in Fig. 7.4 and its main data are in Table 7.1.

Table 7.1: Main data of the LS SRM used for the model validation

symbol	description	value	unit
p	number of pole pairs	1	-
Q_s	number of stator slots	6	-
D_s	airgap diameter	65	mm
g	airgap	0.5	mm
L_{stk}	stack lenght	100	mm
t_{b1}	flux barrier thickness	1	mm
θ_{b1}	flux barrier electrical angle	1.22	rad
l_{b1}	flux barrier length	61.3	mm

7.4.1. The airgap flux density of a single turn on the stator side

The stator magnetic scalar potential of a single turn, whose conductors are located in the stator as in Fig. 7.4 for the phase-A, is,

$$U_s(\theta_s^e, t) = -\frac{2i}{\pi} \sum_{k=1,odd}^{\infty} \frac{1}{k} \sin\, k\frac{\pi}{2} \cos\, k\theta_s^e \tag{7.11}$$

where θ_s^e is the electrical angular coordinate (fixed with the stator) whose origin is along the magnetic axis of this coil. Only odd potential harmonics exist, having considered the electrical coil pitch $\alpha^e = \pi$.

Referring to the reference frame of Fig. 7.4, it is $\theta_s^e = \theta_r^e + \theta_m^e$, where θ_m^e is the rotor position electrical angle. Expressed in the rotor reference frame, the stator magnetic potential is

$$U_s(\theta_r, t) = -\frac{2i}{\pi} \sum_{k=1,odd}^{\infty} \frac{1}{k} \sin\, k\frac{\pi}{2} \cos\, k(\theta_r + \theta_m^e) \tag{7.12}$$

Due to the rotor flux barriers, a square wave rotor magnetic potential arise. It is, in the rotor reference frame

$$U_r(\theta_r^e) = \begin{cases} U_{r1} & \frac{\pi}{2} - \theta_{b1}^e < \theta_r^e < \frac{\pi}{2} + \theta_{b1}^e \\ -U_{r1} & \frac{3\pi}{2} - \theta_{b1}^e < \theta_r^e < \frac{3\pi}{2} + \theta_{b1}^e \\ 0 & \text{elsewhere} \end{cases} \tag{7.13}$$

where θ_{b1}^e is the flux barrier electrical angle. This function is odd in the rotor reference frame. Due to the symmetry, the flux crossing the opposite flux barrier is the same and the rotor potential function exhibits half-wave symmetry (there is only odd harmonics). Its Fourier coefficients are

$$b_\mu = \frac{1}{\pi} \int_0^{2\pi} U_r(\theta_r^e) \sin \mu\theta_r^e \, d\theta_r^e = \frac{4\, U_{r1}}{\mu\pi} \left[\sin \mu \frac{\pi}{2} \sin \mu\theta_{b1}^e \right] \tag{7.14}$$

It is straightforward to see that the term $\sin \mu\frac{\pi}{2}$ deletes the even harmonics and alternates odd harmonics signs, while the term $\sin \mu\theta_{b1}^e$ modulates their amplitudes. The

rotor magnetic scalar potential can be expressed as

$$U_r(\theta_r^e, t) = \sum_{\mu=1,odd}^{+\infty} \frac{4\,U_{r1}(t)}{\mu\pi} \sin\mu\frac{\pi}{2}\, sin\mu\theta_{b1} \sin\mu\theta_r^e \tag{7.15}$$

Let note that U_{r1} is time dependent. It is obtained through the solution of the magnetic circuit for every time instant, computing the flux crossing the flux barrier [12].

$$U_{r1} = a \int_{\frac{\pi}{2p}-\theta_{b1}}^{\frac{\pi}{2p}+\theta_{b1}} U_s(\theta_r)\, d\theta_r^e \tag{7.16}$$

where a is the dimensionless coefficient

$$a = \frac{\frac{D}{2g}\frac{t_{b1}}{l_{b1}}}{1 + \frac{D\,t_{b1}\,2\theta_{b1}}{2g\,l_{b1}}} \tag{7.17}$$

After some manipulation of (7.16) and considering that only odd harmonics of U_s exist for the single turn of the phase-A, it results

$$U_{r1} = 4\frac{ai}{\pi}\Big[\sum_{k=1,odd}^{+\infty} \frac{1}{k^2 p}\, \sin k\theta_{b1}^e\, \sin k\theta_m^e\Big] \tag{7.18}$$

The airgap flux density is computed as

$$B_g(\theta_r^e) = \mu_0 \frac{-U_s(\theta_r^e) + U_r(\theta_r^e)}{g} \tag{7.19}$$

7.4.2. The inductance of windings on the stator side

From the airgap flux density B_g, the self-inductance of the phase-A is computed as

$$L_{aa} = \frac{p}{i} \int_{\theta_{neg}^r}^{\theta_{pos}^r} B_g(\theta_r)\, \frac{DL}{2}\, d\theta_r \tag{7.20}$$

where $\theta_{neg}^r = -\frac{\pi}{2p} - \theta_m$ and $\theta_{pos}^r = \frac{\pi}{2p} - \theta_m$ are the mechanical angle of the negative and positive coil side in the rotor reference frame, respectively. Note that they are function of the rotor position. Considering a phase current $i = 1A$ and developing the expression of the self-inductance L_{aa}, it becomes

$$L_{aa} = \frac{p\mu_0 DL}{2g\pi}\Big[\sum_{k=1,odd}^{+\infty} \frac{4}{k^2 p}\Big(1 - 2U_{r1}\, \sin k\theta_{b1}^e\, \sin k\theta_m^e\Big)\Big] \tag{7.21}$$

It is confirmed that the inductance harmonics decrease with $\frac{1}{k^2}$. The derivative of the phase-A inductance is, remembering that $\theta_m^e = \omega_m^e\, t$

$$\frac{d}{dt}L_{aa} = \frac{p\mu_0 DL}{2g\pi}\Big[\sum_{k=1,odd}^{+\infty} \frac{4}{k^2 p}\Big(-2U_{r1}\, \sin k\theta_{b1}^e\, \cos k\theta_m^e\, k\omega_m^e - 2\frac{d}{dt}U_{r1}\, \sin k\theta_{b1}^e\, \sin k\theta_m^e\Big)\Big] \tag{7.22}$$

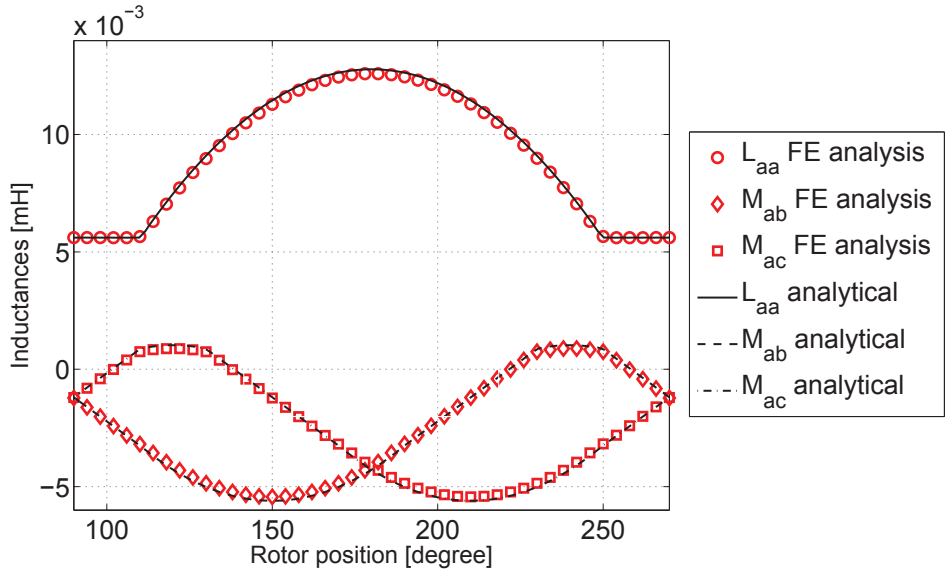

Figure 7.5: self- (L_{aa}) and mutual-inductances (M_{ab} and M_{ac}) as a function of the rotor position

where $\frac{d}{dt}U_{r1}$ is computed from the derivation of equation (7.16). As far the mutual inductances between different stator phases are concerned, they can be computed with the same procedure by varying the integration interval of equation (7.20). For example, the mutual inductances between the phase-A and phase-B ($M_{ab} = M_{ba}$) is computed integrating equation (7.20) between $\theta^r_{neg} = -\frac{\pi}{2p} + \frac{2\pi}{3p} - \theta_m$ and $\theta^r_{pos} = \frac{\pi}{2p} + \frac{2\pi}{3p} - \theta_m$. The self-inductance of the other stator phases are computed with the same procedure considering that they are shifted by $2/3\pi$ and $4/3\pi$ with respect the phase-A. Thus, each element of the submatrices $[L_s]$ and $\frac{d}{dt}[L_s]$ can be determined.

FE analysis is carried out on the LS SyM whose main data are in Table 7.1. Each stator phase has been supplied separately and the self- and mutual-inductances are computed as the ratio between flux linkage and current for different rotor positions.

Fig. 7.5 shows the self- (L_{aa}) and mutual-inductances (M_{ab} and M_{ac}) as a function of the rotor position achieved by FE analysis, together with those achieved by means of the analytical model. In the analytical model, harmonics up to order 99 are considered. An excellent agreement is observed. As far as L_{aa} is concerned, its trend as a function of the rotor position exhibits a constant region and a parabolic region. In particular, L_{aa} is constant when the two conductors of the phase-A are in correspondence of the d-axis and in general for $\frac{\pi}{2p} - \theta_{b1} < \theta_m < \frac{\pi}{2p} + \theta_{b1}$. On the other hand, L_{aa} exhibits a parabolic trend for the other positions. It is easy to understand that the time derivative of L_{aa} is very high in correspondence of the positions $\frac{\pi}{2p} - \theta_{b1}$ and $\frac{\pi}{2p} + \theta_{b1}$, that is where there is the change of slope.

7.4.3. The inductance of windings on the stator side in the case of q¿1 and $n_{cs} > 1$

Let $N = q\,n_{cs}$ be the total number of turns of each stator phase. Each conductor carries the same current i and each group of n_{cs} turns is mutually displaced by a constant electrical angle α_s^e. If the axis of such group of turns lie on the axis $\theta_s^e = 0$, that is the same axis of the single coil considered previously, the stator magnetic scalar potential of this group of turns is, in the stator reference frame,

$$U_{s,q>1}(\theta_s^e, t) = N \sum_{k=1}^{\infty} K_{wk}\, U_s(\theta_s^e, t) = -N \sum_{k=1}^{\infty} K_{wk} \Big[\frac{2i}{\pi} \sum_{k=1,odd}^{\infty} \frac{1}{k} sin\, k\frac{\pi}{2}\, cos\, k\theta_s^e \Big] \quad (7.23)$$

where

$$K_{wk} = \frac{\sin qk\frac{\alpha_s^e}{2}}{q \sin k\frac{\alpha_s^e}{2}} \quad (7.24)$$

is the winding distribution factor relative to the harmonic k. The term K_{wk} is composed by both even and odd harmonics. However, considering that the term $sin\, k\frac{\pi}{2}$ of U_s nullify the even harmonics, the stator magnetic scalar potential of the group of turns is

$$U_{s,q>1}(\theta_s^e, t) = -N\, \frac{2i}{\pi} \sum_{k=1,odd}^{\infty} K_{wk} \frac{1}{kp} sin\, k\frac{\pi}{2}\, cos\, k\theta_s^e \quad (7.25)$$

The expression of U_{r1} becomes

$$U_{r1} = 4N \frac{ai}{\pi} \Big[\sum_{k=1,odd}^{+\infty} K_{wk} \frac{1}{k^2 p}\, \sin k\theta_{b1}^e\, \sin k\theta_m^e \Big] \quad (7.26)$$

The inductances of a stator winding with $q > 1$ must be computed considering the effective conductors distribution. In this case it is not correct just multiplying the inductance of a single turn by $N \sum K_{wk}$, but it is necessary to integrate the flux density over each each group of n_{cs} turns. It yields, for a current $i = 1A$,

$$L_{aa} = p n_{cs} \sum_{h=1}^{q} \int_{\theta_{h,neg}}^{\theta_{h,pos}} B_g(\theta_r) \frac{DL_{stk}}{2}\, d\theta_r \quad (7.27)$$

where $\theta_{h,neg}$ and $\theta_{h,pos}$ are the mechanical position of the conductors of the phase-A in the slot number h of q, in the rotor reference frame.

Fig. 7.6 shows the self- and mutual-inductances of the phase-A in the case of $q = 2$. It should be noted that the trend of the self-inductance is smoother with respect to that of the case $q = 1$ (Fig. 7.5).

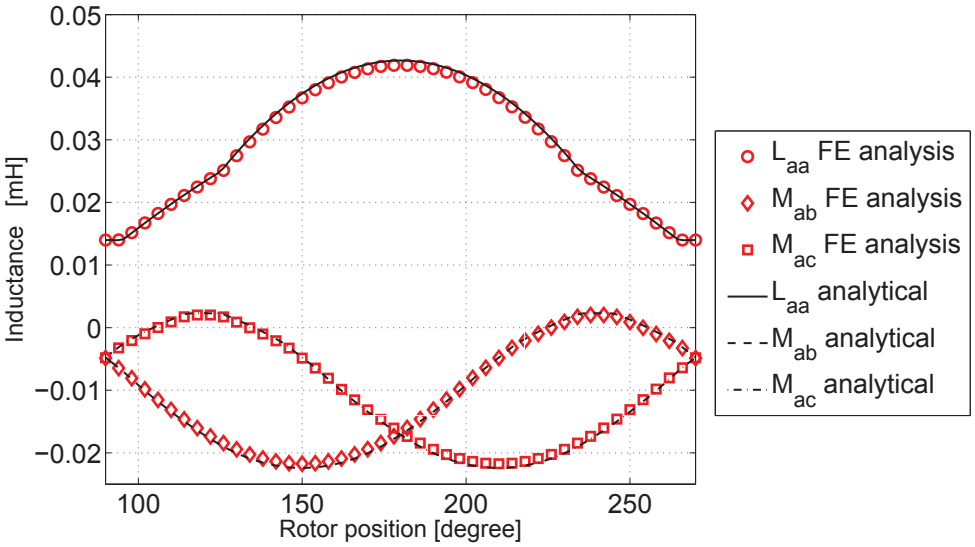

Figure 7.6: self- (L_{aa}) and mutual-inductances (M_{ab} and M_{ac}) as a function of the rotor position, $q = 2$

7.4.4. The inductance of the rotor loops

The self- and mutual-inductance of the rotor loops are constant with the rotor position. Let refer to Fig. 7.4. Consider two rotor bars, located at θ_{c1} and θ_{c2}, respectively, with respect the rotor reference frame and the portion of end circuit connecting them, forming a rotor loop. If this loop is excited by a current i, it produces a magnetic scalar potential referred to the rotor reference frame of

$$U_{loop}(\theta_r, t) = -\frac{2i}{\pi} \sum_{k=1}^{\infty} \frac{1}{k} sin\, k \frac{\delta}{2} cos\, k(\theta_r - \theta_c) \tag{7.28}$$

where $\delta = \theta_{c2} - \theta_{c1}$ and $\theta_c = \frac{\theta_{c2}+\theta_{c1}}{2}$. Such a loop exhibits a pitch different from $\frac{\pi}{2}$ and $U_{loop}(\theta_r, t)$ is composed by both even and odd harmonics.

As described in the previous Subsections, a magnetic potential due to the rotor flux barriers contributes to the airgap flux density. However, in this case the flux barrier magnetic potential does not exhibit half-wave symmetry because each flux barrier is crossed by a different flux. In the case of $p = 1$ is, in the rotor reference frame

$$U_{r,loop}(\theta_r) = \begin{cases} U'_{r1} & \frac{\pi}{2} - \theta_{b1} < \theta_r < \frac{\pi}{2} + \theta_{b1} \\ U''_{r1} & \frac{3\pi}{2} - \theta_{b1} < \theta_r < \frac{3\pi}{2} + \theta_{b1} \\ U_{r0} & \text{elsewhere} \end{cases} \tag{7.29}$$

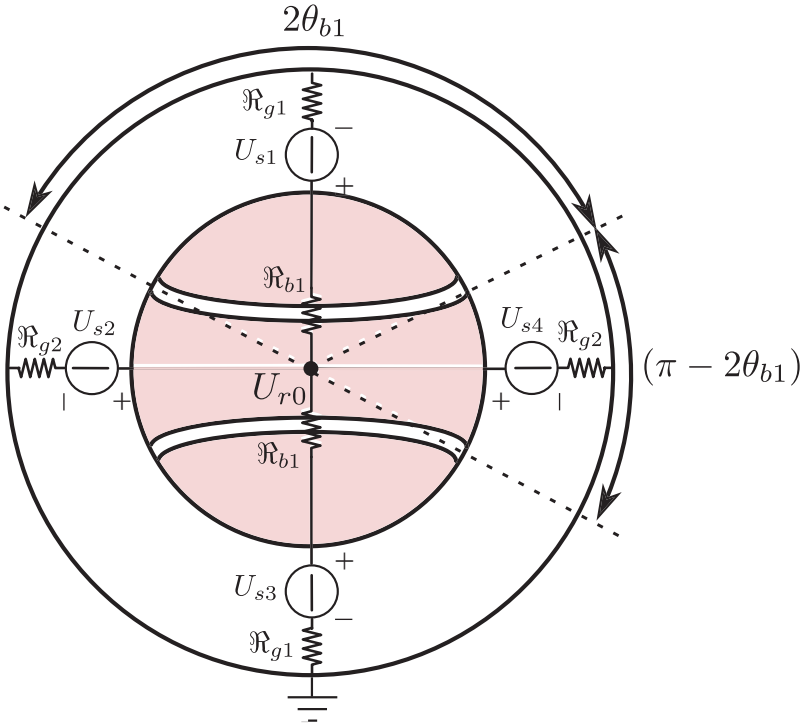

Figure 7.7: LS SyM magnetic circuit layout

The flux barrier magnetic potential Fourier coefficients are:

$$\begin{aligned}
a_{0,loop} &= \frac{1}{2\pi}\int_0^{2\pi} U_{r,loop}(\theta_r)\,d\theta_r \\
&= (U_{r1}^{'} + U_{r1}^{''})\frac{\theta_{b1}}{\pi} + (\pi - 2\theta_{b1})\frac{U_{r0}}{\pi} \\
a_{\mu,loop} &= \frac{1}{\pi}\int_0^{2\pi} U_{r,loop}(\theta_r)\sin\mu\theta_r\,d\theta_r \\
&= -\frac{2}{\mu\pi}\sin\mu\theta_{b1}\Big(-U_{r1}^{'}\cos\mu\frac{\pi}{2} - U_{r1}^{''}\cos\mu\frac{3\pi}{2} + U_{r0}\cos\mu\frac{\pi}{2} + U_{r0}\cos\mu\frac{3\pi}{2}\Big) \\
b_{\mu,loop} &= \frac{1}{\pi}\int_0^{2\pi} U_{r,loop}(\theta_r)\cos\mu\theta_r\,d\theta_r \\
&= -\frac{2}{\mu\pi}\sin\mu\theta_{b1}\Big(-U_{r1}^{'}\sin\mu\frac{\pi}{2} - U_{r1}^{''}\sin\mu\frac{3\pi}{2} + U_{r0}\sin\mu\frac{\pi}{2} + U_{r0}\sin\mu\frac{3\pi}{2}\Big)
\end{aligned} \tag{7.30}$$

$U_{r1}^{'}$ and $U_{r1}^{''}$ and $U_{r0}^{'}$ are computed solving the whole magnetic circuit of the LS SyM, which is illustrated in Fig. 7.7 and Fig. 7.8. The reluctance of the airgap over the angles $2\theta_{b1}$ and $\pi - 2\theta_{b1}$, as illustrated in Fig. 7.7, are

$$\Re_{g1} = \frac{g}{\mu_0\, L_{stk}\, R\,(2\theta_{b1})} \qquad \Re_{g2} = \frac{g}{\mu_0\, L_{stk}\, R\,(\pi - 2\theta_{b1})} \tag{7.31}$$

and

$$\Re_{gb} = \frac{t_{b1}}{\mu_0\, L_{stk}\, l_b} \tag{7.32}$$

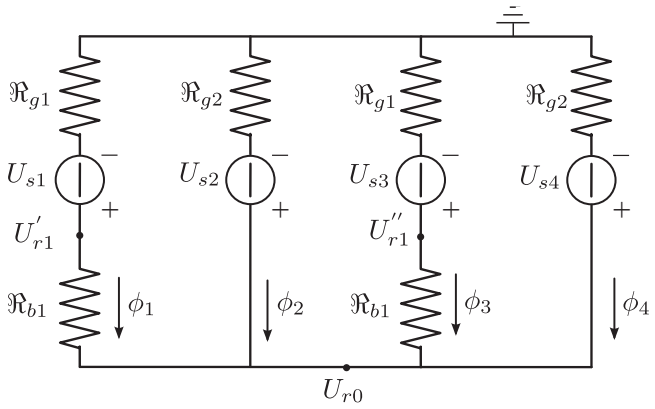

Figure 7.8: LS SyM magnetic circuit equivalent circuit

is the reluctance of the flux barrier. The MMF sources from U_{s1} to U_{s4} are computed from the airgap potential U_{loop} as

$$\begin{aligned}
U_{s1} &= \frac{1}{2\theta_{b1}} \int_{\frac{\pi}{2}-\theta_{b1}}^{\frac{\pi}{2}+\theta_{b1}} U_{loop}(\theta_r)\, d\theta_r \\
U_{s2} &= \frac{1}{\pi - 2\theta_{b1}} \int_{\frac{\pi}{2}+\theta_{b1}}^{\frac{3\pi}{2}-\theta_{b1}} U_{loop}(\theta_r)\, d\theta_r \\
U_{s3} &= \frac{1}{2\theta_{b1}} \int_{\frac{3\pi}{2}-\theta_{b1}}^{\frac{3\pi}{2}+\theta_{b1}} U_{loop}(\theta_r)\, d\theta_r \\
U_{s4} &= \frac{1}{\pi - 2\theta_{b1}} \int_{\frac{3\pi}{2}+\theta_{b1}}^{\frac{\pi}{2}-\theta_{b1}} U_{loop}(\theta_r)\, d\theta_r
\end{aligned} \tag{7.33}$$

The expression of the flux barrier magnetic potential is

$$U_{r,loop}(\theta_r) = a_{0,loop} + \sum_{\mu=1}^{\infty} \left[a_{\mu,loop} \cos \mu\theta_r + b_{\mu,loop} \sin \mu\theta_r \right] \tag{7.34}$$

and the airgap flux density is

$$B_{g,loop}(\theta_r) = \mu_0 \frac{-U_{loop}(\theta_r) + U_{r,loop}(\theta_r)}{g} \tag{7.35}$$

The self- and mutual-inductances of the rotor loops can easily be computed integrating the flux density $B_{g,loop}$.

Table 7.2 reports the value of self-inductance of a rotor loop computed with the analytical model and with FE analysis. Fig. 7.9 shows the resultant airgap flux density when a current of $i = 1A$ is flowing through the considered rotor loop. It can be noted that the analytical model predict with accuracy the airgap flux density. From Table 7.2, a slight higher error is for the value of the self-inductance, due to the leakage fluxes which are neglected in the analytical model.

In the case of $p > 1$ the magnetic circuit is more complex than that of Fig. 7.8 as there are more than 2 flux barriers. However, the same procedure can be used to determine the airgap flux density and the inductances of the rotor loops.

Table 7.2: Self-inductance of a rotor loop, FE vs analytical model

symbol	description	value	unit
θ_{c1}	first rotor bar angle	1.3464	rad
θ_{c2}	second rotor bar angle	π	rad
L_{loop}	loop self-inductance	1.7e-3	mH
$L_{loop,FE}$	loop self-inductance from FE	1.8e-3	mH

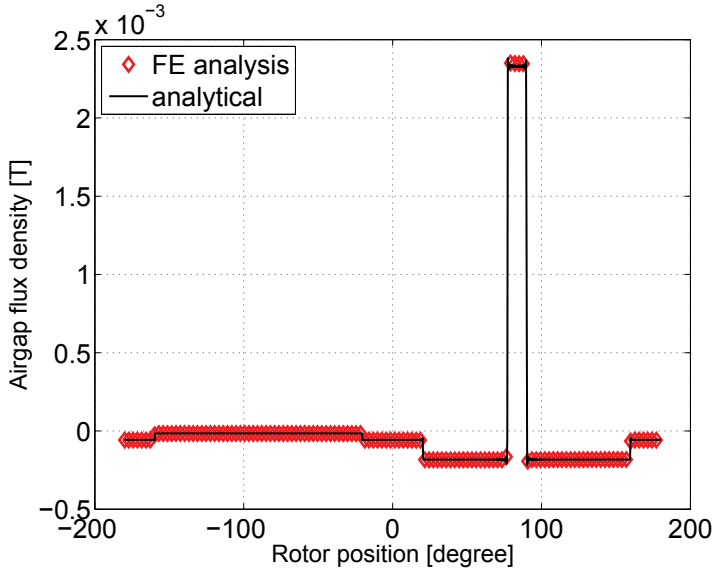

Figure 7.9: Airgap flux density when a current of $i = 1A$ is flowing through the considered rotor loop

7.4.5. The mutual-inductances between stator and rotor windings

The terms of the submatrix $[M_{sr}]$ can be determined either by integrating the airgap flux density due to the stator or rotor windings. It is interesting to remember an interesting aspect of the mutual interaction between windings: the waveform of the induced voltage in a winding is identical with that of the field intensity produced by this winding. In the case studied here, the stator windings are capable to produce only odd field harmonics. Thus, only the odd harmonics of the field produced by each rotor loop affect the computation of the stator-rotor mutual inductances. The even harmonics of the field, which are necessary to compute the terms of the submatrix $[L_r]$, can be neglected in the computation of the stator-rotor mutual inductances. As shown in Fig. 7.10, there are only odd harmonics of the stator-rotor mutual inductances (half-wave symmetry).

Fig. 7.10 shows the mutual inductances between the stator windings (with $n_{cs} = 1$ and $q = 1$) and the rotor loop whose conductors are in the position θ_{c1} and θ_{c2}, namely, rotor loop 1. There is an excellent agreement between the results of the analytical model and that of the FE analysis. Similar results (not reported here for the sake of brevity) are achieved for a stator with $n_{cs} > 1$ and $q > 1$.

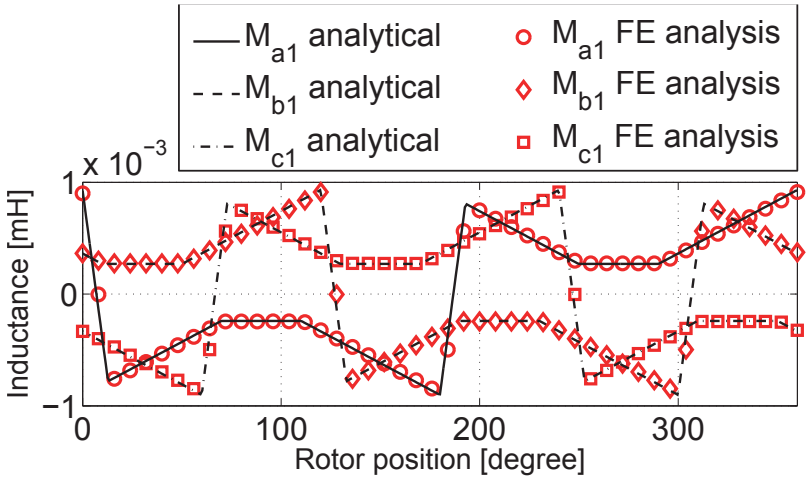

Figure 7.10: Mutual inductances between the stator windings (with $n_{cs} = 1$ and $q = 1$) and the first rotor loop

7.4.6. Integration of the differential equations of the machine

Equation (7.2) is rearranged to highlight the currents $[i]$ as state variable:

$$\frac{d}{dt}[i] = [L]^{-1}\left[[v] - \left([R] + \frac{d}{dt}[L]\right)[i]\right] \tag{7.36}$$

where $[L]^{-1}$ is the inverse of the matrix $[L]$. It is worth noticing that only the derivative of the submatrix L_{loops} is zero.

As far as the stator winding connection mode is concerned, if the stator windings are star-connected, zero sequence third harmonic (and in general multiple of 3) stator currents can not flow.

The application of the proposed method to the computation of the parasitic torques by the integration of equation (7.36) will be subject of future works.

7.5. Conclusions

This Chapter has firstly described the LS SyM equations. The LS SyM is described as a set of multiple coupled circuits defined by self- and mutual-inductance matrices. The inductance coefficient of all the LS SyM circuits are analytically computed in terms of winding space harmonics. Differently from the literature, the analysis is applied on a machine which is not doubly-cylindrical (IM) or with salient pole (generator), but which contains flux barriers in the rotor, as a SRM. One advantage of this approach is that it is also applicable to cage rotors with non-integral number of rotor bars per stator pole-pair. The modification of the stator field due to rotor currents is taken into account adopting the coupled magnetic circuit theory. No assumption has been made regarding the currents waveform and the model is valid for any type of excitation, as well as during transient operation.

The self- and mutual inductances from the analytical model are compared with those achieved from FE as a function of the rotor position, showing an excellent agreement.

Solving the resulting LS SyM differential equations, synchronous and asynchronous torque dips in the torque versus speed curve can be determined.

7.6. Appendix B

In this Appendix, the effect of the $\alpha-\beta$ and $d-q$ transformations on the stator inductances (elements of the submatrix $[L_s]$) is analyzed. Let consider the self- and mutual-inductances of the stator winding expressed in the complex form of the fourier series.

$$\begin{aligned}
L_{aa} &= \sum_{n=-\infty}^{\infty} \dot{L}_{aa,n} e^{jn\theta} \\
L_{bb} &= \sum_{n=-\infty}^{\infty} \dot{L}_{aa,n} e^{-jn\frac{2\pi}{3}} e^{jn\theta} \\
L_{cc} &= \sum_{n=-\infty}^{\infty} \dot{L}_{aa,n} e^{-jn\frac{4\pi}{3}} e^{jn\theta} \\
M_{ab} = M_{ba} &= \sum_{n=-\infty}^{\infty} \dot{M}_{ab,n} e^{jn\theta} \\
M_{bc} = M_{cb} &= \sum_{n=-\infty}^{\infty} \dot{M}_{ab,n} e^{-jn\frac{2\pi}{3}} e^{jn\theta} \\
M_{ca} = M_{ac} &= \sum_{n=-\infty}^{\infty} \dot{M}_{ab,n} e^{-jn\frac{4\pi}{3}} e^{jn\theta}
\end{aligned} \tag{7.37}$$

Applying the $\alpha-\beta$ transformation to the submatrix $[L_s]$, that is $[L_{\alpha\beta}] = [C]^{-1}[L_s][C]$, where

$$[C] = \begin{bmatrix} 1 & 0 & 1 \\ -\frac{1}{2} & \frac{\sqrt{3}}{2} & 1 \\ -\frac{1}{2} & -\frac{\sqrt{3}}{2} & 1 \end{bmatrix} \qquad [C]^{-1} = \frac{2}{3}\begin{bmatrix} 1 & -\frac{1}{2} & -\frac{1}{2} \\ 0 & \frac{\sqrt{3}}{2} & -\frac{\sqrt{3}}{2} \\ \frac{1}{2} & \frac{1}{2} & \frac{1}{2} \end{bmatrix} \tag{7.38}$$

one obtains

$$\begin{aligned}
L_{\alpha,n} &= \sum_{n=-\infty}^{\infty} \dot{L}_{\alpha,n} e^{jn\theta} \\
L_{\beta,n} &= \sum_{n=-\infty}^{\infty} \dot{L}_{\beta,n} e^{jn\theta} \\
L_{\alpha\beta,n} &= \sum_{n=-\infty}^{\infty} \dot{L}_{\alpha\beta,n} e^{jn\theta}
\end{aligned} \tag{7.39}$$

After some algebraic manipulation, the complex coefficients are

$$\begin{aligned}
\dot{L}_{\alpha,n} &= \frac{2}{3}[\dot{L}_{aa,n}(1 + \frac{e^{-jn\frac{2\pi}{3}}}{4} + \frac{e^{-jn\frac{4\pi}{3}}}{4}) + \dot{M}_{ab,n}(-1 - e^{-jn\frac{4\pi}{3}} + \frac{e^{-jn\frac{2\pi}{3}}}{2})] \\
\dot{L}_{\beta,n} &= \frac{1}{2}[\dot{L}_{aa,n}(e^{-jn\frac{2\pi}{3}} + e^{-jn\frac{4\pi}{3}}) - 2\dot{M}_{ab,n}(e^{-jn\frac{2\pi}{3}})] \\
\dot{L}_{\alpha\beta,n} &= \frac{\sqrt{3}}{6}[\dot{L}_{aa,n}(e^{-jn\frac{4\pi}{3}} - e^{-jn\frac{2\pi}{3}}) + 2\dot{M}_{ab,n}(1 - e^{-jn\frac{4\pi}{3}})]
\end{aligned} \tag{7.40}$$

It is worth noticing that the elements of the matrix $[L_{\alpha\beta}]$ contain the same harmonic spectrum of the elements of the matrix $[L_s]$. The coefficients $\dot{L}_{\alpha,n}$, $\dot{L}_{\beta,n}$ and $\dot{L}_{\alpha\beta,n}$ exhibit different values as a function of the harmonic order n. Defining

$$\begin{aligned}\dot{A}_n &= \dot{L}_{aa,n} - \dot{M}_{ab,n} \\ \dot{B}_n &= \frac{\dot{L}_{aa,n}}{2} - \dot{M}_{ab,n}(\frac{j\sqrt{3}}{2} + \frac{1}{2}) \\ \dot{C}_n &= \frac{\dot{L}_{aa,n}}{2} + \dot{M}_{ab,n}(\frac{j\sqrt{3}}{2} - \frac{1}{2})\end{aligned} \tag{7.41}$$

the results of Table 7.3 are achieved, where t represents a generic integer number.

Table 7.3: Complex coefficients of the α– β–inductances as a function of the harmonic order n

harmonic order	$\dot{L}_{\alpha,n}$	$\dot{L}_{\beta,n}$	$\dot{L}_{\alpha\beta,n}$
$n = 3t$	$\dot{A}_n$	$\dot{A}_n$	0
$n = 3t-2$	$\dot{B}_n$	$-\dot{B}_n$	$j\dot{B}_n$
$n = 3t-1$	$\dot{C}_n$	$-\dot{C}_n$	$-j\dot{C}_n$

The inductances in the d– and q–axis reference frame are $[L_{dq}] = [C_2]^{-1}\,[L_{\alpha\beta}]\,[C_2]$, where

$$[C_2] = \begin{bmatrix} \cos(\theta_m^e) & -\sin(\theta_m^e) & 0 \\ \sin(\theta_m^e) & \cos(\theta_m^e) & 0 \\ 0 & 0 & 1 \end{bmatrix} \qquad [C_2]^{-1} = \begin{bmatrix} \cos(\theta_m^e) & \sin(\theta_m^e) & 0 \\ -\sin(\theta_m^e) & \cos(\theta_m^e) & 0 \\ 0 & 0 & 1 \end{bmatrix} \tag{7.42}$$

Considering that $\cos(\theta_m^e) = \frac{e^{j\theta_m^e}+e^{-j\theta_m^e}}{2}$ and $\sin(\theta_m^e) = -j\frac{e^{j\theta_m^e}-e^{-j\theta_m^e}}{2}$, the matrix C_2 can be rewritten as

$$\begin{aligned}[C_2] &= \begin{bmatrix} \frac{e^{j\theta_m^e}+e^{-j\theta_m^e}}{2} & j\frac{e^{j\theta_m^e}-e^{-j\theta_m^e}}{2} & 0 \\ -j\frac{e^{j\theta_m^e}-e^{-j\theta_m^e}}{2} & \frac{e^{j\theta_m^e}+e^{-j\theta_m^e}}{2} & 0 \\ 0 & 0 & 1 \end{bmatrix} \\ &= \frac{e^{j\theta_m^e}}{2}\begin{bmatrix} 1 & j & 0 \\ -j & 1 & 0 \\ 0 & 0 & 2e^{-j\theta_m^e} \end{bmatrix} + \frac{e^{-j\theta_m^e}}{2}\begin{bmatrix} 1 & -j & 0 \\ j & 1 & 0 \\ 0 & 0 & 2e^{j\theta_m^e} \end{bmatrix}\end{aligned} \tag{7.43}$$

Using the data of Table 7.3 and after algebraic manipulations one obtain, as a function of the harmonic order,

$$\dot{L}_d = \begin{cases} \dot{L}_{d,n} = \frac{1}{2}(\dot{L}_{\alpha,n} + \dot{L}_{\beta,n}) = \dot{A}_n & n = 3t \\ \dot{L}_{d,n+2} = \frac{1}{4}(\dot{L}_{\alpha,n} - \dot{L}_{\beta,n} - j2\dot{B}_{\alpha\beta,n}) = \dot{B}_n & n = 3t-2 \\ \dot{L}_{d,n-2} = \frac{1}{4}(\dot{L}_{\alpha,n} - \dot{L}_{\beta,n} + j2\dot{L}_{\alpha\beta,n}) = \dot{C}_n & n = 3t-1 \end{cases} \tag{7.44}$$

$$\dot{L}_q = \begin{cases} \dot{L}_{q,n} = \frac{1}{2}(\dot{L}_{\alpha,n} + \dot{L}_{\beta,n}) = \dot{A}_n & n = 3t \\ \dot{L}_{q,n+2} = \frac{1}{4}(\dot{L}_{\beta,n} - \dot{L}_{\alpha,n} + j2\dot{L}_{\alpha\beta,n}) = -\dot{B}_n & n = 3t-2 \\ \dot{L}_{q,n-2} = \frac{1}{4}(\dot{L}_{\beta,n} - \dot{L}_{\alpha,n} - j2\dot{L}_{\alpha\beta,n}) = -\dot{C}_n & n = 3t-1 \end{cases} \tag{7.45}$$

$$\dot{L}_{dq} = \begin{cases} \dot{L}_{dq,n} = \dot{L}_{\alpha\beta,n} = 0 & n = 3t \\ \dot{L}_{dq,n+2} = \frac{1}{4}(j\dot{L}_{\alpha,n} - j\dot{L}_{\beta,n} + 2\dot{L}_{\alpha\beta,n}) = j\dot{B}_n & n = 3t-2 \\ \dot{L}_{dq,n-2} = \frac{1}{4}(-j\dot{L}_{\alpha,n} + j\dot{L}_{\beta,n} + 2\dot{L}_{\alpha\beta,n}) = -j\dot{C}_n & n = 3t-1 \end{cases} \tag{7.46}$$

From (7.44), (7.45) and (7.46), it is confirmed that the inductances in the d– and q–axis reference frame contain only harmonics whose order is $3t$, which means that their periodicity is $\frac{1}{6}$ of the electrical period. It is also worth noticing that the d– and q–axis inductance coefficients are the same that of the α– and β–inductance coefficients, respectively.

Chapter 8

Analysis and Test of the Sensorless Capability of Induction Motors with Created Saliency

This Chapter presents various experimental tests on the sensorless capability of induction motors. An intentionally created saliency is introduced in the rotor so as to allow the rotor position to be estimated by means of a high frequency injected signal in the stator winding. Experimental measurements are carried out on three prototypes, two with saliency and the third without saliency, as reference. The critical aspects in the prototype realization are discussed in this Chapter. Suggestion on how to solve them from the machine design point of view are included. The rotor saliency has been measured by means of a high frequency injection. Then, the steady state performance have been measured, together with the mechanical characteristic of the three prototypes. FE analysis is used to predict the variation of the IM parameters with rotor position. The results are compared with those achieved from measurements.

8.1. Introduction

The high cost of rare-earth PM, together with the advances in solid-state control technology, leads designers to reconsider IM for variable speed drive applications. Several advantages such as reliability and lower cost come from the absence of the speed sensor and the associated signal wiring in IM drives. Thus, especially in the last two decades, a continuous trend was to find solutions allowing an IM to be controlled at high performance without shaft transducers. Different approaches for sensorless IM drives have been developed. Methods that rely upon tracking the back-EMF to estimate flux or rotor velocity fail at low excitation frequency [98]. Models that assume a sinusoidal flux density distribution in the air gap (fundamental models) also have their limits at zero stator frequency. On the other hand, signal injection methods exploit machine properties that are not reproduced by the fundamental machine model, allowing information on rotor position to be achieved at zero-speed [99]. A high HF voltage signal

is injected within the stator winding and the rotor position can be detected from the current response detecting anisotropic properties of the machine [99–104].

Different approaches can be followed to obtain rotor anisotropy in an IM. For example, in [105], the authors designed an outer-section cage whose resistance is position-dependent [105]. In [106], the saturation-induced saliencies in the stator incremental inductance are used to achieve sensorless control of IM. Other concepts to estimate the rotor position rely on the harmonics due to rotor slotting [107–109]. Another solution to achieve a magnetic saliency in a squirrel cage rotor is to introduce a variation of the width and depth of the rotor slot openings [110, 111]. The idea is to achieve a periodic variation of rotor leakage inductance around the rotor circumference. The rotor saliency exhibits the same number of poles of the motor, that is, it is repeated each $360/p$ degrees.

The response to an injected HF signal reflects all anisotropies, field dependant and position dependant. When informations are extracted by a particular anisotropy, the other act as disturbances [98], and proper signal processing is required. Methods to treat the modulation harmonics due to saturation for sensorless position IM drives using the principle of HF injection are proposed in [112–114]. In [115], the authors described a compensation strategy that suppress the inverter clamping modulation due to inverter dead-time in addition to the saturation saliency.

The rotor saliency achieved with the slot opening modulation can be very large and its amplitude does not vary considerably with the signal frequency [110]. In a rotor with such a saliency, skewing can be adopted since the rotor position information does not rely upon rotor slotting [116,117]. On the contrary, the skewing of rotor bars has a positive effect from the point of view of tracking the additional saliency, since it reduces the noise due to the slot impedance modulation, as it will be shown in Section 8.4.1.

In this Chapter, experimental measurements on three IM prototypes are presented. The first prototype is a standard IM. The other two prototypes have been designed with a rotor saliency by means of the variation of the width and depth of the rotor slot openings along the airgap. Practical aspects on the realization of the two prototypes with saliency are discussed in the Chapter, with particular reference to the die casting and milling process. Considerations about the feasibility of a robust solution for general industrial use of IM with introduced saliency are also given. The dynamic and steady state performance variation given by such a rotor modification are experimentally quantified, as well as the HF parameter modulation. FE analysis is carried out to achieve an estimation of the HF response of the prototypes as a function of rotor position. The approach proposed in [73,118] has been used to compute the IM parameters. Then, the terminal impedance achieved by means of FE has been compared with the measured one, validating the model.

8.2. IM High Frequency model

A model of the machine describing the behavior of a synchronous machine at high frequency is explained in detail in [119]. The same model can be extended also to study the HF response of the IM. Operation at standstill is assumed (i.e. mechanical speed $\omega_m = 0$) and the rotor position is a parameter in the analysis. Sinusoidal steady state is assumed: phasors are denoted with an overline and complex quantity are dotted. The machine parameters at the stator ports in the stator reference frame is in the form

$$\begin{bmatrix} \overline{U}_{s\alpha} \\ \overline{U}_{s\beta} \end{bmatrix} = \begin{bmatrix} \dot{z}_{\alpha\alpha} & \dot{z}_{\alpha\beta} \\ \dot{z}_{\beta\alpha} & \dot{z}_{\beta\beta} \end{bmatrix} \begin{bmatrix} \overline{I}_{s\alpha} \\ \overline{I}_{s\beta} \end{bmatrix} \tag{8.1}$$

At high excitation frequency, due to skin effect in rotor bars, flux lines are mainly confined to the rotor surface and the stator and rotor resistances could be neglected in the stator voltage equations. In the stationary reference frame, the rotor leakage inductance exhibits an alternating component due to the introduced saliency [110]. For any rotor position, the parameters in (8.1) can be computed as

$$\begin{aligned} \dot{z}_{\alpha\alpha} &= \frac{\overline{U}_{s\alpha}}{\overline{I}_{s\alpha}}\Big|_{\overline{I}_{s\beta}=0} & \dot{z}_{\beta\beta} &= \frac{\overline{U}_{s\beta}}{\overline{I}_{s\beta}}\Big|_{\overline{I}_{s\alpha}=0} \\ \dot{z}_{\alpha\beta} &= \frac{\overline{U}_{s\alpha}}{\overline{I}_{s\beta}}\Big|_{\overline{I}_{s\alpha}=0} & \dot{z}_{\beta\alpha} &= \frac{\overline{U}_{s\beta}}{\overline{I}_{s\alpha}}\Big|_{\overline{I}_{s\beta}=0} \end{aligned} \tag{8.2}$$

At high frequency, the stator flux linkages are mainly due to the leakage fluxes and the impedances seen from the stator terminal correspond mainly to the leakage reactances.

In this work, the two-dimensional (2-D) FE procedure to compute the IM parameters is that proposed in [73,118]. The analysis is carried out in the stationary reference frame. A pulsating magnetic field is imposed in the stator winding, that is, each axis is supplied independently from the other. The equivalent series resistance and inductance are computed from flux linkages. Then, considering a Gamma-type equivalent circuit, the complete terminal impedance is computed by adding the other parameters (analytically computed) such as stator resistance and 3D parameters.

8.3. Description of the prototypes

The prototypes are 4–pole, 2-kW IM with $Q_s = 36$ stator slots and $Q_r = 28$ rotor slots. The rotors are skewed to reduce the harmonics due to slotting. A skewing angle of 19 mechanical degrees has been adopted. The prototypes have been manufactured using laser cutting and standard die-casting.

Three different rotors have been manufactured. The first rotor is a standard IM rotor which is designed without any spatial modulation in the slot openings geometry. The slot opening height is $h_{so} = 0.5\ mm$ and the slot opening width is $w_{so} = 1.0\ mm$. A picture of the lamination of the second rotor is shown in Fig. 8.1(a). It is designed so as to have a sinusoidally distributed spatial modulation in the rotor slot opening height combined with a variation in slot opening width along the airgap. The rotor slot shape remains unchanged. Therefore, slot type A in Fig. 8.1(a) exhibits the maximum

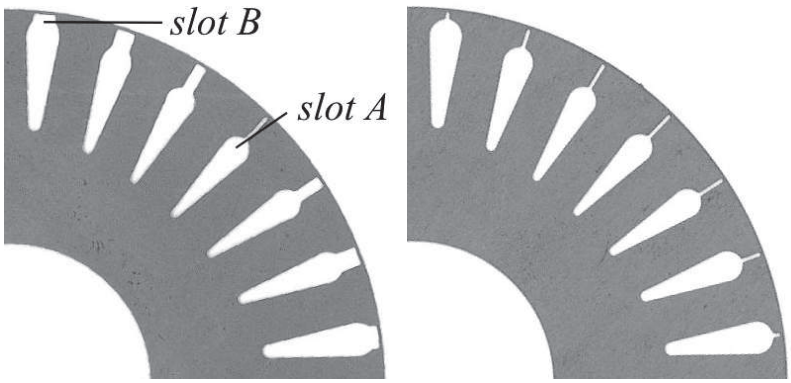

(a) Prototype 2 (b) Prototype 3

Figure 8.1: Photo of the laminations

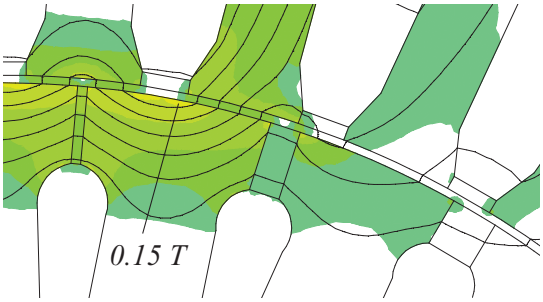

Figure 8.2: Distribution of leakage flux-lines, prototype 2 when stator winding is supplied at 300 Hz

slot opening height and minimum slot opening width, that is $h_{so-max} = 4.0\ mm$ and $w_{so-min} = 0.5\ mm$. On the other hand, slot type B exhibits the minimum slot opening height and the maximum slot opening width, that is $h_{so-min} = 1.0\ mm$ and $w_{so-max} = 2.9\ mm$. In the third rotor, whose lamination is shown in Fig. 8.1(b), only the rotor slot opening height has been sinusoidally modulated from a minimum of $h_{so-min} = 1.0\ mm$ to a maximum of $h_{so-max} = 4.0\ mm$. Fig. 8.2 and Fig. 8.3 show how leakage fluxes are distributed in the slot openings of prototype 2 and 3, respectively, when a 300 Hz pulsating field is imposed in the stator winding.

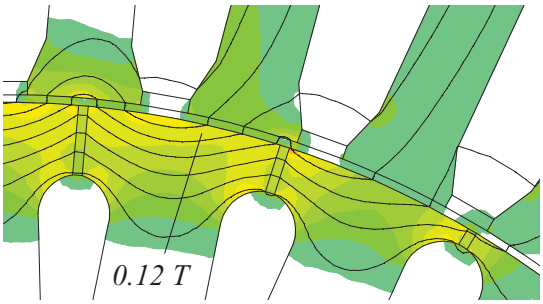

Figure 8.3: Distribution of leakage flux-lines, prototype 3 when stator winding is supplied at 300 Hz

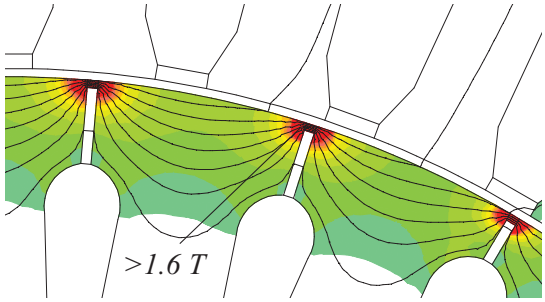

Figure 8.4: Distribution of leakage flux-lines, prototype 3 with iron bridges when stator winding is supplied at 300 Hz

8.3.1. Prototype defects

The rotor has been designed with open slots so as to avoid localized saturation of the rotor slot bridge. However, a thin iron bridge has been left to facilitate the die casting process, as visible in Fig. 8.1. After that, the rotors have been lathed so as to remove this iron bridge. However, it has been observed that not all iron bridges were completely removed on prototype 2 and 3. Certain rotor slots are still closed by a thin iron bridge. This is probably due to the lamination deformation during the die casting operations. The thickness of the iron bridge results to be increased for slots with narrow slot opening, while it is almost completely removed for slots with larger slot openings. This is related to the fact that the narrowest rotor slot openings result not entirely filled by Aluminium. Then, regarding prototype 2, slot type A in Fig. 8.1(a) results to be closed, while slot type B are open. On the contrary, all the rotor slots of prototype 3 are closed.

A higher leakage flux and hence higher leakage inductance is expected due to these semi-closed rotor slots. In particular, prototype 3 is expected to have a higher mean impedance due to all closed rotor slots. In order to investigate more in detail the leakage flux lines distribution in case of closed rotor slot, FE simulations have been considered. The rotor slots has been closed with a proper iron bridge. The simulations presented in Subsection 8.4.1 consider an iron bridge width $w_b = 0.2\ mm$ over all slots characterized by a slot opening width $w_{so} < 1\ mm$. Linear iron is used for the lamination and saturated iron for the iron bridges [26, 73] to simulate the actual behavior under load condition. As an example, Fig. 8.4 shows the HF leakage fluxes of prototype 3, in which each slot is closed by the iron bridge. It is worth noticing how fluxes mainly flow toward the iron bridges. The variation of the terminal impedance with rotor position is expected to be higher for prototype 2 which has closed and open rotor slots. This combination of open and closed rotor slot adds an unpredicted variation of the HF rotor saliency. In addition, the presence of closed rotor slots leads to an undesired field-dependent variation of the local inductance [111].

When rotor slot openings are properly designed, the serial production will not presents any particular difficulties. In open-slot configurations, the slight difference between rotors in serial production will not affect significantly the rotor parameters.

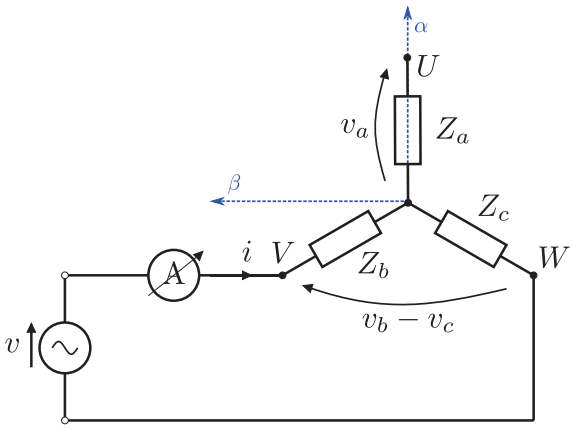

Figure 8.5: Electrical connection, pulsating field along β axis

8.4. Measurements vs simulations

8.4.1. Self-impedance $\dot{z}_{\beta\beta}$

At first, a HF signal is injected in stator winding by means of a function generator and a signal amplifier. A sinusoidal voltage at the frequency of $f = 300\ Hz$ is considered. The common injection frequency in actual sensorless drives is usually in the range 200 to $1000Hz$. However, the modulation amplitude remains quite frequency-invariant below $5kHz$ [110].

The motor has been supplied so as to obtain a pulsating magnetic field at the desired frequency f along the $\beta-$axis. Fig. 8.5 shows the electrical connection adopted for this test. The same test could be performed imposing a pulsating field along the $\alpha-$axis, but an unequal current distribution in b and c windings occurs if they are not exactly equal. The stator voltages in the stationary reference frame are computed as

$$\begin{cases} \overline{U}_{s\alpha} = \overline{v}_a \\ \overline{U}_{s\beta} = \dfrac{1}{\sqrt{3}} (\overline{v}_b - \overline{v}_c) \end{cases} \tag{8.3}$$

while the β current is computed as

$$\overline{I}_{s\beta} = \frac{2}{\sqrt{3}} \cdot \overline{i} \tag{8.4}$$

where $\overline{i}$ is the measured current of the circuit in Fig. 8.5. The terminal impedance $\dot{z}_{\beta\beta}$ and the mutual term $\dot{z}_{\beta\alpha}$ is computed as in (8.2). The impedance $\dot{z}_{\alpha\alpha}$ is not reported in the analysis since it exhibits the same trend of $\dot{z}_{\beta\beta}$. In particular, $\dot{z}_{\alpha\alpha}$ is minimum when $\dot{z}_{\beta\beta}$ is maximum, that is, it exhibits a shift of 45 mechanical degrees.

The impedance modulation due to the slots depends on the stator and rotor slot number combination and it is reduced by the skewing of rotor bars. Fig. 8.6 shows the terminal impedance of prototype 1 corresponding to two values of skewing angle. The case without skewing is also reported in Fig. 8.6 for clarity. It is worth noticing how the rotor skewing reduces the impedance fluctuation due to the slots.

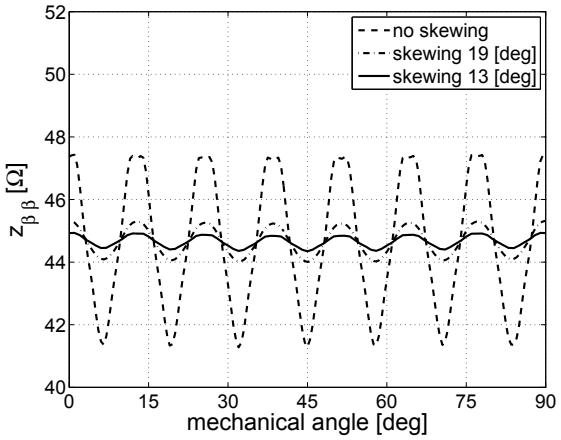

Figure 8.6: Terminal impedance, prototype 1: with and without skewing (FE results). A $f = 300Hz$ signal is imposed along the β axis

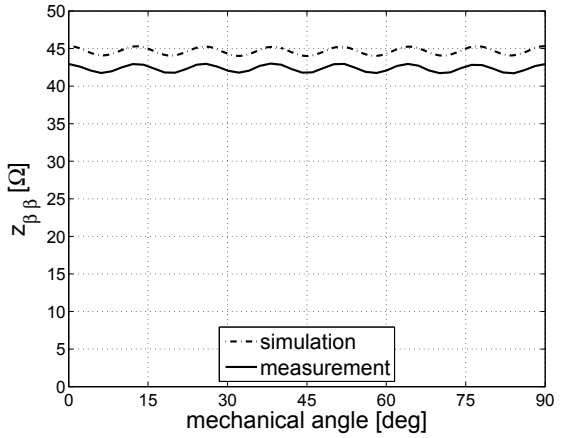

Figure 8.7: Terminal impedance, prototype 1 when a $f = 300Hz$ signal is imposed along β axis

The experimental measurement of the terminal impedance has been carried out on the three prototypes under study. The results are shown hereafter as a function of mechanical position, together with the result of FE analysis.

Fig. 8.7 shows how the measured trend of terminal impedance impedance $\dot{z}_{\beta\beta}$ on prototype 1 fits the simulated one. In particular, the mean value of $\dot{z}_{\beta\beta}$ achieved by the FE analysis is very close to the measured one, while the variation of $\dot{z}_{\beta\beta}$ with rotor position due to the slots has the same amplitude, i.e. about 3% of the mean value, in both cases.

Regarding prototype 2, the average value of impedance $\dot{z}_{\beta\beta}$ is higher than those of standard motor as shown in Fig. 8.8. The same figure shows also a high dependence of $\dot{z}_{\beta\beta}$ on rotor position with respect to that of prototype 1. This is expected since the difference between the maximum and minimum value of $\dot{z}_{\beta\beta}$ is very high. Such a dependence does not depend on the skewing angle. The amplitude of the variation of $\dot{z}_{\beta\beta}$ is about 2/3 of the average value, both for simulation and measurement. On the contrary, simulation underestimates the average value of terminal impedance. This

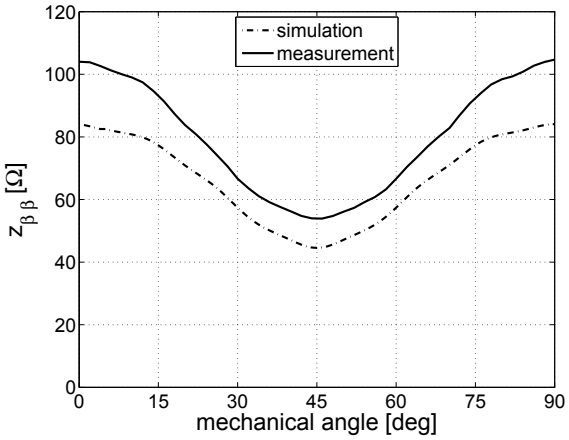

Figure 8.8: Terminal impedance, prototype 2 when a $f = 300Hz$ signal is imposed along the β axis

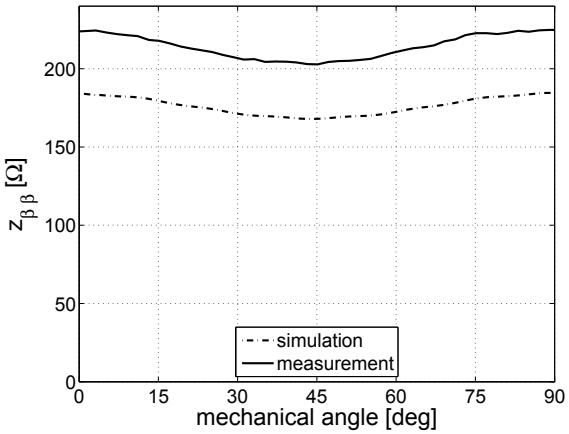

Figure 8.9: Terminal impedance, prototype 3 when a $f = 300Hz$ signal is imposed along the β axis

difference in the average value is due to the uncertainty of the actual thickness of the iron bridges above the slot openings. As said in Subsection 8.3.1, only the slots with slot opening width $w_{so} < 1mm$ have been considered to be closed in the simulations. However, there is not a clear distinction between the actual closed and opened slots in the prototype 2. As shown in Fig. 8.10, some slots result open only for a fraction of the total stack length. Due to the iron bridges, a higher leakage reactance is expected in prototype 3. As a consequence, a higher $\dot{z}_{\beta\beta}$ is expected. This is confirmed in Fig. 8.9, where the difference between the maximum and minimum value of $\dot{z}_{\beta\beta}$ is about 10% of its mean value for both simulation and measurement, that is lower than that of prototype 2. Also in this case FE analysis underestimates the average value of the terminal impedance. From FE analysis, the terminal impedance results to be very sensitive to the thickness of the iron bridges above the slot openings [120].

Figure 8.10: Partial lathing of prototype 2

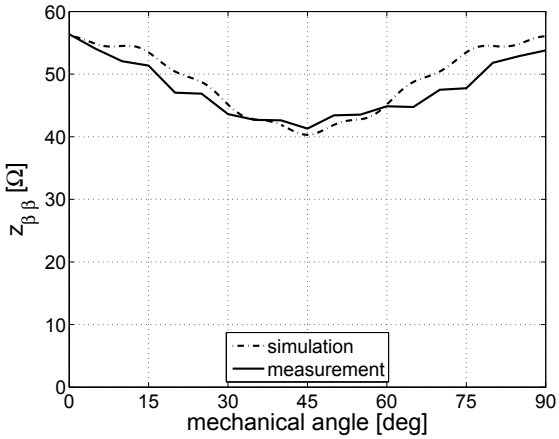

Figure 8.11: Terminal impedance, prototype 2 machined when stator winding is supplied at $f = 300Hz$ along the β axis

8.4.2. Self-impedance $\dot{z}_{\beta\beta}$ on Prototype 2 with opened rotor slots

To remove the field-dependent component on the leakage inductance, the rotor of prototype 2 has been machined again. The rotor slot iron bridges, shown in Fig. 8.10, have been removed so that the aluminum bars becomes visible. Then, the test has been repeated again. A $f = 300\ Hz$ signal has been injected along the β axis. Fig. 8.11 reports the measured terminal impedance as a function of rotor position. By opening the slot of prototype 2, the measured average impedance decreases. Due to the absence of iron bridges over the slots, it can be noted from Fig. 8.11 that FE analysis predict satisfactorily the trend of $\dot{z}_{\beta\beta}$ as a function of the rotor position.

To investigate the magnetizing flux effects on the modulation amplitude, a DC current was superimposed to a $f = 200\ Hz$ HF signal. The measured reduction of the average impedance due to increasing flux level is shown in Fig. 8.12. In the case of $2A$ DC, that corresponds to the magnetizing current (60% of the rated current), the average impedance decrease of the 6%, while the impedance variation decrease less than 1%. As a result, the spatial dependance of the terminal impedance is maintained also in presence of the load, that is, the self-sensing capability.

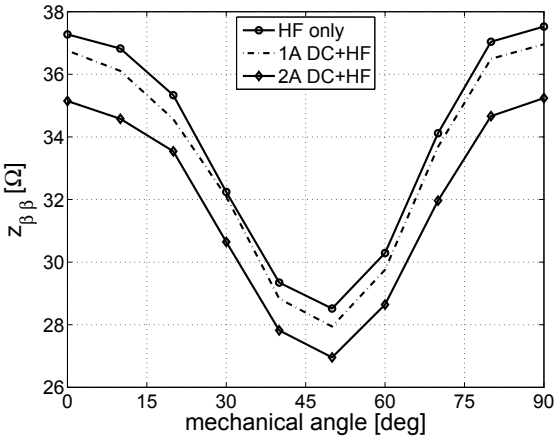

Figure 8.12: Measured terminal impedance, prototype 2 machined when a DC signal is superimposed to an HF signal of $f = 200Hz$ along the β axis

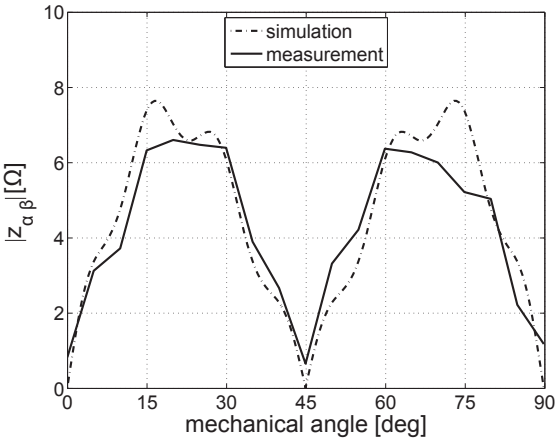

Figure 8.13: Mutual impedance, prototype 2 machined when stator winding is supplied at $f = 300Hz$ along the β axis

8.4.3. Mutual-impedance $\dot{z}_{\alpha\beta}$

An estimation of the mutual impedance existing between the α–β axis has been computed using (8.2). Fig. 8.13 reports the measured and simulated absolute value of the mutual leakage reactance $\dot{z}_{\alpha\beta}$ of prototype 2 machined. Good agreement is found between simulation and measurement results. As mentioned in Section 8.2, the mutual impedance depends on the amplitude of the leakage inductance variation with the rotor position. The consequence is that in prototype 1 (i.e. with standard rotor) the mutual impedance is rather small and comparable to the sensitivity of the instrumental apparatus as shown in Fig. 8.14. The mutual impedance measured on the prototype 3 and prototype 2 before being machined are shown in Fig. 8.15. The results of simulations are not reported due to the uncertainty of the iron bridge width. It is convenient to observe that the mutual impedance of prototype 2 un-machined is very high compared to that of prototype 3.

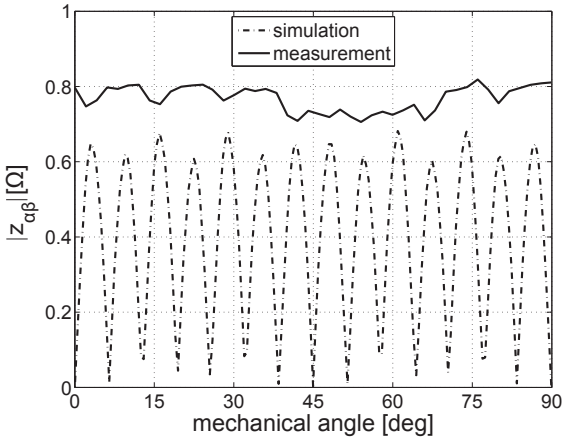

Figure 8.14: Mutual impedance, prototype 1 when stator winding is supplied at $f = 300Hz$ along the β axis

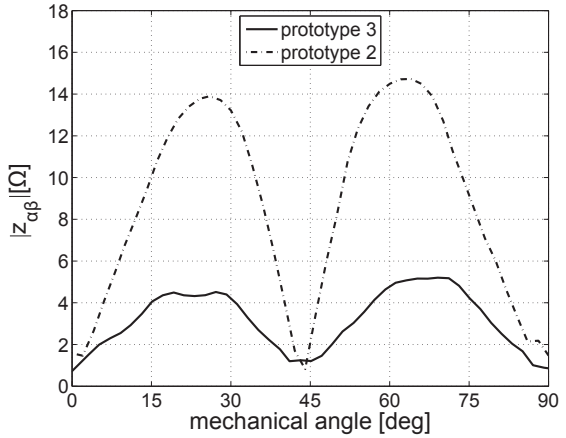

Figure 8.15: Measured mutual impedance, prototype 2 (un-machined) and 3 when stator winding is supplied at $f = 300Hz$ along the β axis

8.4.4. Test at rated current

A test has been carried out to understand how the introduced saliency affects the performance of the prototypes. The greater the reactance of the cage, the higher the reactive power, the lower the power factor of the motor. On the other hand, the efficiency should decrease less than the power factor, since it is mostly related to the resistive part of the cage. The prototypes have been mounted on a test bench in which a master motor is used to reproduce the effect of the load. The master motor is an IM that can be operated in speed control mode. A steady state test has been carried out at rated current. The load has been regulated so as the current absorbed by the motor was the same for the three prototypes. The steady-state test was carried out at thermal steady-state, that is, when there is not appreciable variation of the stator temperature. Table 8.1 shows electrical quantities measured on the three prototypes.

The variation in electrical quantities for prototype 2 and 3 with respect to those of standard motor is reported in Table 8.2. As expected, the introduced anisotropy of

Table 8.1: Prototype comparison at rated current

Parameter	Prototype 1	Prototype 2	Prototype 3
I [A]	3.62	3.63	3.61
V [V]	396.9	398.1	394.4
P [W]	1869	1733	1703
PF [-]	0.75	0.69	0.69
slip [%]	3.00	2.80	3.40
Torque [Nm]	10.7	9.8	9.7
η [%]	87.0	86.3	86.3

Table 8.2: Performance variation with respect to prototype 1: Test at rated current

Parameter	Prototype 2	Prototype 3
Power factor	-8 %	-8 %
Torque	-8 %	-9 %
Mechanical power	-8 %	-10 %
Efficiency	-0.8 %	-0.8 %

the rotor bars does not reduce significantly the motor efficiency. A higher decrease is noticed for output torque, mechanical power and power factor. During the test it has been noticed that prototype 2 is a little bit noisier than prototype 1 and 3, remaining within acceptable limits.

It should be noted that sensorless drives operate not only at low slip values, but also in various dynamic states. Starting and maximum torque are important and for this reason their deterioration has been quantified in the next Section.

8.4.5. Steady state characteristic

A test has been carried out to measure the (quasi)–steady state mechanical characteristic of the three prototypes. The motors are supplied with the line voltage and they are forced to increase their speed by the master motor following a ramp path. The total starting time is 5 s. Since the speed variation is slower than the variation of electrical quantities, it is possible to consider the measured mechanical characteristic as (quasi)–steady-state. The measured torque is shown in Fig. 8.16 for the three prototypes. From Fig. 8.16 it is possible to see how the introduced rotor anisotropy reduces the starting torque (at $s = 1$) as a consequence of the increased leakage reactance. Furthermore, as expected, the maximum torque of the prototype 3 is lower than that of the other two prototypes because of the higher value of average impedance. However, since an IM drive works at low slip, where the mechanical characteristic is very steep, the reported reduction of the starting and maximum torque has a low impact in the rated value, as shown in Table 8.1.

Hereafter, Table 8.3 lists the motor parameter of the two prototypes obtained by

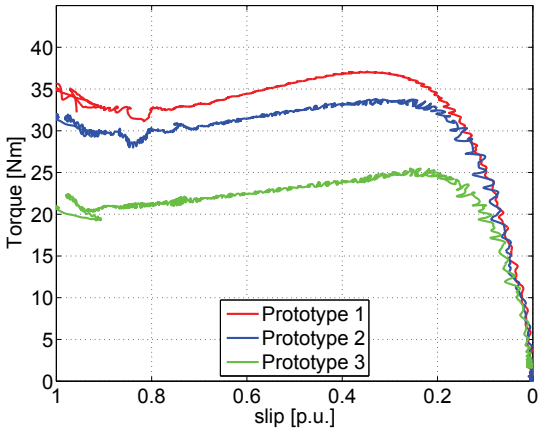

Figure 8.16: Torque characteristic

classical no-load and locked rotor tests. The parameters refer to the IM Γ-type equivalent circuit. If a rotor anisotropy is introduced, as for prototypes 2 and 3, such a parameters have to be considered as a mean between the $\alpha-$ and $\beta-$ axis parameters [60]. Table 8.3 highlights that the rotor parameters of the prototype 3 result to be higher than those of the other prototypes.

Table 8.3: Parameters for the three prototypes measured at 50 Hz

Parameter	Prototype 1	Prototype 2	Prototype 3
R_s [Ω]	3.5	3.5	3.5
X_0 [Ω]	107	100	104
R_0 [$k\Omega$]	2.1	2.5	2.6
R_r [Ω]	3.1	3.7	6.2
X_σ [Ω]	8.80	10.5	20.0

8.5. Conclusions

It is known that the injection of a carrier signal to the fundamental excitation of an IM with created saliency in rotor slot openings allows the detection of rotor position and rotor speed as well. The rotor anisotropy can be achieved by varying both the slot opening height and width along the airgap.

Three prototypes have been manufactured: two of them with created saliency and the third is a standard induction motor used as reference. The experimental realization of the prototypes shows that the rotor saliency can be affected by the casting and milling processes. In particular, a too narrow rotor slot opening can lead to an unwanted iron bridge that closes the slot, causing an unpredictable variation of IM parameters.

This Chapter experimentally quantifies the impact of the rotor slot modification as concerns the terminal impedance variation, the reduction of starting and maximum torque and the steady state performance deterioration. A high dependency of terminal

impedance on rotor position is achieved. It is confirmed that the main flux does not affect significantly the variation of the terminal impedance with the rotor position. It is shown that the reduction of starting and maximum torque can be significant, especially when rotor slots are not completely open. On the other hand, the motor efficiency at steady state results slightly reduced. A higher decrease is measured as regard output torque, mechanical power and power factor.

FE time harmonic simulations are used to estimate the rotor anisotropy necessary to the detection of rotor position. Simulations predict properly the HF response of the prototypes in case of open rotor slots.

Chapter 9

On the Proprieties of the Differential Cross-Saturation Inductance in Synchronous Machines

The cross-saturation inductance is a mutual inductance due to the saturation of portions of the magnetic circuit of one axis caused by the current of the other axis. In sensorless drives, the differential cross-saturation inductance causes an error in the estimation of the rotor position when it is performed by means of the high frequency signal injection methods. The knowledge of the properties of cross-saturation inductance is therefore essential to minimize any distortion effect on the position estimation. This Chapter aims to describe the properties of the cross-saturation inductance for different types of synchronous machine, such as reluctance, interior permanent-magnet and surface-mounted permanent-magnet machines. Information is also given to predict the error in the estimated position for any stator currents, useful for implementing an error compensation technique or to detect the feasible operating regions using the high frequency voltage injection technique. The analysis is supported by finite element simulations and experimental measurements.

9.1. Introduction

The cross-saturation inductance $l_{dq} = l_{dq}(i_d, i_q)$ is a differential mutual inductance that describes the existing coupling between spatially orthogonal d– and q–axis windings of a three phase synchronous machine (SyM) [121]. It is due to the saturation of magnetic circuit portions of one-axis caused by the current of the other axis. Any rigorous model of a SyM should consider iron saturation and, therefore, it should include the cross-saturation inductance. The effect of l_{dq} could not be ignored in any model-based control algorithm such as in the application of Model Predictive Control, in the identification of electromechanical quantities and in the sensorless detection of rotor position by high frequency (HF) voltage injection techniques.

As an example, when HF voltage injection technique is adopted in sensorless drive, the cross-saturation differential inductance l_{dq} causes an error in the estimation of the

rotor position. When the motor is operating at steady state in a generic I_d–I_q working point, the HF current trajectory is an ellipse if a rotating HF voltage in injected [122]. The major axis of the ellipse which identifies the estimated d-axis is rotated by the angle ϵ with respect to the actual d-axis, with

$$\epsilon = \frac{1}{2} \arctan\left(-\frac{l_{dq}}{l_{\Delta}}\right) \tag{9.1}$$

where the difference inductance $l_{\Delta} = (l_q - l_d)/2$ [123]. The same result is valid for pulsating HF voltage injection. As evident from (9.1), the sensorless control is not effective when l_{dq} is high causing a huge rotor position estimation error [124].

All the inductances are functions of the stator currents in the considered operating point. As regard the control algorithm, the knowledge of the properties of the differential cross-saturation inductance, that is, sign and amplitude depending on the working condition, is therefore essential:

- to envisage the thread of any model-based identification or control algorithm [125–129];
- to estimate the effects in neglecting the presence of cross-saturation [123,130–132];
- to design any compensation approach to mitigate the negative effects of the cross-saturation, that are undesired in the developed application [133–137];
- to detect the polarity of the direct axis at locked rotor [138];

As far as the machine is concerned, ideally the locus $l_{dq} = 0$ should be as close as possible to the maximum torque per ampere (MTPA) trajectory to avoid the aforementioned estimation error ϵ. The effect of the stator and rotor iron saturation of a three-flux barriers interior permanent magnet (IPM) motor on the estimation accuracy is investigated in [139]. In [140], the effect of some rotor and stator modifications of Permanent Magnet (PM) machine on l_{dq} has been studied. A stator with lower iron saturation yields a lower angle error (proportional to l_{dq}), as expected. The estimation error angle may be very high and instabilities in the control may occur, highlighting the importance to consider l_{dq} in the control algorithm. The knowledge of the l_{dq} properties is therefore essential. However, only partial results are achieved in the aforementioned works and a general analysis of the l_{dq} trend has not been carried out yet.

This work aim is to describe the properties of the cross-saturation inductance for SyMs, supporting the analysis by means of finite element (FE) simulations and experimental measurements. For the sake of generality, different SyMs are considered. They are reluctance (REL), IPM and surface-mounted permanent-magnet (SPM) machine. The first part of the Chapter is dedicated to describe the properties of l_{dq} from the theoretical point of view. A simplified magnetic model is introduced to roughly predict the position of the locus $l_{dq} = 0$, determining consequently the sign of l_{dq} in the i_d–i_q plane. After that, the second part of the Chapter validates the analysis by comparing FE results with those from experiments.

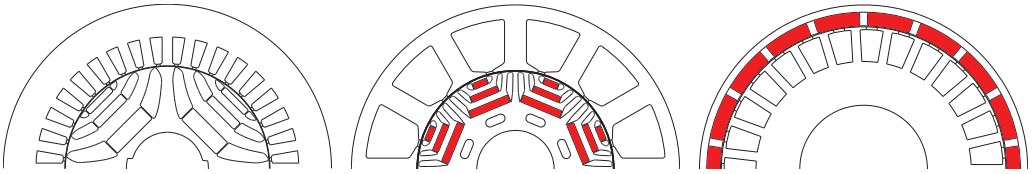

(a) REL machine lamination (b) IPM machine lamination (c) SPM machine lamination

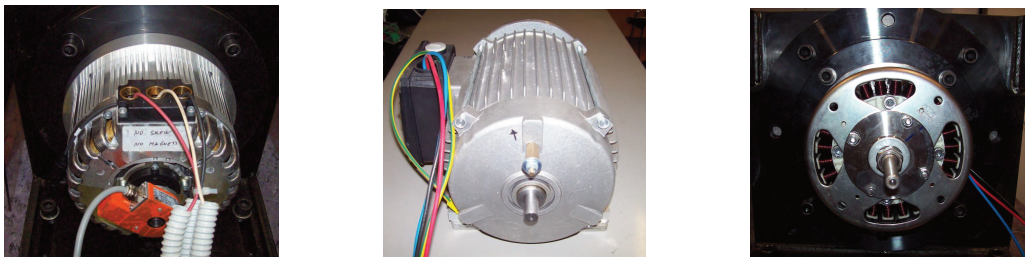

(d) REL machine prototype (e) IPM machine prototype (f) SPM machine prototype

Figure 9.1: SyM laminations and rotor prototypes used in the analysis of differential cross-saturation inductance

9.2. Considered motor structures

The analysis of the differential cross-saturation inductance is carried out on three types of SyMs. They are an REL, an IPM and an SPM machines, whose main data are reported in Table 9.1.

REL machine: It is a 36–slot 4–pole, 15 Nm machine and it is illustrated in Fig. 9.1(a). Its airgap diameter is $D_i = 125\ mm$ and the stack length is $L_{stk} = 40\ mm$. A photo of the prototype is in Fig. 9.1(d).

IPM machine: It is a 12 Nm, 12–slot 8–pole machine, whose lamination is sketched in Fig. 9.1(b). Its airgap diameter is $D_i = 84\ mm$ and the stack length is $L_{stk} = 75\ mm$. The prototype is shown in Fig. 9.1(e).

SPM machine: It is a 10 Nm, 27–slot 18–pole machine, illustrated in Fig. 9.1(c). It is an external rotor machine, whose airgap diameter is $D_i = 156\ mm$ and the stack length is $L_{stk} = 35\ mm$. The prototype is shown in Fig. 9.1(f). These SyMs are chosen to demonstrate that the analysis proposed in this Chapter is reasonably valid for any

Table 9.1: Main data of the considered machines

machine	winding	airgap diameter D_i $[mm]$	rated power P $[kW]$	rated current I $[A]$	length L_{stk} $[mm]$
REL	36/4	125	2	6	40
IPM	12/08	84	2.5	12	75
SPM	27/6	156	3	10	35

SyM. In fact, they exhibit characteristics that are common in all SyM:

- Flux barriers;
- PM in a rotor structure with or without saliency;
- Distributed and fractional slot winding.

Inductance l_{dq} is affected by saturation and it vary considerably depending on design variables such as tooth, back iron and flux barrier width. However, general considerations valid for any SyM will be deduced from the following analysis.

9.3. Machine equations

Referring to a generic SyM in which PM, if present, is aligned along the d– axis, the d– and q–axis flux linkages can be expressed as a function of the stator currents as

$$\begin{cases} \lambda_d = \lambda_d(i_d, i_q) \\ \lambda_q = \lambda_q(i_d, i_q) \end{cases} \tag{9.2}$$

Considering a non-hysteretic loss-less system, there is a biunivocal relationship between the currents and the flux-linkages. The voltage equations are expressed as

$$\begin{cases} v_d = R_s i_d + \dfrac{d\lambda_d(i_d, i_q)}{dt} - \omega_m^e \lambda_q(i_d, i_q) \\ v_q = R_s i_q + \dfrac{d\lambda_q(i_d, i_q)}{dt} + \omega_m^e \lambda_d(i_d, i_q) \end{cases} \tag{9.3}$$

Rearranging the time derivatives and assuming a zero speed, i.e. $\omega_m^e = 0$, equations (9.3) can be written as

$$\begin{cases} v_d = R_s i_d + l_d(i_d, i_q)\dfrac{di_d}{dt} + l_{dq}(i_d, i_q)\dfrac{di_q}{dt} \\ v_q = R_s i_q + l_{qd}(i_d, i_q)\dfrac{di_d}{dt} + l_q(i_d, i_q)\dfrac{di_q}{dt} \end{cases} \tag{9.4}$$

where the differential inductances are defined as

$$\begin{aligned} l_d &= \frac{\partial \lambda_d(i_d, i_q)}{\partial i_d} & l_{dq} &= \frac{\partial \lambda_d(i_d, i_q)}{\partial i_q} \\ l_{qd} &= \frac{\partial \lambda_q(i_d, i_q)}{\partial i_d} & l_q &= \frac{\partial \lambda_q(i_d, i_q)}{\partial i_q} \end{aligned} \tag{9.5}$$

9.4. Proprieties of cross-saturation inductance

Independently from the rotor structure presented in Section 9.2, the cross-saturation inductance holds some general properties, which derive from general laws of the electromagnetic field theory and geometrical symmetries of the rotor lamination. Hereafter such properties are recalled, justified and discussed.
Dependance of fluxes, inductances, energy on machine currents is not explicitly written if not essential for the treatment.

9.4.1. Reciprocity theorem

The energy conservation principle yields the equality of the differential cross-saturation inductances defined in (9.5), [141]. At locked rotor, the electric work due to infinitesimal linkage flux variations is given by

$$\begin{aligned} dW &= \frac{3}{2}\left(i_d d\lambda_d + i_q d\lambda_q\right) = \\ &= \frac{3}{2}\left[i_d\left(\frac{\partial\lambda_d}{\partial i_d}di_d + \frac{\partial\lambda_d}{\partial i_q}di_q\right) + i_q\left(\frac{\partial\lambda_q}{\partial i_d}di_d + \frac{\partial\lambda_q}{\partial i_q}di_q\right)\right] \end{aligned} \tag{9.6}$$

and it equals the magnetic energy variation. The magnetic energy is a state function of the currents $W = W(i_d, i_q)$ and the currents i_d, i_q are state variables. Then, one obtains

$$dW = \frac{\partial W(i_d, i_q)}{\partial i_d}di_d + \frac{\partial W(i_d, i_q)}{\partial i_q}di_q \tag{9.7}$$

Comparing equations (9.6) and (9.7), it results

$$\begin{cases} \dfrac{\partial W}{\partial i_d} = \dfrac{3}{2}\left(i_d\dfrac{\partial\lambda_d}{\partial i_d} + i_q\dfrac{\partial\lambda_q}{\partial i_d}\right) \\ \dfrac{\partial W}{\partial i_q} = \dfrac{3}{2}\left(i_d\dfrac{\partial\lambda_d}{\partial i_q} + i_q\dfrac{\partial\lambda_q}{\partial i_q}\right) \end{cases} \tag{9.8}$$

and the two second mixed derivatives are expressed as

$$\begin{cases} \dfrac{\partial^2 W}{\partial i_d\partial i_q} = \dfrac{3}{2}\left(i_d\dfrac{\partial^2\lambda_d}{\partial i_d\partial i_q} + \dfrac{\partial\lambda_q}{\partial i_d} + i_q\dfrac{\partial^2\lambda_q}{\partial i_d\partial i_q}\right) \\ \dfrac{\partial^2 W}{\partial i_q\partial i_d} = \dfrac{3}{2}\left(\dfrac{\partial\lambda_d}{\partial i_q} + i_d\dfrac{\partial^2\lambda_d}{\partial i_q\partial i_d} + i_q\dfrac{\partial^2\lambda_q}{\partial i_q\partial i_d}\right) \end{cases} \tag{9.9}$$

Schwarz's theorem for two-variable functions yields

$$\frac{\partial^2 W}{\partial i_d\partial i_q} = \frac{\partial^2 W}{\partial i_q\partial i_d} \tag{9.10}$$

so that, introducing (9.9) in (9.10), and simplifying equal terms on the two sides, the reciprocity property is proved, see also (9.5), that is

$$l_{dq}(i_d, i_q) = l_{qd}(i_d, i_q) \tag{9.11}$$

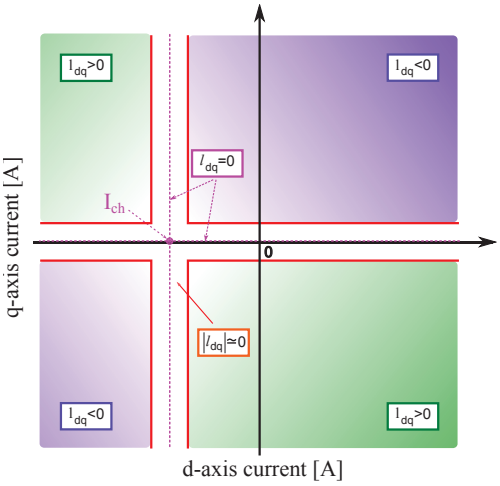

Figure 9.2: Trend of l_{dq} in the i_d–i_q plane for a generic SyM machine. Generic boundaries are in the d– and q-axis currents

9.4.2. Axis orthogonality property

The PM flux (if any) is considered to be aligned along the d–axis. Remembering that the d– and q–axis are orthogonal, it is

$$\begin{cases} \lambda_d(i_d, i_q) = \lambda_d(i_d, -i_q) \\ \lambda_q(i_d, i_q) = -\lambda_q(i_d, -i_q) \end{cases} \tag{9.12}$$

From the first equation in (9.12), one obtains

$$\frac{\partial \lambda_d(i_d, i_q)}{\partial i_q} = \frac{\partial \lambda_d(i_d, -i_q)}{\partial i_q} = -\frac{\partial \lambda_d(i_d, -i_q)}{\partial(-i_q)} \tag{9.13}$$

and then

$$l_{dq}(i_d, i_q) = -l_{dq}(i_d, -i_q) \tag{9.14}$$

The second equation of (9.12) confirms this property again. In fact, by derivation of both sides, it is possible to write

$$\frac{\partial \lambda_q(i_d, i_q)}{\partial i_d} = -\frac{\partial \lambda_q(i_d, -i_q)}{\partial i_d} \tag{9.15}$$

which coincides to (9.14).

9.4.3. Zero of l_{dq} along the d–axis

This statement is a particular case of the property illustrated above when $i_q = 0$. Namely, it should be realized that

$$l_{dq}(i_d, 0) = 0 \tag{9.16}$$

is a limit solution of (9.14). This property states that the real axis of the i_d–i_q plane belongs to the $l_{dq} = 0$ locus, as illustrates in the exemplifying Fig. 9.2. Rather than

the straight line where $l_{dq} = 0$, Fig. 9.2 shows a region of the i_d–i_q plane where l_{dq} is very close to zero. This is a more practical approach to determine the zero of such a parameter, yielding a more suitable comparison with the experimental results which will be illustrated later on.

9.4.4. Zero of l_{dq} along $i_d = I_{ch}$ locus

From a simplified magnetic analysis, the d–axis flux linkage can be defined as

$$\lambda_d(i_d, i_q) = N\frac{Ni_d + H_m t_m}{\Re_d(i_d, i_q)} \tag{9.17}$$

where the numerator is the magnetomotive force along the d–axis (H_m and t_m are the PM coercitive magnetic field and thickness, respectively), $\Re_d(i_d, i_q)$ is the d–axis reluctance which is assumed to be dependent on both the machine currents due to saturation effects and N is the phase effective number of turns. From (9.17), the cross-saturation inductance is computed as

$$l_{dq} = \frac{\partial \lambda_d}{\partial i_q} = N\frac{(Ni_d + H_m t_m)}{\Re_d^2(i_d, i_q)}\frac{-\partial \Re_d(i_d, i_q)}{\partial i_q} \tag{9.18}$$

Eq. (9.18) states that $l_{dq} = 0$ where:

- $\partial \Re_d(i_d, i_q)/\partial i_q \equiv 0$, that is, where there is not cross saturation. This region of the i_d-i_q plane is not known a priori, as it is function of the geometrical parameters of the machine. Generally speaking, for low λ_d and/or λ_q fluxes the magnetic circuit is linear and $l_{dq} \simeq 0$;
- $(Ni_d + H_m t_m) = 0$, that is, when $\lambda_d = 0$, which is ideally a vertical line in the i_d-i_q plane at $i_d = -(H_m t_m)/N$, which can be also rewritten as $i_d = -\lambda_m/L_d$, where L_d is the unsaturated d–axis inductance. Such a current is often referred to a characteristic current I_{ch} and it is approximately constant for any i_q in PM motors.

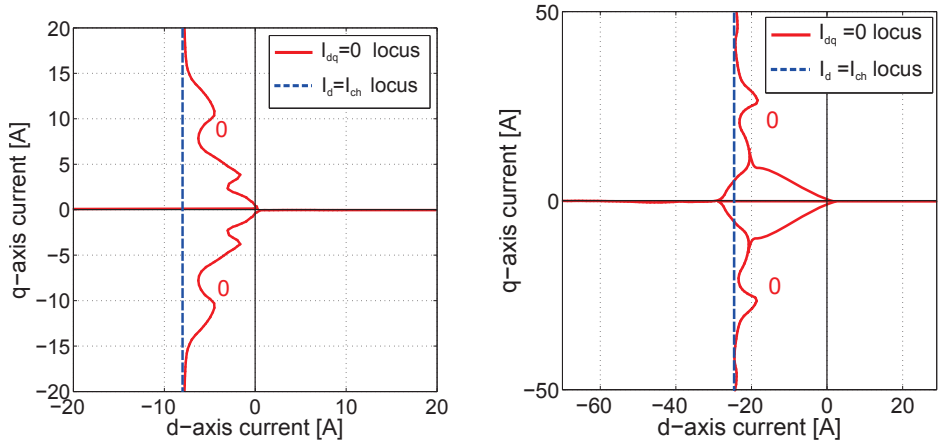

(a) IPM machine

(b) SPM machine

Figure 9.3: $i_d = I_{ch}$ and $l_{dq} = 0$ loci (FE simulations)

The expected $l_{dq} = 0$ locus and the region $\mid l_{dq} \mid \simeq 0$ are therefore not only along the d–axis and where no iron saturation occurs, but also along the straight line characterized by $i_d = -\Lambda_m/L_d$ as sketched in Fig. 9.2. As a confirmation, Fig. 9.3 shows the locus $i_d = I_{ch}$ together with the locus $l_{dq} = 0$ for the IPM and SPM machine as they result from the FE analysis that will be described later.

The sign of l_{dq} in the four quadrants of the i_d–i_q plane defined by the locus $l_{dq} = 0$ can be predicted by (9.18). It is reasonable to assume that the reluctance increases with the saturation and then when the amplitude of the current increases. Then, $\partial \Re_d / \partial i_q > 0$ for $i_q > 0$ and vice-versa, so that the sign of l_{dq} results as shown in Fig. 9.2: $l_{dq} < 0$ in the first and third quadrants of the i_d–i_q plane and $l_{dq} > 0$ in the second and fourth quadrants.

The REL machine can be considered as a particular PM machine in which $I_{ch} = 0$ and then $l_{dq} = 0$ locus coincide with the i_d– and i_q–axis. This can be demonstrated also in a different way. For the REL machine, it results

$$\begin{cases} \lambda_d(i_d, i_q) = -\lambda_d(-i_d, i_q) \\ \lambda_q(i_d, i_q) = \lambda_q(-i_d, i_q) \end{cases} \tag{9.19}$$

and, by derivation of both sides of the first equation in (9.19),

$$l_{dq}(i_d, i_q) = \frac{\partial \lambda_d(i_d, i_q)}{\partial i_q} = -\frac{\partial \lambda_d(-i_d, i_q)}{\partial (i_q)} = -l_{dq}(-i_d, i_q) \tag{9.20}$$

Therefore it is possible to write:

- $l_{dq}(i_d, 0) = 0$ directly from (9.16);
- $l_{dq}(0, i_q) = 0$ from (9.20).

It follows that both the $i_d = 0$ and $i_q = 0$ axes represent the $l_{dq} = 0$ locus, as illustrated in Fig. 9.2 with $I_{ch} = 0$.

9.5. FE analysis

In order to confirm the theoretical predictions of the previous section, a FE analysis of the machines shown in Fig. 9.1 has been carried out. A series of magnetostatic simulations have been performed in the whole i_d–i_q plane. Fig. 9.4 shows the flux lines when only d– or q–axis currents are flowing in the stator winding.

From the field solution, the differential inductances have been computed in each point of the i_d–i_q plane as

$$\begin{aligned} l_d(i_d, i_q) &= \frac{\lambda_d(i_d + \Delta i_d, i_q) - \lambda_d(i_d - \Delta i_d, i_q)}{2\Delta i_d} \\ l_{dq}(i_d, i_q) &= \frac{\lambda_d(i_d, i_q + \Delta i_q) - \lambda_d(i_d, i_q - \Delta i_q)}{2\Delta i_q} \\ l_q(i_d, i_q) &= \frac{\lambda_q(i_d, i_q + \Delta i_q) - \lambda_q(i_d, i_q - \Delta i_q)}{2\Delta i_q} \\ l_{qd}(i_d, i_q) &= \frac{\lambda_q(i_d + \Delta i_d, i_q) - \lambda_q(i_d - \Delta i_d, i_q)}{2\Delta i_d} \end{aligned} \tag{9.21}$$

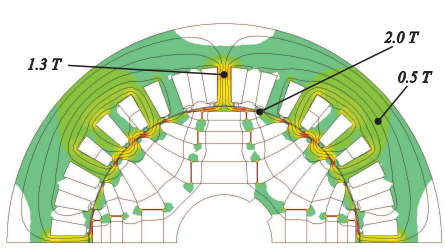

(a) REL machine, d–axis current

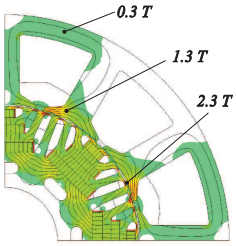

(b) IPM machine, d-axis current

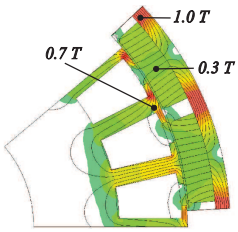

(c) SPM machine, d-axis current

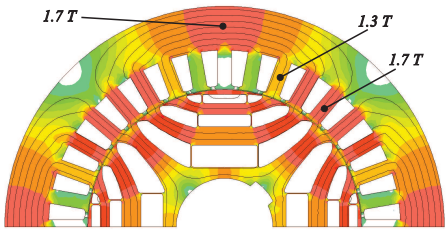

(d) REL machine, q–axis current

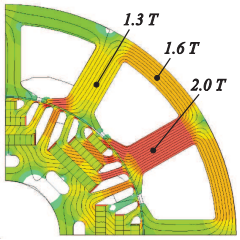

(e) IPM machine, q-axis current

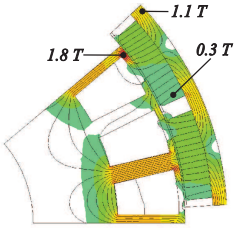

(f) SPM machine, q-axis current

Figure 9.4: Flux lines and flux density map of the prototypes

The l_{dq} loci achieved with FE is shown in Fig. 9.5. Instead of a single curve, a region

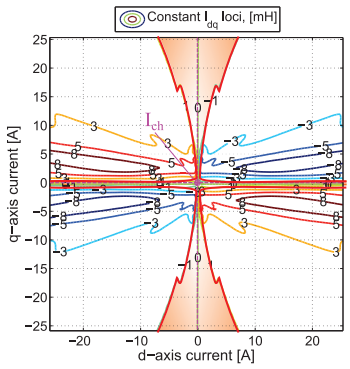

(a) REL machine

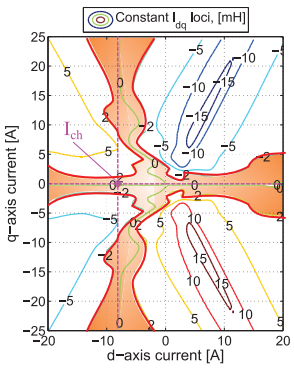

(b) IPM machine

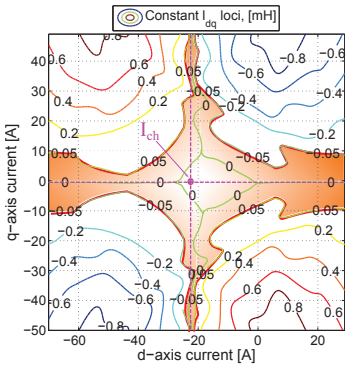

(c) SPM machine

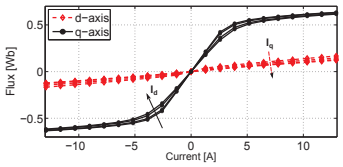

(d) REL machine: current vs flux

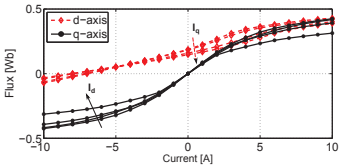

(e) IPM machine: current vs flux

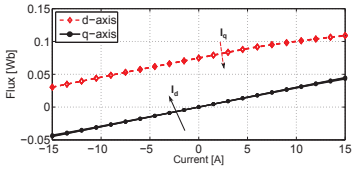

(f) SPM machine: current vs flux

Figure 9.5: l_{dq} loci in the i_d-i_q plane (FE simulation) and current vs flux characteristics

around $l_{dq} = 0$ has been highlighted in Fig. 9.5. It is worth noticing that the trend of l_{dq} is in agreement with the theoretical considerations of the previous Section. For all the considered machines $l_{dq} \simeq 0$ i) where the iron saturation is low, that is, for

low i_d– and i_q–current, ii) along $i_q = 0$ and iii) along $i_d = I_{ch}$. The current vs flux characteristics considering the cross saturation effect are also shown in Fig. 9.5. These figures illustrate how the flux of one axis is affected by the current of the other axis. Further comments on Fig. 9.5 will be found in the following Subsections.

The following parameters, that are function of the differential inductances l_d, l_q and l_{dq}, can be achieved from experimental measurements, as pointed out in Section 9.6:

$$\begin{aligned} \Gamma_{dq} &= \frac{l_{dq}}{l_d l_q - l_{dq}^2} \left[\frac{1}{H}\right] \\ \Gamma_{\Delta} &= \frac{l_{\Delta}}{l_d l_q - l_{dq}^2} \left[\frac{1}{H}\right] \end{aligned} \tag{9.22}$$

Their unit of measurement is the reciprocal of an inductance one, that is, H^{-1}. Such parameters are chosen to be compared with the results of FE, as they are proportional to l_{dq} and l_{Δ}, respectively.

Even if the analysis of Γ_{Δ} is not the focus of this work, its behavior is reported together to that of Γ_{dq} for the sake of completeness. The sensorless technique based on the HF signal injection requires a high value of Γ_{Δ} and, in any case, different from zero. From (9.1), the map of ϵ in the i_d-i_q plane can be obtained, as the estimation error depends on the ratio of the two quantities in (9.22). Such an information can be exploited to determine the feasible operating regions using the HF voltage injection sensorless technique [142] or to implement an error compensation technique.

9.5.1. REL Machine

The l_{dq} loci resulting from the FE analysis on the REL machine are shown in Fig. 9.5(a). Both behavior and sign of l_{dq} agree with those predicted in Fig. 9.2 considering $I_{ch} = 0$. The l_{dq} locus is specular along the d– and q–axis, confirming that $l_{dq} = 0$ along the d– and the q–axis.

From Fig. 9.5(d) it can be noted that the REL machine exhibit a high saliency ratio to increase the reluctance torque component. Considerations on the position of $l_{dq} = 0$ in the i_d-i_q plane can be deduced from the current vs flux characteristics. Let refer to the point in which two i_d vs λ_d curves intersect. In such a point it is possible to write

$$\lambda_d(i_{dx}, i_{q1}) = \lambda_d(i_{dx}, i_{q2}) \tag{9.23}$$

where i_{dx} is the d–axis current of the intersection, i_{q1} and i_{q2} are the q–axis currents that correspond to the two i_d vs λ_d curves. If i_{q1} and i_{q2} are close enough, for the definition of l_{dq} in (9.5), it follows that $l_{dq} = 0$ in the point $(i_{dx}, \frac{i_{q1}+i_{q2}}{2})$. In Fig. 9.5(d), all the i_d vs λ_d curves intersect in the same point, that is, for $i_{dx} = 0$, confirming that $l_{dq} = 0$ is along the vertical line $i_d = I_{ch} = 0$.

Iron ribs are necessary in REL machines for mechanical reasons. From the magnetic point of view, they have a detrimental effect on the torque production because they increase the d–axis flux linkage, for given current. At steady state, such iron ribs are saturated. In order to study how the iron ribs affect the differential cross-saturation inductance l_{dq}, FE analysis has been carried out also on the REL machine without the iron ribs (i.e. replaced with air).

The Γ_{dq} and the Γ_{Δ} loci of the REL machine, with and without iron ribs, are reported in Fig. 9.6, limiting the analysis to the second quadrant of the i_d-i_q plane. Fig. 9.6 reports also the results of the experimental measurements on the REL machine, that will be discussed later.

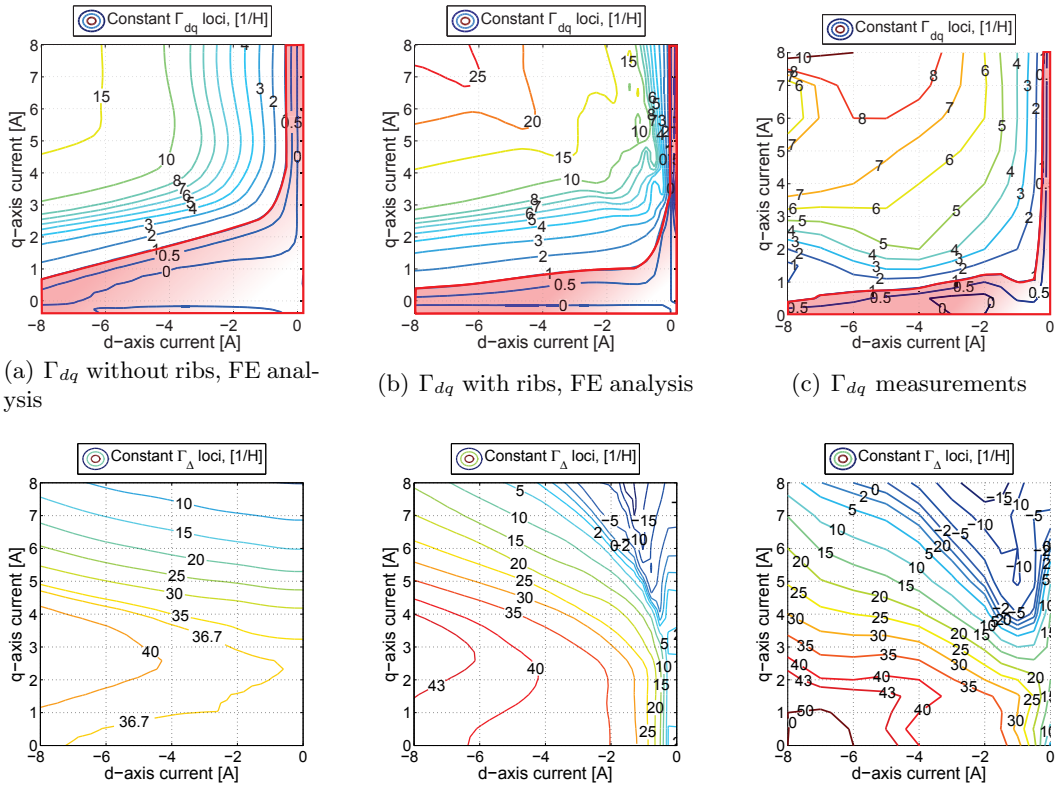

(a) Γ_{dq} without ribs, FE analysis

(b) Γ_{dq} with ribs, FE analysis

(c) Γ_{dq} measurements

(d) Γ_{Δ} without ribs, FE analysis

(e) Γ_{Δ} with ribs, FE analysis

(f) Γ_{Δ} measurements

Figure 9.6: Γ_{dq} and Γ_{Δ} loci in the i_d-i_q plane, REL machine

Comparing Fig. 9.6(a) with Fig. 9.6(b), it is worth noticing that the presence of the iron ribs tends to thicken the Γ_{dq} curves along the q–axis. This is reasonable since when $i_d = 0$ the iron ribs are unsaturated and both d– and q–magnetic circuits are linear. On the other hand, iron ribs saturate with small i_d currents. As far as Γ_{Δ} is concerned, a similar thickening of the Γ_{Δ} curves is observed in Fig. 9.6(e). The rapid saturation of the ribs with the i_d current yields a rapid variation of Γ_{Δ} values. When the ribs are saturated, Γ_{Δ} tends to equate the values with no ribs, Fig. 9.6(d). In this region, a further increase of Γ_{Δ} requires higher values of current.

A satisfactorily agreement is found between the experimental results shown in Fig. 9.6(c) and the FE analysis, Fig. 9.6(b). The quantities Γ_{dq} and Γ_{Δ} exhibit the same trend both in experimental measurements and in FE analysis. The slight difference between measured and predicted quantities may be due to the measurement uncertainty. Another cause of discrepancy is that an ideal B-H curve is assumed in the simulations. Especially in the iron ribs or, in general, for high flux density, the actual iron B-H curve can defers from the manufacturer specification. However, the experimental results allow the analytical and FE analysis to be validated.

9.5.2. IPM Machine

As said above, it is expected that $l_{dq} = 0$ along both the i_d–axis and the straight line $i_d = I_{ch} = -\Lambda_m / L_d$, as illustrated in Fig. 9.2. Similarly to the REL machine, the IPM machine has been studied by means of FE model. The l_{dq} loci in the i_d-i_q plane are reported in Fig. 9.5(b). The simulation results confirm that the $l_{dq} = 0$ locus is along $i_q = 0$. For high $\mid i_q \mid$ currents, the $l_{dq} = 0$ locus approaches the predicted straight line $i_d = I_{ch}$. In fact, in the IPM machine under analysis, $\Lambda_m = 0.19\ Wb$, $L_d = 24\ mH$ so that $I_{ch} = -8\ A$. At low i_q current, the iron saturation is low and the $l_{dq} = 0$ locus approaches the origin of the i_d-i_q plane.

Fig. 9.5(e) shows the current vs flux characteristics of the IPM machine. It is worth noticing that in this case the i_d vs λ_d curves intersect always at negative i_d, confirming that the $l_{dq} = 0$ locus is along a curve that lies in the second and third quadrant of the i_d-i_q plane.

Fig. 9.7(a) and 9.7(b) show a detail of Γ_{dq} and Γ_Δ behaviors without and with the iron ribs, respectively. Due to the impact of the PM flux, there is only a slight change in the Γ_{dq} loci. The presence of the ribs tends to move Γ_{dq} curve toward lower $\mid i_d \mid$ currents.

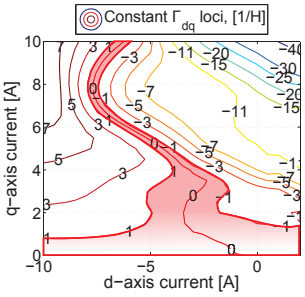

(a) Γ_{dq} without ribs, FE analysis

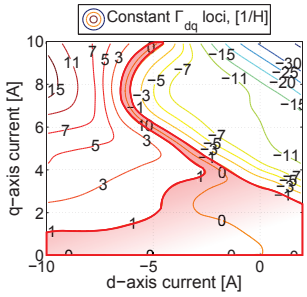

(b) Γ_{dq} with ribs, FE analysis

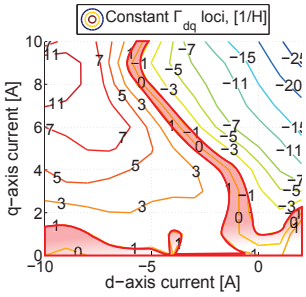

(c) Γ_{dq} measurements

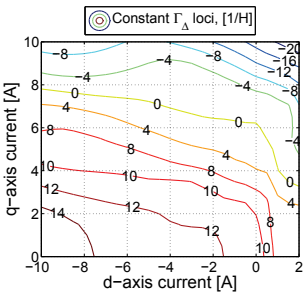

(d) Γ_Δ without ribs, FE analysis

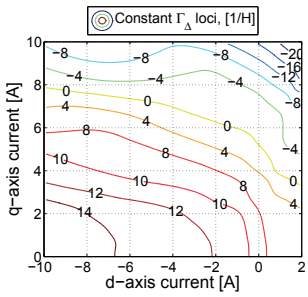

(e) Γ_Δ with ribs, FE analysis

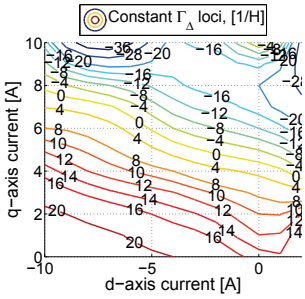

(f) Γ_Δ measurements

Figure 9.7: Γ_{dq} and Γ_Δ loci in the i_d-i_q plane, IPM machine

From the comparison between experimental measurements and FE analysis it results that the Γ_{dq} loci is predicted satisfactorily. The measured constant Γ_{dq} loci exhibit a similar shape of the simulated one. Good agreement is found also for the Γ_Δ loci. In particular, the $\Gamma_\Delta = 0$ is predicted with a better precision. Higher discrepancy but with reasonable value is found for higher values of current.

9.5.3. SPM machine

The SPM machine can be considered as a particular case of the IPM machine in which the difference between the l_d and l_q inductance is minimal. In addiction, there is no iron ribs in the rotor and saturation is limited in tooth tips. This SPM machine is characterized by low l_{dq} compared with the REL and IPM machine described above, as can be noted from Fig. 9.5(c) and Fig. 9.5(f). It is characterized by $\Lambda_m = 0.08\ Wb$, $L_d = 3.2\ mH$ so that $I_{ch} = -25\ A$. The FE analysis confirms again that $l_{dq} = 0$ along $i_q = 0$ and along the straight line $i_d = I_{ch}$, as illustrated in Fig. 9.5(c).

Fig. 9.8 show the Γ_{dq} loci of the SPM machine achieved by FE analysis, together with that obtained by the experimental results. The comparison between FE and experimental values of Γ_{dq} shows a satisfactory agreement. The Γ_Δ locus is not reported, since in SPM machine it is not of interest due to the very small difference between the l_d and l_q inductances.

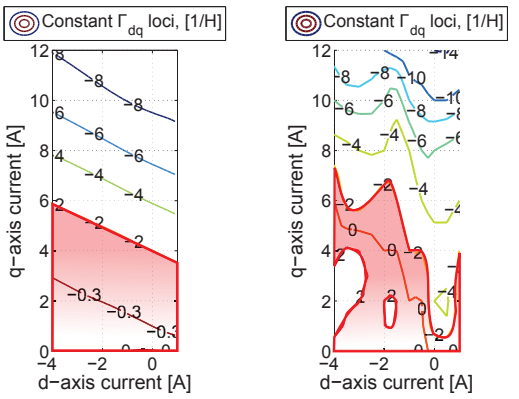

(a) Γ_{dq}, FE analysis (b) Γ_{dq}, measurement

Figure 9.8: FE analysis and experimental result, SPM machine

9.6. Experimental validation

In order to validate the analysis described in the previous Sections, the parameters Γ_{dq} and Γ_Δ of the three machines (REL, IPM and SPM) have been experimentally measured.

The measurement technique is based on feeding the motor adding HF voltages to the fundamental voltages. Such HF sinewave voltages are supplied in a synchronous d^x–q^x reference frame, but not coincident to the actual d–q reference frame (see Fig. 9.9). The d^x–q^x reference frame rotates at the speed ω_m^e. The test has been carried out at locked rotor, that is $\omega_m^e = 0$. At locked rotor, the stator voltages (9.4) in the d^x–q^x reference frame become:

$$\begin{cases} v_d^x = R_s i_d^x + l_d(i_d^x, i_q^x)\dfrac{di_d^x}{dt} + l_{dq}(i_d^x, i_q^x)\dfrac{di_q^x}{dt} \\ v_q^x = R_s i_q^x + l_{qd}(i_d^x, i_q^x)\dfrac{di_d^x}{dt} + l_q(i_d^x, i_q^x)\dfrac{di_q^x}{dt} \end{cases} \tag{9.24}$$

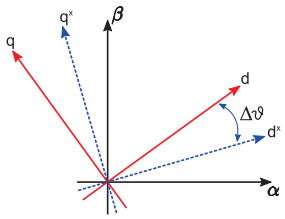

Figure 9.9: Stationary (α–β) and synchronous (d–q) reference frames, related to the estimated position. The d^x–q^x reference frame is a generic rotating frame

The HF signal is injected along the d^x–axis, that is

$$\begin{aligned} v^x_{hd} &= V^x_h \cos(\omega_h t) \\ v^x_{hq} &= 0 \end{aligned} \tag{9.25}$$

Using (9.24) and (9.25) and solving in the steady-state, after ignoring the resistance voltage drop, the HF current is obtained [143, 144]:

$$i^x_{hq} = -\frac{l_\Delta \sin(2\Delta\theta) + l_{dq}\cos(2\Delta\theta)}{l_d l_q - l^2_{dq}} \frac{V^x_h}{\omega_h} \sin(\omega_h t) \tag{9.26}$$

where $\Delta\theta$ is the angular displacement between d^x–q^x and d–q (see Fig. 9.9).

A dSPACE fast-prototyping system is adopted to control the currents. The adopted block scheme of experimental measurement setup is reported in Fig. 9.10. The machine is controlled by a voltage-source inverter which imposes HF voltage signals superimposed to steady-state voltages. This technique is similar to sensorless HF technique, but in this case the actual rotor position is known and the generic d^x–q^x reference frame

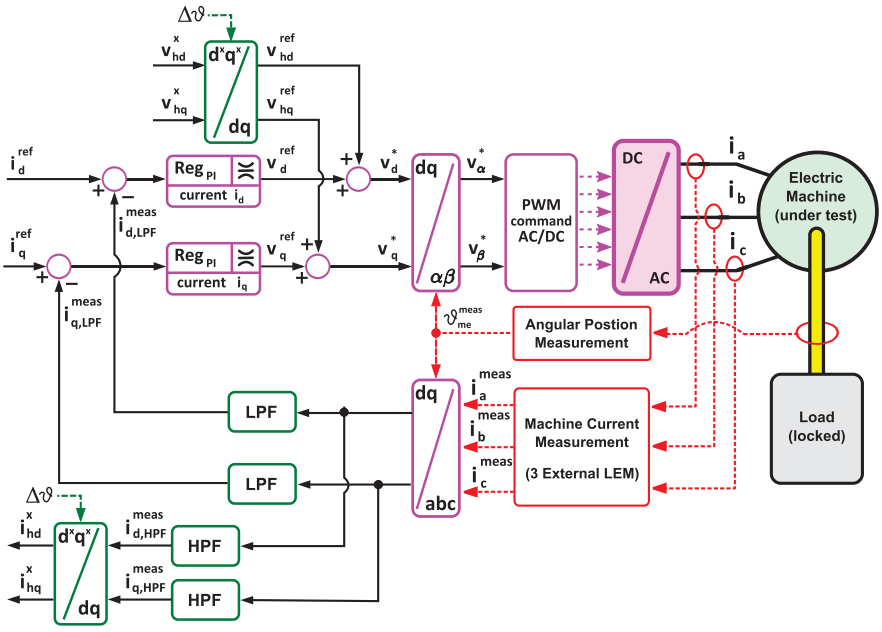

Figure 9.10: Block scheme of HF parameters measurement setup

is intentionally rotated with respect to the actual $d-q$ reference frame to characterize the machine parameters. The three currents are measured. The voltage reference values are adopted after the dead-time compensation block [145]. For a given value of $\Delta\theta$, the quantities Γ_{dq} and Γ_{Δ} can be extracted from the measured current i_{hq}^{x}. By imposing $\Delta\theta = 0$ the current i_{hq}^{x} results in

$$i_{hq}^{x} = -\frac{l_{dq}}{l_d l_q - l_{dq}^2}\frac{V_h^x}{\omega_h}\sin(\omega_h t) = -\Gamma_{dq}\frac{V_h^x}{\omega_h}\sin(\omega_h t) \tag{9.27}$$

from which Γ_{dq} is achieved. If $\Delta\theta = \pi/4$, the quadrature current is

$$i_{hq}^{x} = -\frac{l_{\Delta}}{l_d l_q - l_{dq}^2}\frac{V_h^x}{\omega_h}\sin(\omega_h t) = -\Gamma_{\Delta}\frac{V_h^x}{\omega_h}\sin(\omega_h t) \tag{9.28}$$

that allows the parameter Γ_{Δ} to be obtained.

The achieved parameters Γ_{dq} and Γ_{Δ} have been reported in the i_d-i_q plane in Fig. 9.6, Fig. 9.7 and Fig. 9.8 for a direct comparison with those obtained by FE analysis.

9.7. Conclusions

This Chapter gives the basis of the properties of the differential cross-saturation inductance for different types of synchronous machines. From the analysis, it has been demonstrated that the locus $l_{dq} = 0$ is not only along $i_q = 0$ and where there is no iron saturation, but also along $i_d = I_{ch}$. It has been shown (by means of theory, FE simulations and tests) that this is a general result, which is valid for all the considered machines. The sign of l_{dq} in the i_d–i_q plane is determined. Such an information can be adopted in direct axis polarity detection methods, which are based on the identification of the sign of l_{dq} at locked rotor.

The analysis is in satisfactory agreement with FE and experimental results. The quantity Γ_{dq} (proportional to l_{dq}) is used to compare FE results with those of measurements. For the sake of completeness, the behavior of Γ_{Δ} (proportional to the difference between l_d and l_q) is reported too. It is shown that the map of the position error ϵ (dependent on the ratio between Γ_{dq} and Γ_{Δ}) can be achieved both with FE and with experimental measurements. The map of ϵ is useful to determine the feasible operating regions using the HF voltage injection sensorless technique or to implement any error compensation technique.

The impact of rotor iron ribs on l_{dq} is analyzed by means of FE. As far as the REL machine is concerned, the iron ribs move the $l_{dq} = 0$ locus toward lower $\mid i_d \mid$ currents and thick the l_{dq} loci along $i_d = 0$. The iron ribs reduce the sensorless rotor position detection region (where $\Gamma_{\Delta} \neq 0$). In the IPM machine the impact of iron ribs is limited.

9.8. Appendix

Hereafter, the HF current trajectory of the IPM motor described Section 9.2 (Fig. 9.1(b)) is analyzed for different working points which are close to the MTPA trajectory. This analysis helps the reader to understand more in detail the impact of l_{dq} and l_{Δ} on the sensorless rotor position detection. The HF current trajectory are computed at zero speed. To better exploit the machine parameters effect, a rotating HF voltage signal ($V_h = 50V$, $\omega_h = 200Hz$) is assumed to be injected in the stator winding. The corresponding HF currents are:

$$\begin{aligned} i_{dh}(i_d, i_q) &= \frac{V_h}{\omega_h} \frac{\left(l_q \sin \omega_h t \, + \, l_{dq} \cos \omega_h t\right)}{l_d l_q - l_{dq}^2} \\ i_{qh}(i_d, i_q) &= \frac{-V_h}{\omega_h} \frac{\left(l_d \cos \omega_h t \, + \, l_{dq} \sin \omega_h t\right)}{l_d l_q - l_{dq}^2} \end{aligned} \tag{9.29}$$

The inductances are computed from FE results by (9.21). They refer to the steady state working points illustrated in Fig. 9.11. Refer also to Γ_{dq} and Γ_{Δ} of Fig. 9.7(b) and Fig. 9.7(e). In particular:

Referring to Fig. 9.11:

- Fig. 9.11(a): This point is characterized by $I_d = -2.7A$ and $I_q = 4A$. In this point, $l_{dq} \simeq 0$. Consequently the major axis of the current ellipse is rotated by $\epsilon \simeq 0$ with respect to the actual d-axis. The detectable HF saliency is defined as the ratio between the current oscillations along the maximum and the minimum ellipse axis [120];
- Fig. 9.11(b): This point is characterized by $I_d = -6A$ and $I_q = 7A$, $l_{dq} \simeq 0$ and $l_d \simeq l_q$. This is a critical point from the point of view of the sensorless position detection since the ellipse degenerates into a circle;
- Fig. 9.11(c): This point is characterized by $I_d = -10A$ and $I_q = 8A$, $l_{dq} \neq 0$ and $l_d \simeq l_q$. Even though the two differential inductances are equal, the angular displacement of the ellipse results in $\epsilon = \frac{\pi}{4}$;
- Fig. 9.11(d) This point is characterized by $I_d = -8A$ and $I_q = 5A$, $l_{dq} \neq 0$ and $l_d \neq l_q$. In this case the ellipse is rotated of the angle ϵ, which is the error in the rotor position estimation caused by the d- and q-axis cross-saturation.

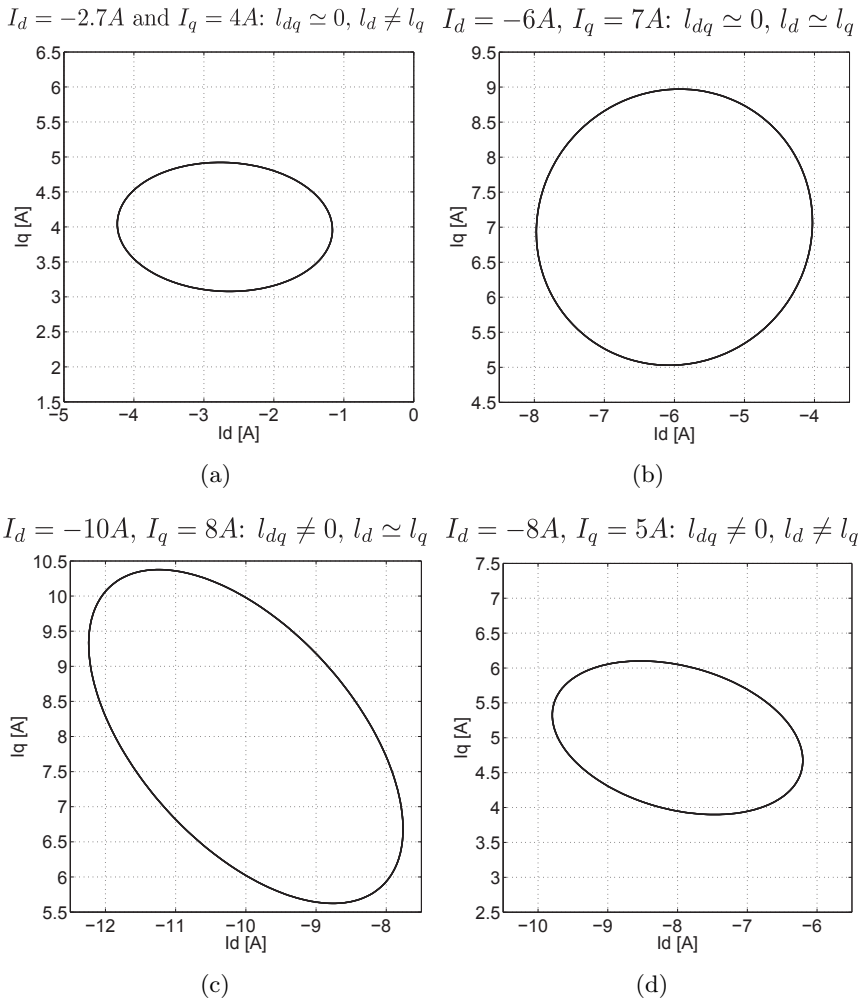

Figure 9.11: HF current trajectory in the IPM machine

Chapter 10

Ring Losses Evaluation in Ringed Pole PM motors

In this Chapter, the ringed–pole surface-mounted permanent magnet machine is investigated from the point of view of the ring losses. The rings around the poles create a high frequency anisotropy that is useful to detect the rotor position by means of a high frequency signal injection. However, the presence of the rings causes additional rotor losses. The causes of ring losses are investigated. The first cause is the high frequency signal injection itself. The harmonics in the airgap magnetomotive force, which are not synchronous with the rotor and so induce currents in the rings, are the second source of losses. The third source is the airgap flux fluctuation due to stator slotting. Machines of different sizes and winding types are investigated. Finite element analysis and analytical model are used to estimate the ring losses, comparing the results. The influence of the ring cross section area on the ring losses is analyzed, showing that the ring losses can be reduced in certain configurations.

10.1. Introduction

The ringed–pole rotor configuration exhibits an anisotropic electromagnetic behavior at a high frequency [146]. The rotor position is estimated by means of a high frequency voltage injection, allowing the widely known low and zero speed sensorless technique to be applied [147, 148]. A ringed–pole rotor is shown in Fig. 10.1(a). It uses a short circuited copper ring around each pole [148], in order to modify the direct axis flux linkage dynamics. Alternatively, a rotor cage, whose bars are between the magnets, can be adopted [149] as shown in Fig. 10.2. This solution refers to an external rotor configuration, where the cage allows an easier placement of the PMs. A different copper bar cross section area can be introduced among the poles, modifying the rotor high frequency saliency [131, 149]. The two methods are both effective for high frequency sensorless detection. The choice of using a cage instead of separated rings is mainly due to manufacturing reasons. The performance of sensorless control in ringed–pole machines has been verified in literature [131, 147–151]. However, only small size machines have been considered.

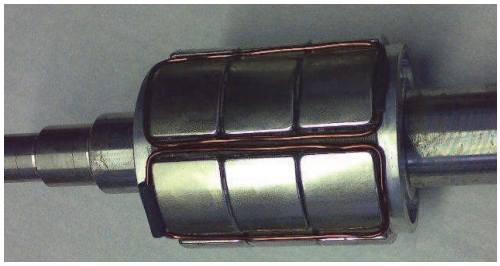

(a) Ringed–pole SPM rotor

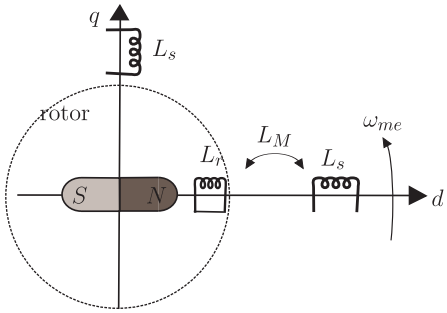

(b) d–q model of the motor

Figure 10.1: Ringed–pole rotor configuration and corresponding d–q model

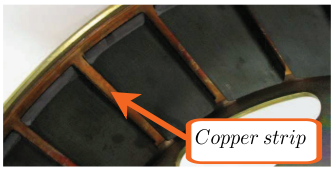

(a) Copper cage - low filling

(b) Copper cage - medium filling

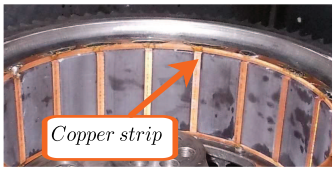

(c) Copper cage - high filling

Figure 10.2: Example of ringed–pole machines with different quantity of copper

The magnetic model of the machine in the d–q reference frame is reported in Fig. 10.1(b). From the electrical point of view, the ring is an additional coil along the direct axis, with inductance L_r and resistance R_r. A mutual inductance L_M occurs between the ring and the stator winding of d–axis. The effect of the ring is to modify the response of the current along the d–axis. However, there are additional losses due to the current that flows in the rings themselves. The various sources of losses in the rotor rings are:

- the effect of the magneto-motive force (MMF) harmonics, which are not synchronous with the rotor [152–160]. The effect of this source of losses on the rings has not yet been investigated in the literature;
- the effect of the injection signal itself [131, 148, 161];
- the effect of the airgap flux fluctuation due to the stator slotting [157, 162–166]. Neither this aspect has been investigated considering ringed–pole rotors yet.

This part of the thesis investigates the losses due to each source listed above for small and large size machines, respectively. The impact of the winding type of the machine is also considered in the analysis. The aim is to investigate if the ringed–pole technique can be adopted also for large machines from the additional losses point of view.

FE analysis is used to compute such losses. The stator is conveniently substituted by an equivalent currents sheet that allows any high-frequency stator harmonic to be reproduced. Therefore, the three sources of losses are reproduced separately by means

of such a current sheet. The possibility of segregating the different source of losses, not feasible experimentally, is key to estimating the contribution of each factor to the total losses.

An analytical approach is also proposed to rapidly estimate the ring losses. At first the analytical model is applied to the case of separated rings between the poles. After that, the analysis is extended to the case of a whole conductive cage. Comments on the peculiarities of the solution with rings and cage are included. At last, the influence of the ring geometry and cross section area on the ring losses is investigated.

10.2. Sources of losses

During the normal operation of the ringed–pole machine, there are three main causes of losses in the rings that are wound around the poles.

The MMF space harmonics are the first cause of losses. More specifically, fractional slot machines are characterized by a high content of MMF harmonics [152–154]. Such harmonics, but the main harmonic, rotate with respect to the rotor reference frame. The effect is a variable flux in the rotor, which induces eddy currents in any rotor conductive part. The amplitude and the frequency of this variable flux depends on the winding configuration (no. of poles, no. of slots and if double– or single– layer), the rotating speed and the MMF harmonic order.

The second source is the injection of high frequency current, that is necessary for position sensing. Such a high frequency current causes losses in the rings. In [161], the ring losses due to the high frequency injection have been experimentally measured. They are less than 2 W on a 6–pole, 27–slot Surface mounted Permanent Magnet (SPM) machine, whose rotor diameter is $D_i = 70\ mm$ and stack length $L_{stk} = 65\ mm$. In [131], an evaluation of the cage losses has been carried out for different frequencies and materials. Generally speaking, these losses are quite low in small size machines, and they can be often neglected. However, since rotor losses increase significantly with the dimension of the machine [122], it is necessary to carry out the analysis for large machines.

The third source of ring losses is the airgap flux fluctuation caused by the different magnetic permeance along the airgap, introduced by the stator slot openings. The effect of the slotting causes losses also in the PMs, that can be high for wide slot openings [155, 156, 162, 163, 165].

The aim of this Chapter is to study the effect of each of these three sources of losses in different configurations of ringed–pole SPM machines. In all simulations, both the magnets and the copper cage have been considered as being conductive. In order to take into account the lamination effect, a conductivity equal to zero has been applied in the iron.

Table 10.1: Main data of the simulated machines

machine	winding	airgap diameter D_i $[mm]$	external diameter D_e $[mm]$	length L_{stk} $[mm]$
machine A	48/40	1000	1250	300
machine B	12/10	70	135	63
machine C	27/6	63.5	120	63

10.3. Study cases

The analysis of the ring losses is carried out on three machines, whose main data are reported in Table 10.1. The three machines have been chosen in order to investigate how the machine size and the winding MMF harmonic content affect the ring losses. A large machine and two small machines with different winding MMF harmonic content are analyzed.

Machine A is a large machine with inner diameter $D_i = 1\ m$, external diameter $D_e = 1.25\ m$ and stack length $L_{stk} = 0.3\ m$. It is a 200 kW SPM machine and it is illustrated in Fig. 10.3(a). PMs are segmented in 4 parts along the circumferential direction to reduce the PM eddy current losses [167–170]. The machine has a 48–slot 40–pole winding (main harmonic order $\nu = 20$) and its rated electric loading is $\hat{K}_{sp} = 100\ kA/m$ (current density 4 A/mm^2). Both Single–Layer (SL) and Double–Layer (DL) windings are considered. The subharmonic with order $\nu = 4$ exhibits a winding factor about 27% of the main one for SL winding and 7% for DL winding, respectively. The amplitude of such a MMF harmonic results to be 136% of the main MMF harmonic for SL winding and 35% for DL winding. However, the harmonic order closest to the main is $\nu = 28$ (amplitude 70% of the main both for SL and DL), which is a slot harmonic [154], that is, with the same winding factor of the main harmonic.

Machine B is a smaller machine, with inner diameter $D_i = 70\ mm$, external diameter $D_e = 135\ mm$ and stack length $L_{stk} = 63\ mm$. It is a 1.5 kW, 12–slot 10–pole machine, whose rotor is sketched in Fig. 10.3(b). Its rated electric loading is $\hat{K}_{sp} = 70\ kA/m$ (current density 6 A/mm^2). Its harmonic content is the same that of **machine A**, but with periodicity one fourth. The main MMF harmonic order is $\nu = 5$, the subharmonic order is $\nu = 1$ and the first slot harmonic order is $\nu = 7$.

Finally, **machine C** is a 0.7 kW, 27–slot 6–pole machine with inner diameter $D_i = 63.5\ mm$, external diameter $D_e = 120\ mm$ and stack length $L_{stk} = 63\ mm$. The rated electric loading is $\hat{K}_{sp} = 38\ kA/m$ with a current density of 6 A/mm^2. The rotor is drawn in Fig. 10.3(c). In this case the machine dimensions are similar to those of **machine B**, but there is a lower harmonic content. The main harmonic order is $\nu = 3$ and there are not any MMF subharmonics. The MMF harmonic order closest to the main is $\nu = 6$ (amplitude only 3.4% with respect to the main) and the first slot harmonic order is $\nu = 24$ (amplitude 12% with respect to the main). The key difference of the **machine C** with respect to the previous two machines is that it has a distributed winding.

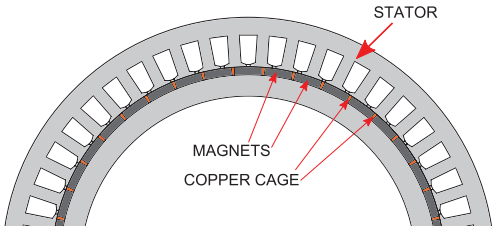

(a) Sketch of 48–slot 40–pole SPM machine with copper cage (**machine A**)

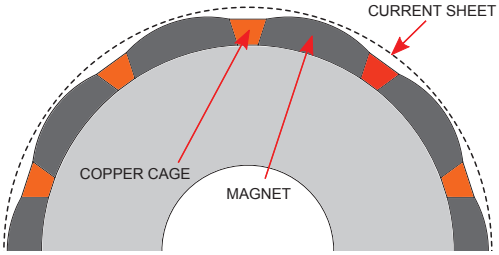

(b) Sketch of 10–pole SPM rotor with copper cage (**machine B**)

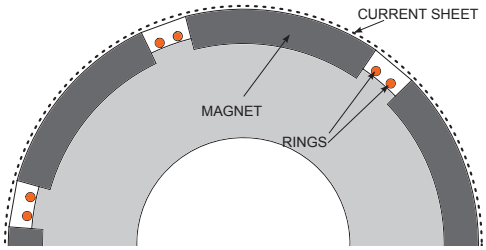

(c) Sketch of 6–pole SPM rotor with copper rings (**machine C**)

Figure 10.3: SPM ringed–pole machines

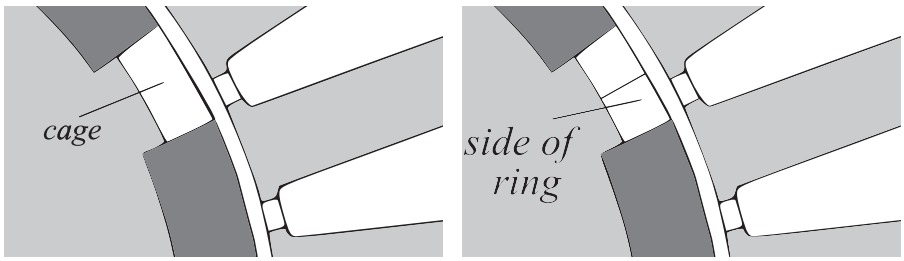

(a) Cage (b) Ring

Figure 10.4: Cage and ring with the same copper volume

The three study cases has been analyzed with cage and rings among the poles. The quantity of copper used for the rings or cage affects the amount of losses in the copper itself, as explained in Section 10.9. In the FE analysis, rings and cage are designed with the same copper volume to better compare the results, as illustrated in Fig. 10.4.

10.4. Ring losses due to airgap MMF harmonics

In order to determine the impact of each MMF harmonic on the ringed–pole rotor losses, various FE simulations have been carried out. The stator is replaced by an equivalent distribution of currents, as shown in Fig. 10.3. The circumference is split into a high number of points, e.g. N_p, with distance $\pi D/N_p$. The peak current is computed from the electric loading $\hat{K}_s$, as $\hat{I}_p = \hat{K}_s \pi D/N_p$. According to such a peak value, a *point current* is assigned to each point to reproduce the linear current density distribution over an arc length $\pi D/N_p$.

The currents are assigned to reproduce the effect of each MMF harmonic. Then, losses are computed by means of the superimposition of the effects of each MMF harmonic [171]. This is true if no saturation in the iron is hypothesized. For each harmonic order ν–th, the maximum current value is computed from the electric loading $\hat{K}_{s\nu}$, as $\hat{I}_{p\nu} = \hat{K}_{s\nu} \pi D/N_p$.

The peak value of the main harmonic electric loading is fixed and depends on the considered machine. The amplitude of the other electric loading harmonics is computed according to the winding type (number of slots and poles). Only DL winding is considered in this section. A comparison between SL and DL winding is presented in Subsection 10.4.1. The linear current density harmonic waveforms rotate along the air-gap at a given speed [152] in the rotor reference frame. Using the symbolic notation, in the generic angular position ϑ, the *point current* is forced to be

$$\dot{I}_{p\nu}(\vartheta) = \hat{I}_{p\nu} e^{j\nu\vartheta} \tag{10.1}$$

In other words, the phase of the current (i.e. $\nu\vartheta$) is fixed to be a function of the geometrical position ϑ of the point in which the current itself is assigned. The frequency of the simulation is computed as

$$f_{\nu r} = f\left(sgn \cdot \frac{\nu}{p} - 1\right) \tag{10.2}$$

where sgn is equal to $+1$ or -1 according to whether the harmonic speed is forward or backward in relation to the rotor speed and f depends on the rotor speed. For each machine, the two ringed–pole rotor configurations are investigated: the first with separated rings wound around each pole, and the second with a whole copper cage whose bars are between each PM. The losses in the PMs are also reported for the sake of comparison. The analysis for **machine A** has been carried out for the rotating speed of $n = 100\ rpm$ that corresponds to a main frequency of $f = 33.33\ Hz$. **Machine B** and **machine C** have been studied with a rotating speed $n = 1000\ rpm$. The losses due to the MMF harmonics are shown in Table 10.2.

Higher losses are achieved in large size machine (**machine A**). In small size machines (**machine B** and **machine C**) the losses are smaller but not always negligible. Table 10.2 also reports (in brackets) the percentage of the losses compared to the rated power. The losses reach some percentage points of the rated power in large size machines (**machine A**) and in fractional slot machines (**machine A** and **machine B**). **Machine C** exhibits the lowest losses since the corresponding distributed winding yields a low MMF harmonic content. Even if the computation has been carried out

Table 10.2: Rotor losses due to MMF harmonics in the three motors at rated electric loading and speed. Ratio $losses/P_{nom}\%$ in parenthesis

Winding		Cu [W]	PM [W]
48/40	cage	4700 (2.4%)	700 (0.3%)
	ring	6800 (3.4%)	700 (0.3%)
	nothing	–	800 (0.4%)
12/10	cage	20 (1.3%)	1.4 (0.1%)
	ring	26 (1.7%)	1.7 (0.1%)
	nothing	–	2.2 (0.2%)
27/6	cage	1.4 (0.2%)	0.1 (0.01%)
	ring	0.5 (0.07%)	0.05 (0.007%)
	nothing	–	0.1 (0.01%)

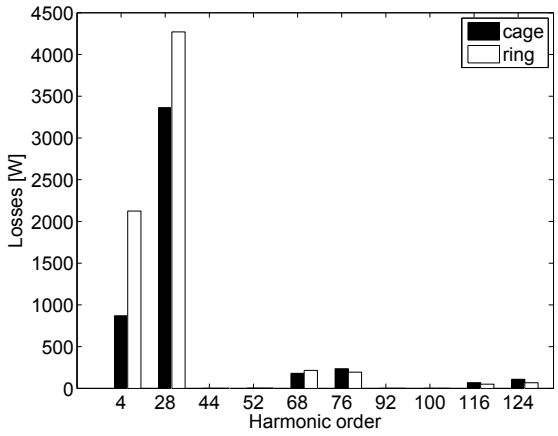

Figure 10.5: Ring losses for **machine A**, with both copper cage and rings between the poles (main harmonic is the $20-th$ order harmonic)

on specific machines, the general result is that both (i) large size machines and (ii) fractional slot machines exhibit higher ring losses.

Moreover, using the rotor cage instead of separated rings around each pole, losses are lower for **machine A** and **machine B**, i.e. when fractional slot winding is adopted. On the contrary, for **machine C**, which has a distributed winding, losses are lower when separated rings are adopted. This behavior will be investigated hereafter.

Fig. 10.5 shows the copper losses due to the different harmonics for **machine A**, both using cage and using separated rings. The main harmonic, whose order is $\nu = 20$, is synchronous with the rotor, therefore it produces no losses. The highest losses are induced by the harmonic of 28–th order. Generally, high losses are caused by the MMF harmonics of lower order, often subharmonics, but also close to the main harmonic, even if not necessarily both. This is a general result when dealing with rotor losses due

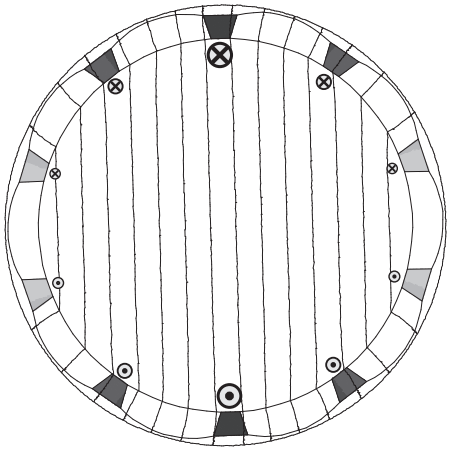

Figure 10.6: Cage current distribution when a 2 pole, $10Hz$ harmonic is rotating along the airgap (crosses and points define the current direction)

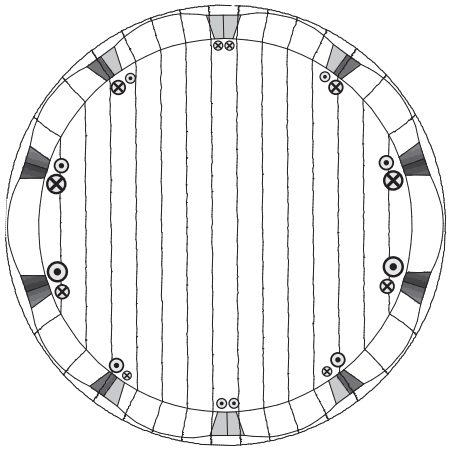

Figure 10.7: Rings current distribution when a 2 pole, $10Hz$ harmonic is rotating along the airgap (crosses and points define the current direction)

to MMF harmonics [152, 153]. Fig. 10.5 also shows that using rings, losses are higher for low harmonic orders ($\nu = 4$ and $\nu = 28$ in the figure), while they are slightly lower for higher order harmonics.

It is interesting to compare the current distribution in the cage for low order harmonics with the rings one. Low order harmonics exhibit a wave length that is longer than the pole pitch. Referring for example to Fig. 10.6, in which a 2–pole harmonic is rotating along the airgap, the cage acts as an induction motor one. On the other hand, when separated rings are adopted, currents are forced to flow in each ring, Fig. 10.7. According to the results of Fig. 10.5 and Table 10.2, the use of a cage rather than separated rings between the pole seems to be convenient when there are sub–harmonics or harmonics close to the main. However, this result can not be generalized, since the losses depends from the ring cross section, as pointed out in Section 10.9. Higher order harmonics exhibit a wave length that is comparable to the pole pitch. In this case, both cage and rings behave similarly.

Table 10.3: Rotor losses due to MMF harmonics in **machine A**. Ratio $losses/P_{nom}\%$ in parenthesis

Winding type		Cu [kW]	PM [kW]
DL	cage	4.7 (2.4%)	0.7 (0.3%)
	ring	6.8 (3.4%)	0.7 (0.3%)
	nothing	–	0.8 (0.4%)
SL	cage	16.0 (8.0%)	0.7 (0.4%)
	ring	34.3 (17.2%)	1.0 (0.5%)
	nothing	–	0.8 (0.4%)

As a further consequence, the shielding effect of cage and rings limits the induced current in the PMs so that the associated losses are lower, as shown in Table 10.2. If either the copper cage or the rings are removed, an increase in the losses in the PMs is expected.

As a result, the MMF losses should be taken into account when designing a large size ringed–pole machine. Particular attention must be paid to machines with fractional slot winding, which have a high MMF harmonic content.

10.4.1. Impact of the number of layers

In this Subsection the impact of the number of the layers of the winding is investigated. The same model applied in Section 10.4 is adopted to compute the MMF harmonic losses in the different rotor parts. **Machine A** is considered, with both whole copper cage and rings between the poles. The rated electric loading is again $\hat{K}_{sp} = 100\ kA/m$ and the rotor speed is $n = 100\ rpm$ as in Section 10.4. Simulations are carried out for both SL and DL winding and the comparison is reported in Table 10.3. The results show that the difference between the losses of the whole cage and the losses of the rings increase when a SL winding is used. Generally speaking, the losses of the SL winding are greater than that of the DL winding. This is due to the fact that machines with SL winding exhibit a higher MMF harmonic content. More specifically, in **machine A** the MMF subharmonic of order $\nu = 4$ has a great impact, causing the increase in losses shown in Fig. 10.8.

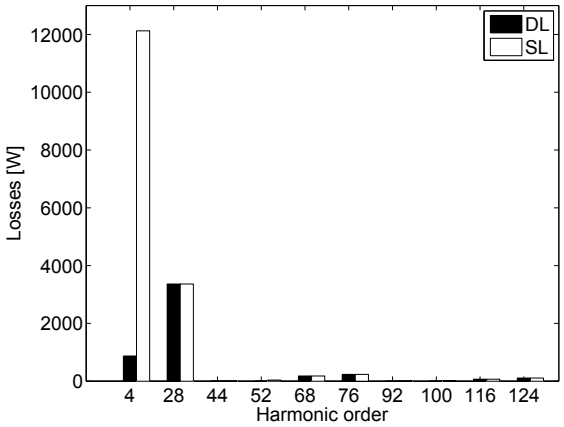

Figure 10.8: Ring losses for **machine A**, whole copper cage between the poles, DL vs SL winding

Table 10.4: Rotor losses due to MMF harmonics in **machine A** for different airgap heights. Ratio $losses/P_{nom}\%$ in parenthesis

	g=3 mm	g=4 mm	g=5 mm
cage [kW]	4.7 (2.4%)	4.2 (2.1%)	4.0 (2.0%)
PM [kW]	0.7 (0.3%)	0.5 (0.3%)	0.4 (0.2%)

10.4.2. Impact of the amplitude of airgap

In this Subsection the impact of the airgap height is investigated from the point of view of the losses due to the MMF harmonics. Once again the model applied in Section 10.4 is used and **machine A** with whole copper cage between the poles is considered. Simulations are carried out for a DL winding, with three different airgaps, that are, $g = 3,\ 4,\ 5\ mm$. The simulations carried out in the other Sections refer to an airgap $g = 3mm$. Table 10.4 shows the obtained results. As expected, losses decrease when increasing the airgap height. The decrease is not proportional to the airgap amplitude, since the reducing effect is more relevant for high order harmonics [152]. Low order harmonics are less influenced by the airgap height. However, it is important to consider that increasing the airgap also causes the main MMF harmonic to decrease, affecting the performance of the machine.

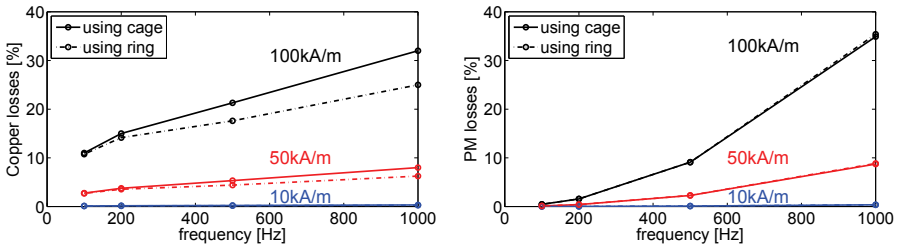

(a) Copper losses (b) PM losses

Figure 10.9: Losses due to signal injection, **machine A**

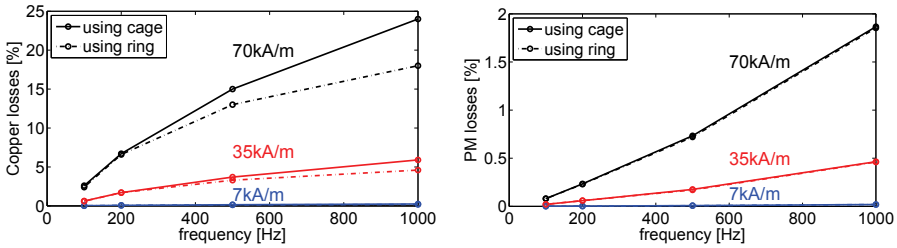

(a) Copper losses (b) PM losses

Figure 10.10: Losses due to signal injection, **machine B**

10.5. Ring losses due to signal injection

In order to estimate the impact of the signal injection on the joule losses, the current point model is used again.

Signal injection is carried out at different electric loadings $\hat{K}_s$ and different frequencies on the three machines presented above. Note that the common injection frequency is usually in the range 800 to 1000 Hz [149]. A reference value of the signal injection electric loading is from 10 to 20% of the rated electric loading. However, the signal injection electric loading should be as low as possible, so as to achieve information from the signal itself, but also to limit the losses. Higher electric loading signal injections are analyzed to be compared with the other source of losses. The rotor copper losses and the PM losses in the case of cage and rings are shown in Fig. 10.9, Fig. 10.10 and Fig. 10.11 for the 3 study cases, respectively. As expected, the higher the frequency, the higher the losses. Moreover, the figures confirm that the losses increase as the square of the electric loading. For high electric loadings the losses due to signal injection are high. The use of rings rather that cage among the poles allows the copper losses to be slightly reduced, while the PM losses are very similar in the two cases. In all cases, for a signal injection of 10% of the rated electric loading, the PM and the rotor copper losses are negligible.

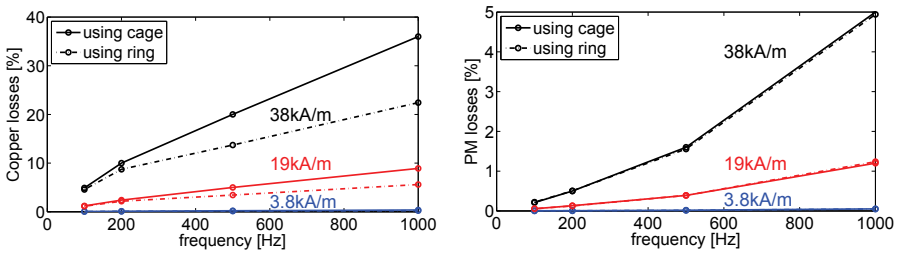

(a) Copper losses (b) PM losses

Figure 10.11: Losses due to signal injection, **machine C**

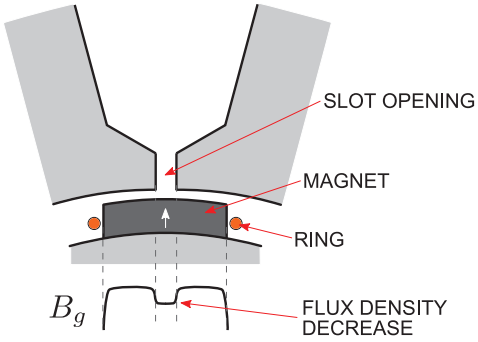

Figure 10.12: Sketch of the effect of the slot opening

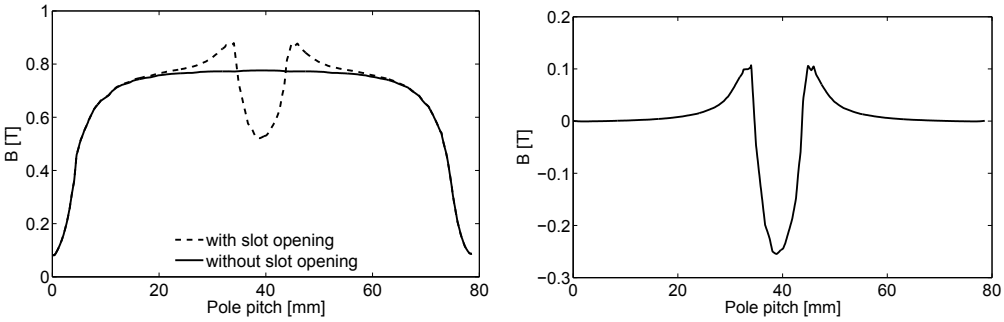

(a) Flux density above a pole (b) Flux density fluctuation

Figure 10.13: Slotting effect, **machine A**: slot opening width $w_{so} = 10mm$

10.6. Ring losses due to slot opening flux fluctuation

To compute the losses due to the slot openings, a deep analysis of the slot openings effect is carried out. Fig. 10.12 illustrates the effect of the slot opening on the PM flux density distribution. Referring to **machine A**, Fig. 10.13(a) shows the flux density distribution along a pole pitch with and without the slot opening. The PM flux density variation is highlighted in Fig. 10.13(b). This is a slight overestimation, since this disturbance is computed in the middle of the pole, i.e. when it is maximum.

When the machine is rotating, there is a relative speed between the rotor and the flux density variation. From the rotor point of view, this flux density moves along the

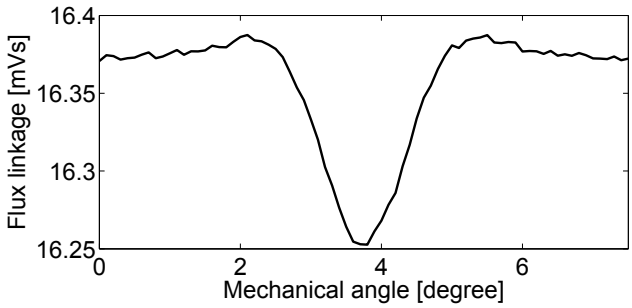

Figure 10.14: Flux linked by a ring around a PM in the **machine A**: slot opening width $w_{so} = 10mm$

airgap with the rotor speed ω_m. The main effect of this rotating flux density fluctuation is an electromotive force induced into the rotor conductive parts. As a consequence, eddy currents flow in both rotor rings and PMs. As an example, Fig. 10.14 shows the flux linked by a ring wound around a PM during a rotation of 7.5 degrees, which corresponds to a slot angle.

The rotor losses due to the stator slot openings are computed by considering the Fourier series expansion of the flux density variation (Fig. 10.13(b)). The amplitude of each harmonic $\hat{B}_\nu$ is derived and a series of FE simulations are then carried out, by reproducing each harmonic by means of the current sheet that substitutes the stator, similarly to the previous Sections. The corresponding electric loading is

$$\hat{K}_{s\nu} = \frac{\hat{B}_\nu \cdot N_s \cdot 2\nu \cdot (g + t_m)}{\mu_0 \cdot D_i} \tag{10.3}$$

where N_s is the number of stator slots, g is the airgap width, t_m is the thickness of the magnets, ν is the harmonic order and D_i is the inner diameter of the machine. The frequency of the simulations is set as

$$f_\nu = \frac{n}{60} \cdot N_s \cdot \nu \tag{10.4}$$

where n is the speed of the machine in round/min.

Table 10.5 shows the losses in **machine A** for different slot openings and with the same assumptions of Subsection 10.4.1. A whole copper cage and rings between the pole are considered. These results highlight that in **machine A** the losses due to the slot openings are very high. They represent an important contribution to the losses, according to [162, 163]. The greatest amount of losses arises in the rings. In **machine A**, such an effect is emphasized by the dimension of the machines [122]. The slot pitch of **machine A** is $w_s = 65.4\ mm$, so that the simulations are carried out for slot openings from 15% to 46% of the slot pitch. The rotor speed also has a great impact on the losses caused by the slot openings. In **machine B** and **machine C**, whose slot openings are 16% and 23% of the slot pitch, respectively, this source of losses is not relevant, as reported in Table 10.6. Table 10.6 reports the results for both **machine B** and **machine C**, with a rotating speed equal to $n = 1000\ rpm$.

Table 10.5: Losses due to slot openings in **machine A** for different values of slot opening. Ratio $losses/P_{nom}\%$ in parenthesis

slot opening	10 mm	20 mm	30 mm
cage [kW]	2.9 (1.5%)	9.1 (4.6%)	12.2 (6.1%)
PM [kW]	0.7 (0.4%)	2.9 (1.5%)	4.7 (2.4%)
ring [kW]	2.2 (1.1%)	6.1 (3.1%)	8.5 (4.3%)
PM [kW]	0.7 (0.4%)	3.0 (1.5%)	4.7 (2.4%)
nothing [kW]	-	-	-
PM [kW]	0.7 (0.4%)	2.9 (1.5%)	4.6 (2.3%)

Table 10.6: Losses due to slot openings in **machine B** and **machine C**. In parenthesis the ratio $losses/P_{nom}\%$

Winding	12/10	27/6
cage [W]	3.0 (0.2%)	0.06 (< 0.05%)
PM [W]	1.4 (0.08%)	0.006 (< 0.05%)
ring [W]	4.9 (0.3%)	0.38 (0.05%)
PM [W]	3.7 (0.2%)	0.05 (< 0.05%)
nothing [W]	-	-
PM [W]	3.7 (0.2%)	0.05 (< 0.05%)

10.7. Analytical model: rings

An analytical model has been developed to rapidly estimate the losses in a single ring around each pole. The circuital model, in which the ring leakage inductance is neglected, is shown in Fig. 10.15. The rotor rings are assumed to be identical. Each

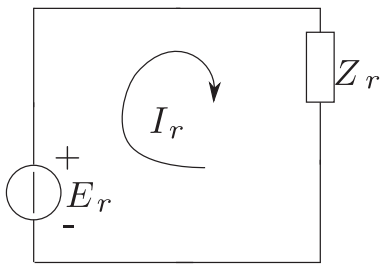

Figure 10.15: Circuital model of the rings

rotor ring is mutually coupled to the stator winding and to the other rings. It is assumed that currents in the rotor rings (or cage) and in the PM do not modify the

stator field. The ring resistance R_r is computed as:

$$R_r = 2 \cdot \rho \frac{L_{stk} + \tau_r}{S_r} \tag{10.5}$$

where τ_r is the ring pitch, L_{stk} is the stack length, ρ is the resistivity of the ring and S_r is the ring cross section area.

The flux linked by the k_{th} rotor ring only due to rotor currents (i_{rk}) is represented by λ_{rk}. Such a flux linkage is due to the ring self–inductance L_r and mutual inductance M_r among the rings. In matrix form,

$$\begin{bmatrix} \lambda_{r1} \\ \lambda_{r2} \\ ... \\ \lambda_{2p} \end{bmatrix} = \begin{bmatrix} L_r & M_r & ... & M_r \\ M_r & L_r & ... & M_r \\ ... & ... & ... & ... \\ M_r & M_r & ... & L_r \end{bmatrix} \begin{bmatrix} i_{r1} \\ i_{r2} \\ ... \\ i_{r2p} \end{bmatrix} \tag{10.6}$$

It is assumed that there is no saturation along iron paths, so that superimposition of the effect can be applied to the computation of the losses. The contribution of each MMF harmonic is computed separately and the losses are computed at steady state. From the reluctance of the flux path $\Re_r$ corresponding to each ring (the number of turns is $n = 1$), the ring self–inductance is:

$$L_r = \frac{n^2}{\Re_r} = \frac{\mu_0 L_{stk} \pi D(2p-1)}{(2p)^2 (g + t_m/\mu_r)} \tag{10.7}$$

where $g + t_m/\mu_r$ is the actual airgap (air and magnet thickness), μ_r is the relative permeability of the PM. Due to the rotor symmetry, the mutual inductance between two rings corresponds to

$$M_r = \frac{-L_r}{2p-1} \tag{10.8}$$

where $2p$ is the number of poles and also the number of rotor rings. If $B = \hat{B}\sin(x/R\nu)$ is the MMF harmonic of ν–th order the airgap flux density, the flux peak linked by each ring is:

$$\Phi_r = \frac{D\hat{B}L_{stk}}{\nu} \cos\left(\frac{\pi}{2} - \frac{\tau_r \nu}{D}\right) \tag{10.9}$$

The voltage peak induced in a ring is $\hat{E} = \omega\hat{\Phi}_r$, where $\omega = 2\pi f$. The voltage induced in the other $(2p-1)$ rotor rings exhibits the same amplitude but a phase shift equal to $(\pi\ (n-1)\nu/p)$, where n refers to the $n-th$ rotor ring. Therefore, referring to the $k-th$ rotor ring and assuming a voltage phase equal to zero, the voltage, in complex vector form, is

$$\bar{E}_k = R_r \bar{I}_{rk} + j\omega \left[L_r \bar{I}_{rk} + M_r \sum_{n \neq k}^{2p} \bar{I}_{rn} \right] \tag{10.10}$$

Since M_r is given by (10.8) and $\bar{I}_{rn} = I_{rk} e^{j\frac{\pi\nu\cdot(n-k)}{p}}$, then

$$\bar{E}_k = R_r \bar{I}_{rk} + j\omega L_r \bar{I}_{rk} \left[1 - \frac{-1}{2p-1} \sum_{n \neq k}^{2p} e^{j\frac{\pi\nu\cdot(n-k)}{p}} \right] \tag{10.11}$$

Table 10.7: Rotor losses due to MMF harmonics in the three motors: FE VS analytical

Winding	FE [W]	Analytical [W]
48/40 DL	6800	6000
48/40 SL	34300	30300
12/10 DL	26	28
27/6 DL	1.2	0.7

The term within the square brackets results in $\frac{2p}{2p-1}$. Therefore, the amplitude of the ring current is $\hat{I}_{rk} = \hat{E}_1/|\dot{Z}_r|$, where $\dot{Z}_r = R_r + j\omega L_r \frac{2p}{2p-1}$ is the ring impedance. From (10.8), the mutual inductance between the rings on $\dot{Z}_r$ becomes more relevant when p is low. On the contrary, if $2p$ is high, $\dot{Z}_r \simeq R_r + j\omega L_r$. The losses in a single ring are computed as $P_r = R_r \hat{I}_{rk}^2/2$ and the total losses of all the rings as $P_{tot} = 2pP_r$.

Especially at high frequencies, the ring current distribution is also affected also by the proximity effect. The ring has been modeled as punctual, but the actual ring geometry affects the current distribution at high frequencies and when high harmonic orders are considered. However, the simplified analytical method presented here aims to evaluate the overall ring losses rather than their precise prediction. With no claim of exhaustiveness, it is useful for the design purpose, without the need for time-consuming FE analysis. It helps to determine if the ring solution can be conveniently adopted for the sensorless control purpose. The analytical model has been used to evaluate the ring losses due to MMF harmonics for the three case studies. Results are reported in Table 10.7 and compared with the FE simulations. Table 10.7 shows that there is a satisfactory agreement between FE and analytical computation. In the case of **machine A** and **machine B**, the model predicts the losses with an error lower than 12% compared to the simulation results. As shown, these machines are characterized by a fractional slot winding and the highest losses are found for the first sub-harmonic and harmonics close to the main one. In Fig. 10.16, the ring losses of **machine A** computed with the analytical model are compared with those from FE. Good agreement is found for the 4^{th} and the 28^{th} harmonics. The accuracy of the model decreases with higher harmonic orders. However, higher harmonic orders cause a lower amount of losses. The highest difference is found with **machine C**. This is due to the fact that there are no sub-harmonics or harmonic close to the main one in distributed windings. In **machine C**, the highest losses are at high harmonic order, which are characterized by a high frequency. However, the MMF losses are generally low in machines with distributed winding.

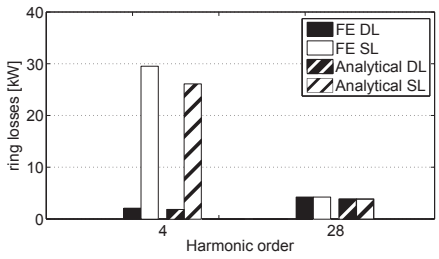

Figure 10.16: Contribution of the 4^{th} and the 28^{th} harmonics on MMF losses of **machine A**: FE vs analytical

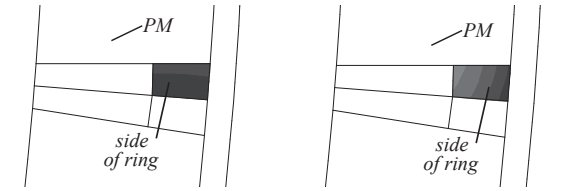

(a) Harmonic order: 4, frequency: 40 Hz

(b) Harmonic order: 28, frequency: 80 Hz

Figure 10.17: Current distribution on rings for different harmonics, **machine A**

10.8. Analytical model: cage

When a whole cage is adopted, a similar analysis is carried out. The cage can be modeled as the squirrel cage of an induction motor, by means of a complex vector model [35]. Let R_b be the bar resistance. $R_r = 2(R_b + R_e)$ is the resistance of two bars and two rotor end windings, that is, a rotor loop. Neglecting the leakage inductances of the bars and end rings, the flux linkage equation in matrix form is again given by (10.6), where in this case i_{rk} represents the k_{th} loop current.

In complex vector form, the voltage induced in the k_{th} rotor circuit by the stator MMFs is

$$\begin{aligned}\bar{E}_k &= R_r\bar{I}_{rk} - R_b\bar{I}_{r(k+1)} - R_b\bar{I}_{r(k-1)} + j\omega\left[L_r\bar{I}_{rk} + M_r\sum_{n\neq k}^{2p}\bar{I}_{rn}\right] \\ &= \bar{I}_{rk}\left(R_r - R_b e^{j\frac{\pi\nu\cdot 1}{p}} - R_b e^{j\frac{\pi\nu\cdot(2p-1)}{p}}\right) + \\ &+ j\omega L_r\bar{I}_{rk}\left[1 - \frac{-1}{2p-1}\sum_{n\neq k}^{2p} e^{j\frac{\pi\nu\cdot(n-k)}{p}}\right]\end{aligned} \tag{10.12}$$

As before, the term into square brackets can be reduced to $\frac{2p}{2p-1}$. In the other rotor loops is induced a voltage of the same amplitude but phase shift (π $(n-1)\nu/p$). The loop current $\bar{I}_{rk}$ is computed as $\bar{I}_{rk} = \bar{E}_k/\dot{Z}_{cage}$, where

$$\dot{Z}_{cage} = \left(R_r - R_b e^{j\frac{\pi\nu\cdot 1}{p}} - R_b e^{j\frac{\pi\nu\cdot(2p-1)}{p}}\right) + j\omega\cdot L_r\frac{2p}{2p-1} \tag{10.13}$$

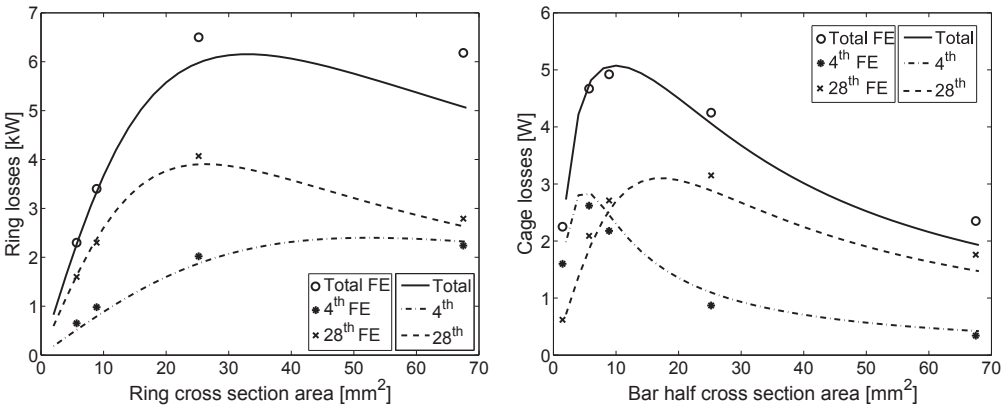

(a) ring (b) cage

Figure 10.18: Ring and cage losses due to MMF harmonics of **machine A** as a function of the cross section area: FE vs analytical

is the loop impedance. Clearly, the current flowing in the first rotor bar is $\bar{I}_{bar-k} = \bar{I}_{rk} - \bar{I}_{r(k+1)}$. The losses in a single bar and two end winding are computed as $P_r = R_b \hat{I}^2_{bar-k}/2 + 2R_e \hat{I}^2_{rk}/2$ and the total losses as $P_{tot} = 2pP_r$.

10.9. Considerations on the ring losses

In the previous Sections, the amount of ring losses has been evaluated and compared with the PM losses in different machines. It is clear that in large size machines, the ring losses can be very high, preventing the ringed–pole solution to be used. In this Section, the impact of the ring or cage cross section area on the ring losses has been evaluated. The analytical models described in Sections 10.7 and 10.7 are well suited for this kind of analysis. FE simulations have also been carried out to confirm the result.

The ring cross section area S_r of **machine A** is varied to fill from 5% to 100% of the empty space between the PMs. Then, ring and cage losses are computed both analytically and using FE. The results are reported in Fig. 10.18(a) and Fig. 10.18(b).

It should be noted that the losses initially increase with S_r. After a certain value of S_r, the losses decrease. This is expected since for small cross section area, $Z_r \simeq R_r >> X_{Lr}$ and the losses increase as $P_r \propto \hat{E}^2_r/R_r$, that is, proportionally to with S_r. On the other hand, for high cross section area, $Z_r \simeq X_{Lr} >> R_r$ and the losses $P_r \propto R_r \hat{I}^2_r$ decrease inversely proportional to S_r. With the rotor cage, the loss peak is for lower S_r.

The analytical curves and FE data in Fig. 10.18 are very close. A slight discrepancy is noticed for the higher ring cross section area, when the non-uniform current distribution is enhanced. FE analysis reveals that high current density is in the external part of the bar and rings. When frequency increases, the field governing equations in each subdomain, i.e., magnet, air-gap, stator and conductors must be solved applying the boundary conditions to the interfaces between these subdomains [172, 173]. As an

example, based on this approach, in [174] an analytical calculation is proposed to investigate the eddy-current distribution in the rotor bars of an induction motor. Anyway, the MMF harmonics of high order cause a quite low amount of rotor losses [152, 153].

Rings and cage are almost equivalent for the sensorless rotor position detection. The response of a ringed–pole machine to a high frequency injection signal was computed in [131]. In the same paper, some considerations on how the ring geometry affects the machine saliency was also given. In particular, it is convenient that the ring is located in the external part of the rotor because of the higher coupling between the ring and the stator winding.

As far as the losses are concerned, the ring and cage cross section area have to be chosen so as to avoid the losses peak, compatibly with the self-sensing capability of the machine. In the machine under analysis, for high S_r the cage exhibits lower losses while for low S_r it is convenient to use separate rings. However, this result can not be generalized, since each winding type exhibits a different harmonic content and each MMF harmonic causes a loss peak at a different cross section. The proposed analytical model can be used to rapidly determine which solution between ring and cage is more convenient from the losses point of view.

To reduce the non–uniform current distribution, strips or strand rings could be used rather than bulk copper. Alternatively, a designer could also consider the solution of ring with more than one turn. In this case, the losses may be reduced significantly. The proposed analytical model is but effective for this kind of analysis.

10.10. Conclusions

This Chapter studies the ring losses due to the MMF harmonic content, the high frequency signal injection, and the effect of the slot openings. It is shown that such losses are not relevant in small size machines with distributed winding. On the other hand, in large size machines and in machines with fractional slot winding, losses in the rings can be very high. In these cases, the adoption of the ringed–pole solution may not be a convenient solution.

It is confirmed that the ring losses are influenced by the winding type (single or double layer), the MMF harmonic content, the width of the slot opening, the airgap height and the rotation speed. However, the major contribution is given by the MMF harmonics and by the effect of the slot openings.

An analytical model is proposed to help the designer estimate the ring losses, allowing a rapid evaluation of the ringed–pole feasibility. The analysis is applied to both separated rings and whole cage. FE analysis is used to validate the results. The accuracy of the analytical model is suitable for the purpose of a preliminary design without the use of time-consuming FE simulations. This method compares rapidly the losses due to rotor rings and rotor cage, allowing to determine which solution is more convenient from the losses point of view. The analysis shows that the losses are highly dependent on the ring or cage cross section. Ring and cage exhibit a loss peak at different cross section, depending on the harmonic content. A proper choice of the ring cross section area allows the losses to be reduced.

Conclusion and future work

This Thesis is dedicated to investigate different aspects related to the design of high efficiency electrical machines with particular reference to machines with a rotor winding. The main goal of the thesis is to promote the Line Start Synchronous (LS SyM) technology as a viable solution to meet the new efficiency requirements.

New techniques of analysis for the LS SyM have been developed. One one hand the proposed procedures exhibit the advantage of short simulation time with respect time-stepping Finite Element (FE) analysis. On the other hand, the accuracy of the proposed models is high with respect that of traditional analytical models.

A new three-phase, 2-pole, $1.5kW$ LS SyM rotor lamination has been designed, prototyped and tested. This frame size is chosen because it exhibits the highest potential in efficiency improvements and it is still not available in the market. Since the LS SyM must be competitive with the workhorse of electrical motors, the IM, a robust design, suitable for the industrial production, is adopted. Both steady state and dynamic performance are considered in the design procedure. From the experimental tests, an overview comparison between the Induction Motor (IM) and LS SyM performance is given. It results that the prototype exhibits superior performance with respect that of IM. A very good synchronization capability is also achieved. This results is achieved with a small PM volume buried in the rotor.

Other aspects discussed in the Thesis deal with the design of a LS SyM lamination suitable for different number of poles to reduce the manufacturing cost and the development of an analytical model to describe the effect of MMF harmonics in LS SyM.

The second part of this Thesis is dedicated to design aspects related to electrical motors suitable for Variable Speed Drives (VSDs), with particular reference to issues related to the high-frequency (HF) signal injection sensorless technique. The aim is to design the machine so as to extend the applicability of the HF signal injection sensorless technique.
The performance achievable by IM with asymmetric cage is experimentally quantified. It is confirmed that the cage asymmetry allows the rotor position to be detected with a small reduction of the motor efficiency.
The properties of the cross-saturation inductance are deeply discussed. It is originally shown that the cross-saturation inductance depends from certain machine parameters.

With such an analysis, a designer can consider the effect of the cross-saturation inductance and mitigate its negative effect on the control strategy.
Ringed pole SyMs are studied from the ring losses point of view to investigate if the ringed-pole solution can be adopted also in large size-machines. FE analysis and analytical models are used to predict the losses. It is shown that in large size machines and in machines with fractional slot winding, losses in the rings can be very high. In these cases, the adoption of the ringed–pole solution may not be a convenient solution.

The work of this Thesis can be further extended. In particular, the analytical model proposed in Chapter 7 will be used to analyze the parasitic torques in the torque characteristic of LS SyM and IM.

Bibliography

[1] J. C. et al, "Consensus on consensus: a synthesis of consensus estimates on human-caused global warming," *Environmental Research Letters*, vol. 11, no. 4, 2016.

[2] *US president Barack Obama State of the Union speech, January 20, 2015.*

[3] *Laudato si' [Internet]. Available at: http://w2.vatican.va/content/francesco/en/encyclicals/documents/papa-francesco_20150524_enciclica-laudato-si.html.*

[4] *Islamic Declaration on Global Climate Change [Internet]. Available at: http://islamicclimatedeclaration.org/islamic-declaration-on-global-climate-change/.*

[5] P. F. et al, "Climate carbon cycle feedback analysis: Results from the c4mip model intercomparison," *Journal of Climate*, vol. 19, no. 14, pp. 3337–3353, 2006.

[6] M. G. Flanner, K. M. Shell, M. Barlage, D. K. Perovich, and M. A. Tschudi, "Radiative forcing and albedo feedback from the northern hemisphere cryosphere between 1979 and 2008," *Nature Geoscience*, vol. 4, pp. 151–155, 2011.

[7] B. D. Stocker, R. Roth, F. Joos, R. Spahni, M. Steinacher, S. Zaehle, L. Bouwman, Xu-Ri, and I. C. Prentice, "Multiple greenhouse-gas feedbacks from the land biosphere under future climate change scenarios," *Nature Climate Change*, vol. 3, pp. 666–672, 2013.

[8] S. A. N. Ion Boldea, *The Induction Machines Design Handbook, 2nd Ed.* CRC Press. ISBN 978-1-4200-6668-5, 2010.

[9] P. Vas, *Sensorless Vector and Direct Torque Control.* Oxford University Press. ISBN: 9780198564652, 1998.

[10] N. Bianchi, S. Bolognani, and P. Frare, "Design criteria for high-efficiency spm synchronous motors," *IEEE Transactions on Energy Conversion*, vol. 21, no. 2, pp. 396–404, June 2006.

[11] E. Fornasiero, L. Alberti, N. Bianchi, and S. Bolognani, "Considerations on selecting fractional-slot nonoverlapped coil windings," *IEEE Transactions on Industry Applications*, vol. 49, no. 3, pp. 1316–1324, May 2013.

[12] M. Barcaro, A. Faggion, L. Sgarbossa, N. Bianchi, and S. Bolognani, "Performance evaluation of an integrated starter alternator using an interior permanent magnet machine," *IET Electric Power Applications*, vol. 4, no. 7, pp. 539–546, August 2010.

[13] M. Ferrari, N. Bianchi, and E. Fornasiero, "Analysis of rotor saturation in synchronous reluctance and pm-assisted reluctance motors," *IEEE Transactions on Industry Applications*, vol. 51, no. 1, pp. 169–177, Jan 2015.

[14] P. Guglielmi, B. Boazzo, E. Armando, G. Pellegrino, and A. Vagati, "Permanent-magnet minimization in pm-assisted synchronous reluctance motors for wide speed range," *IEEE Transactions on Industry Applications*, vol. 49, no. 1, pp. 31–41, Jan 2013.

[15] J. K. Kostko, "Polyphase reaction synchronous motors," *Journal of the American Institute of Electrical Engineers*, vol. 42, no. 11, pp. 1162–1168, Nov 1923.

[16] R. R. Moghaddam, F. Magnussen, and C. Sadarangani, "Theoretical and experimental reevaluation of synchronous reluctance machine," *IEEE Transactions on Industrial Electronics*, vol. 57, no. 1, pp. 6–13, Jan 2010.

[17] A. de Almeida, F. Ferreira, and A. Quintino Duarte, "Technical and economical considerations on super high-efficiency three-phase motors," *IEEE Transactions on Industry Applications*, vol. 50, no. 2, pp. 1274–1285, March 2014.

[18] P. Lawrenson, R. M. Mathur, and J. Stephenson, "Transient performance of reluctance machines," *Proceedings of the Institution of Electrical Engineers*, vol. 118, no. 6, pp. 777–783, June 1971.

[19] V. Honsinger, "Permanent magnet machines: Asychronous operation," *IEEE Transactions on Power Apparatus and Systems*, vol. PAS-99, no. 4, pp. 1503–1509, July 1980.

[20] "Rotating electrical machines: Part 2-1: Standard methods for determining losses and efficiency from tests (excluding machines for traction vehicles), international standard IEC 60034-2-1, 2014."

[21] "Rotating electrical machines: Part 2-3: Specific test methods for determining losses and efficiency of converter-fed ac induction motors, international standard IEC 60034-2-3, 2013."

[22] "Rotating electrical machines: Part 30-1: Efficiency classes of line operated ac motors, international standard IEC 60034-30-1, 2014."

[23] A. de Almeida, F. Ferreira, and G. Baoming, "Beyond induction motors - technology trends to move up efficiency," in *IEEE/IAS 49th Industrial Commercial Power Systems Technical Conf (ICPS), Lakeview Drive Stone Mountain, GA, USA*, 2013, pp. 1–13.

[24] N. Tesla, "A new system of alternate current motors and transformers," *Transactions of the American Institute of Electrical Engineers*, vol. V, no. 10, pp. 308–327, July 1888.

[25] C. C. W. M. Liwschitz-Garik, *Alternating-current machines, 2nd Ed.* D. Van nostrand company, Inc., 2010.

[26] V. H. B. Heller, *Harmonic field effects in induction machines.* elsevier scientific publishing company, ISBN: 978-0444998569, 1977.

[27] K. J. Binns, R. Hindmarsh, and B. P. Short, "Effect of skewing slots on flux distribution in induction machines," *Proceedings of the Institution of Electrical Engineers*, vol. 118, no. 3.4, pp. 543–549, March 1971.

[28] J. Haataja and J. Pyrhonen, "Improving three-phase induction motor efficiency in europe," *Power Engineering Journal*, vol. 12, no. 2, pp. 81–86, April 1998.

[29] L. Alberti, N. Bianchi, A. Boglietti, and A. Cavagnino, "Core axial lengthening as effective solution to improve the induction motor efficiency classes," *IEEE Transactions on Industry Applications*, vol. 50, no. 1, pp. 218–225, Jan 2014.

[30] S. Williamson and C. I. McClay, "Optimization of the geometry of closed rotor slots for cage induction motors," *IEEE Transactions on Industry Applications*, vol. 32, no. 3, pp. 560–568, May 1996.

[31] S. Lie and C. D. Pietro, "Copper die-cast rotor efficiency improvement and economic consideration," *IEEE Transactions on Energy Conversion*, vol. 10, no. 3, pp. 419–424, Sep 1995.

[32] A. Boglietti, A. Cavagnino, L. Feraris, and M. Lazzari, "Energy-efficient motors," *IEEE Industrial Electronics Magazine*, vol. 2, no. 4, pp. 32–37, December 2008.

[33] T. J. E. Miller, "Synchronization of line-start permanent-magnet ac motors," *IEEE Transactions on Power Apparatus and Systems*, vol. PAS-103, no. 7, pp. 1822–1828, 1984.

[34] E. Richter, T. J. E. Miller, T. W. Neumann, and T. L. Hudson, "The ferrite permanent magnet ac motor—a technical and economical assessment," *IEEE Transactions on Industry Applications*, vol. IA-21, no. 3, pp. 644–650, May 1985.

[35] A. R. Munoz and T. A. Lipo, "Complex vector model of the squirrel-cage induction machine including instantaneous rotor bar currents," *IEEE Transactions on Industry Applications*, vol. 35, no. 6, pp. 1332–1340, Nov 1999.

[36] C. P. Steinmetz, "The alternating current induction motor," *Transactions of the American Institute of Electrical Engineers*, vol. XIV, no. 1, pp. 183–217, Jan 1897.

[37] G. Kron, *Equivalent circuits of electric machinery, first edition.* ed. New York: John Wiley, 1951.

[38] D. G. Dorrell, T. J. E. Miller, and C. B. Rasmussen, "Inter-bar currents in induction machines," *IEEE Transactions on Industry Applications*, vol. 39, no. 3, pp. 677–684, May 2003.

[39] A. Boglietti, A. Cavagnino, and M. Lazzari, "Computational algorithms for induction-motor equivalent circuit parameter determination; part i: Resistances and leakage reactances," *IEEE Transactions on Industrial Electronics*, vol. 58, no. 9, pp. 3723–3733, Sept 2011.

[40] ——, "Computational algorithms for induction motor equivalent circuit parameter determination; part ii: Skin effect and magnetizing characteristics," *IEEE Transactions on Industrial Electronics*, vol. 58, no. 9, pp. 3734–3740, Sept 2011.

[41] L. Alberti, N. Bianchi, and S. Bolognani, "A very rapid prediction of im performance combining analytical and finite-element analysis," *IEEE Transactions on Industry Applications*, vol. 44, no. 5, pp. 1505–1512, Sept 2008.

[42] K. Delaere, R. Belmans, and K. Hameyer, "Influence of rotor slot wedges on stator currents and stator vibration spectrum of induction machines: a transient finite-element analysis," *IEEE Transactions on Magnetics*, vol. 39, no. 3, pp. 1492–1494, May 2003.

[43] L. Alberti, N. Bianchi, and S. Bolognani, "Variable-speed induction machine performance computed using finite-element," *IEEE Transactions on Industry Applications*, vol. 47, no. 2, pp. 789–797, March 2011.

[44] A. Knight and C. McClay, "The design of high-efficiency line-start motors," *IEEE Transactions on Industry Applications*, vol. 36, no. 6, pp. 1555–1562, Nov 2000.

[45] A. Aliabad, M. Mirsalim, and N. Ershad, "Line-start permanent-magnet motors: Significant improvements in starting torque, synchronization, and steady-state performance," *IEEE Transactions on Magnetics*, vol. 46, no. 12, pp. 4066–4072, Dec 2010.

[46] A. Isfahani and S. Vaez-Zadeh, "Effects of magnetizing inductance on start-up and synchronization of line-start permanent-magnet synchronous motors," *IEEE Transactions on Magnetics*, vol. 47, no. 4, pp. 823–829, April 2011.

[47] A. Takahashi, S. Kikuchi, H. Mikami, K. Ide, and A. Binder, "Reluctance torque utility for line-starting permanent magnet motors," *IEEE Transactions on Energy Conversion*, vol. 28, no. 4, pp. 805–814, 2013.

[48] M. Popescu, T. J. E. Miller, M. McGilp, G. Strappazzon, N. Trivillin, and R. Santarossa, "Line-start permanent-magnet motor: single-phase starting performance analysis," *IEEE Transactions on Industry Applications*, vol. 39, no. 4, pp. 1021–1030, 2003.

[49] T. Miller, M. Popescu, C. Cossar, M. McGilp, G. Strappazzon, N. Trivillin, and R. Santarossa, "Line-start permanent-magnet motor single-phase steady-state performance analysis," *IEEE Transactions on Industry Applications*, vol. 40, no. 2, pp. 516–525, March 2004.

[50] M. Popescu, T. J. E. Miller, M. McGilp, G. Strappazzon, R. Santarossa, and N. Trivillin, "Asynchronous performance analysis of a single-phase capacitor-start, capacitor-run permanent magnet motor," *IEEE Transactions on Energy Conversion*, vol. 20, no. 1, pp. 142–150, March 2005.

[51] B. taek Kim and B.-I. Kwon, "Influence of space harmonics on starting performance of a single-phase line start permanent-magnet motor," *IEEE Transactions on Magnetics*, vol. 44, no. 12, pp. 4668–4672, 2008.

[52] K. Kurihara, T. Kubota, and M. Hori, "Steady-state and transient performance analysis for a single-phase capacitor-run permanent-magnet motor with skewed rotor slots," *IEEE Transactions on Industrial Electronics*, vol. 57, no. 1, pp. 44–51, Jan 2010.

[53] M. A. Rahman, A. M. Osheiba, K. Kurihara, M. A. Jabbar, H. W. Ping, K. Wang, and H. M. Zubayer, "Advances on single-phase line-start high efficiency interior permanent magnet motors," *IEEE Transactions on Industrial Electronics*, vol. 59, no. 3, pp. 1333–1345, March 2012.

[54] S. F. Rabbi and M. A. Rahman, "Critical criteria for successful synchronization of line-start ipm motors," *IEEE Journal of Emerging and Selected Topics in Power Electronics*, vol. 2, no. 2, pp. 348–358, June 2014.

[55] R. T. Ugale and B. N. Chaudhari, "Rotor configurations for improved starting and synchronous performance of line start permanent magnet synchronous motor," *IEEE Transactions on Industrial Electronics*, vol. PP, no. 99, pp. 1–1, 2016.

[56] M. Popescu, T. J. E. Miller, M. McGilp, D. M. Ionel, and S. J. Dellinger, "A unified approach to the synchronous performance analysis of single and polyphase line-fed interior permanent magnet motors," in *Conference Record of the 42nd IEEE Industry Applications Annual Meeting*, Sept 2007, pp. 148–153.

[57] M. Popescu, T. J. E. Miller, M. McGilp, F. J. H. Kalluf, C. da Silva, and L. Von Dokonal, "Effect of winding harmonics on the asynchronous torque of a single-phase line-start permanent-magnet motor," in *Conference Record of the Fourtieth IEEE Industry Applications Annual Meeting*, vol. 4, Oct 2005, pp. 2820–2827.

[58] H.-P. Nee, L. Lefevre, P. Thelin, and J. Soulard, "Determination of d and q reactances of permanent-magnet synchronous motors without measurements of the rotor position," *IEEE Transactions on Industry Applications*, vol. 36, no. 5, pp. 1330–1335, Sep 2000.

[59] T. Marcic, G. Stumberger, B. Stumberger, M. Hadziselimovic, and P. Virtic, "Determining parameters of a line-start interior permanent magnet synchronous motor model by the differential evolution," *IEEE Transactions on Magnetics*, vol. 44, no. 11, pp. 4385–4388, Nov 2008.

[60] S. Boroujeni, N. Bianchi, and L. Alberti, "Fast estimation of line-start reluctance machine parameters by finite element analysis," *IEEE Transactions on Energy Conversion*, vol. 26, no. 1, pp. 1–8, 2011.

[61] G.-H. Kang, J. Hur, H. Nam, J.-P. Hong, and G.-T. Kim, "Analysis of irreversible magnet demagnetization in line-start motors based on the finite-element method," *IEEE Transactions on Magnetics*, vol. 39, no. 3, pp. 1488–1491, May 2003.

[62] C. K. Lee, B. I. Kwon, B. T. Kim, K. I. Woo, and M. G. Han, "Analysis of magnetization of magnet in the rotor of line start permanent magnet motor," *IEEE Transactions on Magnetics*, vol. 39, no. 3, pp. 1499–1502, May 2003.

[63] K. Kurihara and M. A. Rahman, "High-efficiency line-start interior permanent-magnet synchronous motors," *IEEE Transactions on Industry Applications*, vol. 40, no. 3, pp. 789–796, May 2004.

[64] C. K. Lee and B. I. Kwon, "Design of post-assembly magnetization system of line start permanent-magnet motors using fem," *IEEE Transactions on Magnetics*, vol. 41, no. 5, pp. 1928–1931, May 2005.

[65] T. Hosoi, H. Watanabe, K. Shima, T. Fukami, R. Hanaoka, and S. Takata, "Demagnetization analysis of additional permanent magnets in salient-pole synchronous machines with damper bars under sudden short circuits," *IEEE Transactions on Industrial Electronics*, vol. 59, no. 6, pp. 2448–2456, June 2012.

[66] P. J. Lawrenson and R. M. Mathur, "Pull-in criterion for reluctance motors," *Proceedings of the Institution of Electrical Engineers*, vol. 120, no. 9, pp. 982–986, September 1973.

[67] A. Takahashi, S. Kikuchi, K. Miyata, and A. Binder, "Asynchronous torque of line-starting permanent-magnet synchronous motors," *IEEE Transactions on Energy Conversion*, vol. 30, no. 2, pp. 498–506, June 2015.

[68] G. F. T. Widger and B. Adkins, "Starting performance of synchronous motors with solid salient poles," *Electrical Engineers, Proceedings of the Institution of*, vol. 115, no. 10, pp. 1471–1484, October 1968.

[69] P. K. Kovacs, *Transient phenomena in electrical machines*. Elsevier Science Ltd, ISBN: 978-0444996633, 1984.

[70] H. L. Garbarino and E. T. B. Gross, "The Goerges phenomenon-induction motors with unbalanced rotor impedances," *Transactions of the American Institute of Electrical Engineers*, vol. 69, no. 2, pp. 1569–1575, Jan 1950.

[71] J. M. Stephenson and P. J. Lawrenson, "Average asynchronous torque of synchronous machines, with particular reference to reluctance machines," *Electrical Engineers, Proceedings of the Institution of*, vol. 116, no. 6, pp. 1049–1051, June 1969.

[72] M. Gamba, G. Pellegrino, A. Vagati, and F. Villata, "Design of a line-start synchronous reluctance motor," in *IEEE International Electric Machines Drives Conference (IEMDC), 12-15 may*, 2013, pp. 648–655.

[73] L. Alberti, N. Bianchi, and S. Bolognani, "A very rapid prediction of IM performance combining analytical and finite-element analysis," *IEEE Transactions on Industry Applications*, vol. 44, no. 5, pp. 1505–1512, Sept 2008.

[74] G. Yang, J. Ma, J.-X. Shen, and Y. Wang, "Optimal design and experimental verification of a line-start permanent magnet synchronous motor," in *International Conference on Electrical Machines and Systems, ICEMS*, Oct 2008, pp. 3232–3236.

[75] M. Morandin, S. Bolognani, and A. Faggion, "Active torque damping for an ice-based domestic chp system with an spm machine drive," *IEEE Transactions on Industry Applications*, vol. 51, no. 4, pp. 3137–3146, July 2015.

[76] L. Alberti, N. Bianchi, and S. Bolognani, "Lamination design of a set of induction motors for elevator systems," in *IEEE International Electric Machines Drives Conference, Antalya, Turkey, May*, vol. 1, May 2007, pp. 514–518.

[77] F. Ferreira, G. Baoming, and A. de Almeida, "Stator winding connection-mode management in line-start permanent magnet motors to improve their efficiency and power factor," *IEEE Transactions on Energy Conversion*, vol. 28, no. 3, pp. 523–534, Sept 2013.

[78] C. Debruyne, M. Polikarpova, S. Derammelaere, P. Sergeant, J. Pyrhonen, J. Desmet, and L. Vandevelde, "Evaluation of the efficiency of line-start permanent-magnet machines as a function of the operating temperature," *IEEE Transactions on Industrial Electronics*, vol. 61, no. 8, pp. 4443–4454, Aug 2014.

[79] M. Barcaro and N. Bianchi, "Interior pm machines using ferrite to replace rare-earth surface pm machines," *IEEE Transactions on Industry Applications*, vol. 50, no. 2, pp. 979–985, March 2014.

[80] T. Miller, M. Popescu, C. Cossar, M. McGilp, G. Strappazzon, N. Trivillin, and R. Santarossa, "Line-start permanent magnet motor-single-phase steady-state performance analysis," in *Conference Record of the 38th IEEE Industry Applications Annual Meeting.*, vol. 3, Oct 2003, pp. 1962–1969.

[81] M. J. Melfi, S. D. Umans, and J. E. Atem, "Viability of highly efficient multi-horsepower line-start permanent-magnet motors," *IEEE Transactions on Industry Applications*, vol. 51, no. 1, pp. 120–128, Jan 2015.

[82] J. Li, J. Song, and Y. Cho, "High performance line start permanent magnet synchronous motor for pumping system," in *IEEE International Symposium on Industrial Electronics (ISIE)*, July 2010, pp. 1308–1313.

[83] G. Y. Sizov, P. Zhang, D. M. Ionel, N. A. O. Demerdash, and M. Rosu, "Automated multi-objective design optimization of pm ac machines using computationally efficient fea and differential evolution," *IEEE Transactions on Industry Applications*, vol. 49, no. 5, pp. 2086–2096, Sept 2013.

[84] R. R. Moghaddam and F. Gyllensten, "Novel high-performance synrm design method: An easy approach for a complicated rotor topology," *IEEE Transactions on Industrial Electronics*, vol. 61, no. 9, pp. 5058–5065, Sept 2014.

[85] F. Cupertino, G. Pellegrino, and C. Gerada, "Design of synchronous reluctance motors with multiobjective optimization algorithms," *IEEE Transactions on Industry Applications*, vol. 50, no. 6, pp. 3617–3627, Nov 2014.

[86] G. Pellegrino, F. Cupertino, and C. Gerada, "Automatic design of synchronous reluctance motors focusing on barrier shape optimization," *IEEE Transactions on Industry Applications*, vol. 51, no. 2, pp. 1465–1474, March 2015.

[87] M. Gamba, E. Armando, G. Pellegrino, A. Vagati, B. Janjic, and J. Schaab, "Line-start synchronous reluctance motors: Design guidelines and testing via active inertia emulation," in *IEEE Energy Conversion Congress and Exposition (ECCE)*, Sept 2015, pp. 4820–4827.

[88] L. Gasparin and R. Fiser, "Intensity of the native and additional harmonic components in cogging torque due to design parameters of permanent-magnet motors," in *International Conference on Power Electronics and Drive Systems (PEDS)*, Nov 2009, pp. 1062–1067.

[89] A. Vagati, M. Pastorelli, G. Francheschini, and S. Petrache, "Design of low-torque-ripple synchronous reluctance motors," *IEEE Transactions on Industry Applications*, vol. 34, no. 4, pp. 758–765, Jul 1998.

[90] R. Ugale, B. Chaudhari, S. Baka, S. Dambhare, and A. Pramanik, "Induced pole rotor structure for line start permanent magnet synchronous motors," *Electric Power Applications (IET)*, vol. 8, no. 4, pp. 131–140, April 2014.

[91] A. Arkkio, "Synchronous torques of a cage induction motor from time-discretized finite element analysis," in *International Conference on Electrical Machines and Systems (ICEMS)*, Aug 2011, pp. 1–5.

[92] R. B. Robinson, "Harmonics in a.c. rotating machines," *Proceedings of the IEE - Part C: Monographs*, vol. 109, no. 16, pp. 380–387, September 1962.

[93] ——, "Inductance coefficients of rotating machines expressed in terms of winding space harmonic," *Electrical Engineers, Proceedings of the Institution of*, vol. 111, no. 4, pp. 769–774, April 1964.

[94] T. H. Barton and J. C. Dunfield, "Inductances of a practical slip-ring primitive i - an analytical study," *IEEE Transactions on Power Apparatus and Systems*, vol. PAS-85, no. 2, pp. 140–145, Feb 1966.

[95] B. Wymeersch, F. D. Belie, C. B. Rasmussen, F. Jensen, and L. Vandevelde, "Mutual-inductance modelling in line-start permanent-magnet synchronous machines based on winding-function theory," in *International Electric Machines Drives Conference (IEMDC)*, May 2013, pp. 607–611.

[96] P. J. Lawrenson and R. M. Mathur, "Asynchronous performance of reluctance machines allowing for irregular distributions of rotor conductors," *Electrical Engineers, Proceedings of the Institution of*, vol. 119, no. 3, pp. 318–324, March 1972.

[97] H. R. Fudeh and C. M. Ong, "Modeling and analysis of induction machines containing space harmonics, part i: Modeling and transformation," *IEEE Power Engineering Review*, vol. PER-3, no. 8, pp. 41–42, Aug 1983.

[98] J. Holtz, "Sensorless control of induction motor drives," *Proceedings of the IEEE*, vol. 90, no. 8, pp. 1359–1394, 2002.

[99] ——, "Sensorless control of induction machines; with or without signal injection?" *IEEE Transactions on Industrial Electronics*, vol. 53, no. 1, pp. 7–30, 2005.

[100] M. Degner and R. Lorenz, "Using multiple saliencies for the estimation of flux, position, and velocity in ac machines," *IEEE Transactions on Industry Applications*, vol. 34, no. 5, pp. 1097–1104, 1998.

[101] J.-I. Ha and S.-K. Sul, "Physical understanding of high frequency injection method to sensorless drives of an induction machine," in *Conference Record of the IEEE Industry Applications*, vol. 3, 2000, pp. 1802–1808.

[102] A. Consoli, G. Bottiglieri, G. Scarcella, and G. Scelba, "Flux and voltage calculations of induction motors supplied by low- and high-frequency currents," *IEEE Transactions on Industry Applications*, vol. 45, no. 2, pp. 737–746, March 2009.

[103] L. Alberti, N. Bianchi, M. Morandin, and J. Gyselinck, "Finite-element analysis of electrical machines for sensorless drives with high-frequency signal injection," *IEEE Transactions on Industry Applications*, vol. 50, no. 3, pp. 1871–1879, May 2014.

[104] Y.-D. Yoon and S.-K. Sul, "Sensorless control for induction machines based on square-wave voltage injection," *IEEE Transactions on Power Electronics*, vol. 29, no. 7, pp. 3637–3645, July 2014.

[105] J. Cilia, G. Asher, K. Bradley, and M. Sumner, "Sensorless position detection for vector-controlled induction motor drives using an asymmetric outer-section cage," *IEEE Transactions on Industry Applications*, vol. 33, no. 5, pp. 1162–1169, Sep 1997.

[106] P. Jansen and R. Lorenz, "Transducerless field orientation concepts employing saturation-induced saliencies in induction machines," *IEEE Transactions on Industry Applications*, vol. 32, no. 6, pp. 1380–1393, 1996.

[107] M. Degner and R. Lorenz, "Position estimation in induction machines utilizing rotor bar slot harmonics and carrier-frequency signal injection," *IEEE Transactions on Industry Applications*, vol. 36, no. 3, pp. 736–742, May 2000.

[108] N. Teske, G. Asher, M. Sumner, and K. Bradley, "Encoderless position estimation for symmetric cage induction machines under loaded conditions," *IEEE Transactions on Industry Applications*, vol. 37, no. 6, pp. 1793–1800, Nov 2001.

[109] S. Nandi, S. Ahmed, H. Toliyat, and R. Mohan Bharadwaj, "Selection criteria of induction machines for speed-sensorless drive applications," *IEEE Transactions on Industry Applications*, vol. 39, no. 3, pp. 704–712, May 2003.

[110] P. Jansen and R. Lorenz, "Transducerless position and velocity estimation in induction and salient ac machines," *IEEE Transactions on Industry Applications*, vol. 31, no. 2, pp. 240–247, 1995.

[111] J. Holtz, "Sensorless position control of induction motors-an emerging technology," *IEEE Transactions on Industrial Electronics*, vol. 45, no. 6, pp. 840–851, 1998.

[112] N. Teske, G. Asher, M. Sumner, and K. Bradley, "Suppression of saturation saliency effects for the sensorless position control of induction motor drives under loaded conditions," *IEEE Transactions on Industrial Electronics*, vol. 47, no. 5, pp. 1142–1150, Oct 2000.

[113] J. Holtz and H. Pan, "Elimination of saturation effects in sensorless position-controlled induction motors," *IEEE Transactions on Industry Applications*, vol. 40, no. 2, pp. 623–631, March 2004.

[114] F. Briz, M. Degner, A. Diez, and R. Lorenz, "Measuring, modeling, and decoupling of saturation-induced saliencies in carrier-signal injection-based sensorless ac drives," *IEEE Transactions on Industry Applications*, vol. 37, no. 5, pp. 1356–1364, Sep 2001.

[115] N. Teske, G. Asher, K. Bradley, and M. Summer, "Analysis and suppression of inverter clamping saliency in sensorless position controlled induction machine drives," in *Conference Record of the Thirty-Sixth IEEE IAS Annual Meeting*, vol. 4, Sept 2001, pp. 2629–2636 vol.4.

[116] M. Samonig and T. Wolbank, "Prediction of slotting saliency in induction machines with respect to high-frequency-excitation based sensorless control," in *40th Annual Conference of the IEEE Industrial Electronics Society (IECON)*, Oct 2014, pp. 794–799.

[117] M. Cirrincione, M. Pucci, G. Cirrincione, and A. Miraoui, "Space-vector state model of induction machines including rotor slotting effects: Toward a new category of observers," *IEEE Transactions on Industry Applications*, vol. 44, no. 6, pp. 1683–1692, Nov 2008.

[118] L. Alberti, N. Bianchi, and S. Boroujeni, "Finite element estimation of induction motor parameters for sensorless applications," *COMPEL: The International Journal for Computation and Mathematics in Electrical and Electronic Engineering*, vol. Vol. 31 No. 1, pp. pp. 191–205, 2012.

[119] L. Alberti, N. Bianchi, and S. Bolognani, "High frequency d-q model of synchronous machines for sensorless control," *IEEE Transactions on Industry Applications*, vol. PP, no. 99, pp. 1–1, 2015.

[120] N. Bianchi, M. Degano, and E. Fornasiero, "Sensitivity analysis of torque ripple reduction of synchronous reluctance and interior pm motors," *IEEE Transactions on Industry Applications*, vol. 51, no. 1, pp. 187–195, Jan 2015.

[121] J. Barral, R. Bonnefille, S. Henry, and J. Mesiere, "Contribution to the modelisation of satured synchronous machines," in *Conference Proceedings of the first International Conference of Electrical Machines (ICEM)*, Helsinki, Finland, October 1980.

[122] N. Bianchi, D. Durello, and A. Fasolo, "Relationship between rotor losses and size of permanent-magnet machines," *IEEE Transactions on Industry Applications*, vol. 49, no. 5, pp. 2015–2023, Sept 2013.

[123] P. Guglielmi, M. Pastorelli, and A. Vagati, "Cross-saturation effects in IPM motors and related impact on sensorless control," *IEEE Trans. on Industry Applications*, vol. 42, no. 6, pp. 1516–1522, Nov 2006.

[124] M. Morandin, A. Faggion, and S. Bolognani, "Integrated starter/alternator with sensorless ringed-pole PM synchronous motor drive," *IEEE Transactions on Industry Applications*, vol. 51, no. 2, pp. 1485–1493, March 2015.

[125] E. Capecchi, P. Guglielmi, M. Pastorelli, and A. Vagati, "Position-sensorless control of the transverse-laminated synchronous reluctance motor," *IEEE Trans. on Industry Applications*, vol. 37, no. 6, pp. 1768–1776, Nov 2001.

[126] P. Guglielmi, M. Pastorelli, G. Pellegrino, and A. Vagati, "Position-sensorless control of permanent-magnet-assisted synchronous reluctance motor," *IEEE Trans. on Industry Applications*, vol. 40, no. 2, pp. 615–622, March 2004.

[127] M. Seilmeier, S. Ebersberger, and B. Piepenbreier, "PMSM model for sensorless control considering saturation induced secondary saliencies," in *IEEE International Symposium on Sensorless Control for Electrical Drives and Predictive Control of Electrical Drives and Power Electronics (SLED/PRECEDE)*, Munich, Germany, October 2013, pp. 1–8.

[128] P. Guglielmi, M. Pastorelli, and A. Vagati, "Impact of cross-saturation in sensorless control of transverse-laminated synchronous reluctance motors," *IEEE Transactions on Industrial Electronics*, vol. 53, no. 2, pp. 429–439, April 2006.

[129] P. Garcia, F. Briz, D. Raca, and R. Lorenz, "Saliency-tracking-based sensorless control of ac machines using structured neural networks," *IEEE Trans. on Industry Applications*, vol. 43, no. 1, pp. 77–86, Jan 2007.

[130] N. Bianchi, E. Fornasiero, and S. Bolognani, "Effect of stator and rotor saturation on sensorless rotor position detection," *IEEE Trans. on Industry Applications*, vol. 49, no. 3, pp. 1333–1342, May 2013.

[131] L. Alberti, N. Bianchi, M. Morandin, and S. Bolognani, "Analysis and tests of the sensorless rotor position detection of ringed-pole permanent-magnet motor," *IEEE Transactions on Industry Applications*, vol. 50, no. 5, pp. 3278–3284, Sept 2014.

[132] D. Reigosa, P. Garcia, D. Raca, F. Briz, and R. Lorenz, "Measurement and adaptive decoupling of cross-saturation effects and secondary saliencies in sensorless controlled IPM synchronous machines," *IEEE Trans. on Industry Applications*, vol. 44, no. 6, pp. 1758–1767, Nov 2008.

[133] N. Bianchi, S. Bolognani, J.-H. Jang, and S.-K. Sul, "Comparison of PM motor structures and sensorless control techniques for zero-speed rotor position detection," *IEEE Trans. on Power Electronics*, vol. 22, no. 6, pp. 2466–2475, Nov 2007.

[134] L. Alberti, N. Bianchi, and S. Bolognani, "Comparison of different synchronous machines for sensorless drives," in *39th Annual Conference of the IEEE Industrial Electronics Society (IECON)*, Vienna, Austria, Nov. 2013, pp. 8220–8226.

[135] P. Sergeant, F. De Belie, and J. Melkebeek, "Rotor geometry design of interior PMSMs with and without flux barriers for more accurate sensorless control," *IEEE Trans. on Industrial Electronics*, vol. 59, no. 6, pp. 2457–2465, June 2012.

[136] Y. Kano, T. Kosaka, N. Matsui, and T. Nakanishi, "Design of saliency-based sensorless drive IPM motors for general industrial applications," in *IEEE Industry Applications Society (IAS) Annual Meeting*, Edmonton, Canada, October 2008, pp. 1–6.

[137] N. Bianchi and S. Bolognani, "Influence of rotor geometry of an interior pm motor on sensorless control feasibility," in *Conference Record of the Fourtieth IEEE IAS Annual Meeting*, Hong Kong, October 2005, pp. 2553–2560.

[138] V. Manzolini, M. Morandin, and S. Bolognani, "D-axis polarity detection for IPM synchronous motor drives by high frequency voltage injection," in *accepted for publication in the proceedings of The 42nd Annual Conference of IEEE Industrial Electronics Society (IECON)*, Firenze, October 2016.

[139] N. Bianchi, S. Bolognani, A. Faggion, and E. Fornasiero, "Analysis and experimental tests of the sensorless capability of a fractional-slot inset PM motor," *IEEE Trans. on Industry Applications*, vol. 51, no. 1, pp. 224–231, Jan 2015.

[140] M. Barcaro, M. Morandin, T. Pradella, N. Bianchi, and I. Furlan, "Iron saturation impact on high frequency sensorless control of synchronous permanent magnets motor," in *XXII International Conference on Electrical Machines (ICEM)*, Lausanne, Switzerland, September 2016.

[141] J. Melkebeek and J. Willems, "Reciprocity relations for the mutual inductances between orthogonal axis windings in saturated salient-pole machines," *IEEE Trans. on Industry Applications*, vol. 26, no. 1, pp. 107–114, Jan 1990.

[142] M. Morandin and S. Bolognani, "Locked rotor characterization tests of ipm/rel synchronous machine for sensorless drives," in *8th IET International Conference on Power Electronics, Machines and Drives (PEMD)*, Glasgow, Scotland, UK, April 2016, pp. 1–6.

[143] J.-H. Jang, S.-K. Sul, J.-I. Ha, K. Ide, and M. Sawamura, "Sensorless drive of SMPM motor by high frequency signal injection," in *Seventeenth Annual IEEE Applied Power Electronics Conference and Exposition (APEC)*, Dallas, Texas, October 2002, pp. 279–285.

[144] J.-I. Ha, K. Ide, T. Sawa, and S.-K. Sul, "Sensorless rotor position estimation of an interior permanent-magnet motor from initial states," *IEEE Trans. on Industry Applications*, vol. 39, no. 3, pp. 761–767, May 2003.

[145] N. Bedetti, S. Calligaro, and R. Petrella, "Accurate modeling, compensation and self-commissioning of inverter voltage distortion for high-performance motor drives," in *IEEE Applied Power Electronics Conference and Exposition (APEC)*, Texas, USA, March 2014, pp. 1550–1557.

[146] T. Nondahl, C. Ray, P. Schmidt, and M. Gasperi, "A permanent-magnet rotor containing an electrical winding to improve detection of rotor angular position," *IEEE Transactions on Industry Applications*, vol. 35, no. 4, pp. 819–824, Jul 1999.

[147] N. Bianchi, S. Bolognani, and A. Faggion, "Rotor design arrangement of SPM motors for the sensorless control at low speed and standstill," in *14th International on Power Electronics and Motion Control Conference (EPE/PEMC)*, Sept 2010, pp. S1–23–S1–28.

[148] A. Faggion, N. Bianchi, and S. Bolognani, "Ringed-pole permanent-magnet synchronous motor for position sensorless drives," *IEEE Transactions on Industry Applications*, vol. 47, no. 4, pp. 1759–1766, July 2011.

[149] M. Morandin, S. Bolognani, and A. Faggion, "Outer-rotor ringed-pole SPM starter-alternator suited for sensorless drives," in *2011 Symposium on Sensorless Control for Electrical Drives (SLED)*, 2011, pp. 96–101.

[150] M. Morandin, A. Faggion, and S. Bolognani, "Integrated starter alternator with sensorless ringed-pole pm synchronous motor drive," *IEEE Transactions on Industry Applications*, vol. 51, no. 2, pp. 1485–1493, March 2015.

[151] J. Graus and I. Hahn, "Modelling and optimization of a short-circuited rotor winding of a PMSM for saliency tracking," in *5th IEEE International Symposium on Sensorless Control for Electrical Drives (SLED)*, May 2014, pp. 1–8.

[152] N. Bianchi and E. Fornasiero, "Impact of MMF Space Harmonic on Rotor Losses in Fractional-slot Permanent-magnet Machines," *IEEE Transactions on Energy Conversion*, vol. 24, no. 2, pp. 323–328, Jun. 2009.

[153] N. Bianchi, S. Bolognani, and E. Fornasiero, "An overview of rotor losses determination in three-phase fractional-slot PM machines," *IEEE Transactions on Industry Applications*, vol. 46, no. 6, pp. 2338–2345, Nov 2010.

[154] E. Fornasiero, N. Bianchi, and S. Bolognani, "Slot harmonic impact on rotor losses in fractional-slot permanent-magnet machines," *IEEE Transactions on Industrial Electronics*, vol. 59, no. 6, pp. 2557–2564, June 2012.

[155] J. Wang, K. Atallah, R. Chin, W. Arshad, and H. Lendenmann, "Rotor eddy-current loss in permanent-magnet brushless ac machines," *IEEE Transactions on Magnetics*, vol. 46, no. 7, pp. 2701–2707, July 2010.

[156] H. V. Xuan, D. Lahaye, M. Hoeijmakers, H. Polinder, and J. Ferreira, "Studying rotor eddy current loss of PM machines using nonlinear FEM including rotor motion," in *XIX International Conference on Electrical Machines (ICEM)*, Sept 2010, pp. 1–7.

[157] L. Alberti, E. Fornasiero, N. Bianchi, and S. Bolognani, "Rotor losses measurements in an axial flux permanent magnet machine," *IEEE Transactions on Energy Conversion*, vol. 26, no. 2, pp. 639–645, June 2011.

[158] L. Alberti, E. Fornasiero, and N. Bianchi, "Impact of the rotor yoke geometry on rotor losses in permanent-magnet machines," *IEEE Transactions on Industry Applications*, vol. 48, no. 1, pp. 98–105, Jan 2012.

[159] L. Wu, Z. Zhu, D. Staton, M. Popescu, and D. Hawkins, "Analytical model for predicting magnet loss of surface-mounted permanent magnet machines accounting for slotting effect and load," *IEEE Trans. on Magnetics*, vol. 48, no. 1, pp. 107–117, Jan 2012.

[160] D. Ishak, Z. Zhu, and D. Howe, "Eddy-current loss in the rotor magnets of permanent-magnet brushless machines having a fractional number of slots per pole," *IEEE Transactions on Magnetics*, vol. 41, no. 9, pp. 2462–2469, Sept 2005.

[161] N. Bianchi, S. Bolognani, and A. Faggion, "A ringed-pole SPM motor for sensorless drives - electromagnetic analysis, prototyping and tests," in *2010 IEEE International Symposium on Industrial Electronics (ISIE)*, 2010, pp. 1193–1198.

[162] S. Sharkh, A. Qazalbash, N. T. Irenji, and R. G. Wills, "Effect of slot configuration and airgap and magnet thicknesses on rotor electromagnetic loss in surface PM synchronous machines," in *International Conference on Electrical Machines and Systems (ICEMS)*, Aug 2011, pp. 1–6.

[163] D. Wills and M. Kamper, "Analytical prediction of rotor eddy current loss due to stator slotting in PM machines," in *IEEE Energy Conversion Congress and Exposition (ECCE)*, Sept 2010, pp. 992–995.

[164] J. Pyrhonen, H. Jussila, Y. Alexandrova, P. Rafajdus, and J. Nerg, "Harmonic loss calculation in rotor surface PM - new analytic approach," *IEEE Trans. on Magnetics*, vol. 48, no. 8, pp. 2358–2366, Aug 2012.

[165] H. V. Xuan, D. Lahaye, H. Polinder, and J. Ferreira, "Influence of stator slotting on the performance of PM machines with concentrated windings," *IEEE Trans. on Magnetics*, vol. 49, no. 2, pp. 929–938, Feb 2013.

[166] F. Martin, M.-H. Zaim, A. Tounzi, and N. Bernard, "Improved analytical determination of eddy current losses in surface mounted PM of synchronous machine," *IEEE Trans. on Magnetics*, vol. 50, no. 6, pp. 1–9, June 2014.

[167] M. Andriollo, G. Bettanini, A. Morini, G. Martinelli, and A. Tortella, "Efficiency comparison of in-wheel PM motors for bus propulsion," in *XVII International Conference on Electrical Machines (ICEM)*, 2006.

[168] H. Polinder and M. Hoeijmakers, "Eddy-current losses in the segmented surface-mounted magnets of a PM machine," *IEE Proceedings on Electric Power Applications*, vol. 146, no. 3, pp. 261–266, May 1999.

[169] W.-Y. Huang, A. Bettayeb, R. Kaczmarek, and J.-C. Vannier, "Optimization of magnet segmentation for reduction of eddy-current losses in permanent magnet synchronous machine," *IEEE Transactions on Energy Conversion*, vol. 25, no. 2, pp. 381–387, June 2010.

[170] M. Mirzaei, A. Binder, B. Funieru, and M. Susic, "Analytical calculations of induced eddy currents losses in the magnets of surface mounted PM machines with consideration of circumferential and axial segmentation effects," *IEEE Transactions on Magnetics*, vol. 48, no. 12, pp. 4831–4841, Dec 2012.

[171] M. Shah and S.-B. Lee, "Optimization of shield thickness of finite length rotors for eddy current loss minimization," in *Conference Record of the 41st IEEE Industry Applications Annual Meeting*, vol. 5, Oct 2006, pp. 2368–2373.

[172] Z. Zhu, L. Wu, and Z. Xia, "An accurate subdomain model for magnetic field computation in slotted surface-mounted PM machines," *IEEE Trans. on Magnetics*, vol. 46, no. 4, pp. 1100–1115, April 2010.

[173] T. Lubin, S. Mezani, and A. Rezzoug, "2-d exact analytical model for surface-mounted permanent-magnet motors with semi-closed slots," *IEEE Transactions on Magnetics*, vol. 47, no. 2, pp. 479–492, Feb 2011.

[174] ——, "Analytic calculation of eddy currents in the slots of electrical machines: Application to cage rotor induction motors," *IEEE Trans. on Magnetics*, vol. 47, no. 11, pp. 4650–4659, Nov 2011.

List of Acronyms

EM	electric machine
LS	line-Start
SyM	synchronous machine
IM	induction machine
SRM	synchronous reluctance machine
PM	permanent magnet
HF	high frequency
SPM	surface-mounted permanent-magnet machine
VSD	variable speed drive
DC	direct-current
AC	alternating-current
PF	power factor
IEC	international electrotechnical commission
MEPS	minimum energy performance standards
EC	equivalent circuit
MMF	magneto-motive force
DE	differential evolution

Acknowledgments

Working in the Electric Drive Laboratory of Padova was an exciting and memorable experience for me. I want to thank my Supervisor Prof. Nicola Bianchi and Prof. Silverio Bolognani for their help and constructive advices. I have appreciated not only their expertise but also their kindness.

Special thanks is given to Mose' Castiello for his friendship and for his invaluable help in experimental activities. I have been very lucky to work with colleagues such as Enrico Carraro, Mattia Morandin, Emanuele Fornasiero, Davide Da Ru', Virginia Manzolini, Hanafy Mahmoud, Mahmoud Mohamed, Yawei Wang, Giacomo Bacco and Christian Babetto. It's been a pleasure working with you all.

I would also like to thank Michele Dai Pre' of Calpeda company for the prototype manufacturing and for his precious suggestions.

I am immensely grateful to my endless love Lelia, who supported me and gave birth to our beloved Nicholas and Teresa during this Ph.D period. Special thanks is given also to Lelia's family for the support. I am grateful to my Father, my sister and, last but not least, my Mother. I don't know where she is, but without her guide I would not have reached this goal of my life.

This Thesis is written in LaTeX.
An electronic version is available at: *http://paduaresearch.cab.unipd.it*